# Three-dimensional numerical modelling of gravity and electromagnetic data using unstructured tetrahedral grids

by

©Hormoz Jahandari

A thesis submitted to the School of Graduate Studies in

partial fulfilment of the requirements for the degree of

Doctor of Philosophy

**Department of Earth Sciences**

**Memorial University of Newfoundland**

April, 2015

St. John's Newfoundland & Labrador

# Abstract

This thesis investigates the forward modelling of gravity data and electromagnetic (EM) data on unstructured tetrahedral and Voronoï grids. Unstructured grids allow efficient local refinement of the mesh at the locations of high field curvature. These grids also provide the flexibility required for representing arbitrary topography and geological interfaces. For the forward modelling of gravity data, finite-element and finite-volume methods are employed, and for the modelling of electromagnetic data the finite-volume method is used. The main application of the presented gravity schemes is to minimum-structure inversion methods which use gradient-based minimization techniques. The main application of the presented electromagnetic schemes is for total-field modelling approaches. The unstructured schemes that are presented here are novel in the field of geophysics.

In the finite-volume modelling of gravity data, tetrahedral grids and their dual Voronoï grids are used for deriving cell-centred and vertex-centred schemes, respectively. In the finite-element modelling of gravity data, tetrahedral grids are used and linear and quadratic schemes are developed. The capabilities of the four schemes are illustrated with both simple and realistic synthetic examples. The results of accuracy studies show that the quadratic finite-element scheme is the most accurate but also the most computationally demanding scheme. The best trade-offs between accuracy and computational resource requirements are achieved by the linear finite-element and

the vertex-centred finite-volume schemes.

In the finite-volume modelling of electromagnetic data, staggered tetrahedral-Voronoï grids are used. The two main variants of the governing equations are discretized and solved: the direct EM-field formulation is used for modelling controlled-source and magnetotelluric data, and the EM potential formulation is used for modelling controlled-source data. To verify the controlled-source schemes, two examples are presented which show the computation of the total and secondary fields due to electric and magnetic sources in halfspaces that contain anomalous bodies. The results show good agreement with those from the literature. To demonstrate the versatility of the approach, an example is also included in which helicopter-borne data synthesized for a realistic model show good agreement with real data. The magnetotelluric scheme is verified using two benchmark COMMEMI models and the solutions are compared with those from the literature. Accuracy studies show the relatively higher accuracy of the potential scheme compared to the direct EM-field scheme. The potential scheme performs more efficiently with iterative solvers while the direct method works better with sparse direct solvers. The potential scheme is also used for studying the relative contribution of the inductive and galvanic affects to the observed electromagnetic data.

# Acknowledgements

I would like to thank my supervisor Dr. Colin Farquharson for his direction, encouragement and support throughout my project. I would also like to thank the members of my supervisory committee Dr. Charles Hurich and Dr. Alison Leitch for their guidance and support.

I am grateful to Dr. Peter Lelièvre for his assistance on different matters concerning mesh generation and programming. I am also grateful for the financial support provided by the Natural Sciences and Engineering Research Council of Canada (NSERC), the Atlantic Innovation Fund (Atlantic Canada Opportunities Agency) and Vale through the Inco Innovation Centre at Memorial University, and by the School of Graduate Studies at Memorial University.

# Table of Contents

# List of Tables

# List of Figures

# Chapter 1

# Introduction

The objective of the study presented in this thesis is to develop numerical schemes which can use unstructured grids for the forward modelling of gravity and electromagnetic (EM) data. In geophysical applications, modelling programs are usually required to work with numerical domains which contain highly complicated geological structures. Particularly, in small scale mining applications where the targets are shallow and there is a need for high precision, it is important that the geological structures and interfaces can be modelled as accurately as possible. This goal can not be efficiently achieved by the conventional structured rectilinear grids. The most efficient way of representing arbitrary structures and interfaces is to parameterize the models using unstructured grids. In addition, unstructured grids allow local refinement in the mesh which is highly advantageous for the modelling of regions with high solution curvature. The numerical methods that naturally support unstructured grids are finite- element and finite-volume methods. While the numerical methods are the only options available for modelling the geophysical EM data, gravity data can be simulated using analytical expressions. However, as it will be explained later in this section, numerical forward solvers for gravity data possess particular advantages

for gradient-based inversion algorithms. Hence, the finite-element and finite-volume methods are used in this thesis to develop numerical forward solvers for both gravity and EM data. These numerical schemes are based on unstructured tetrahedral and Voronoï grids which is a new approach in the field of geophysics.

Potential field methods (gravity and magnetics) and electromagnetic methods are two of the major categories of geophysical methods. The surveys based on these methods are conducted on the ground, in the air, in the ocean, in space, and down boreholes. These methods are employed in different disciplines and at a wide range of scales. On the larger scales, the gravity method is used in stellar and planetary studies and in geodetic studies of the earth. The magnetic method is also used in planetary studies and in studies of the earth's magnetic field. Both of these potential field methods are employed in the smaller scale oil, gas and mineral exploration and in engineering and environmental studies (see, e.g., Nabighian et al., 2005a,b). Electromagnetic methods comprise a wide range of techniques which utilize different equipment and ranges of frequencies of electromagnetic signals. Low frequencies ($\sim$ 0.001-1 Hz) are used by the magnetotelluric (MT) method which makes use of the natural occurring sources and are employed for studies of the deep crust and upper mantle (see, e.g., Vozoff, 1991) while controlled-source electromagnetic (CSEM) methods use frequencies in the range of $\sim$ 100 Hz to 1 MHz for large-scale explorations (see, e.g., Everett and Meju, 2005). There are also EM methods, like ground penetrating radar (GPR), which use high frequencies ($\sim$ 20-50 MHz) for surveys of the shallow parts of the earth (see, e.g., Francke, 2012). Like potential field methods, EM methods are also widely used in geological, engineering and environmental studies. However, similar to the magnetic method, the primary application of EM methods is in the search for minerals, particularly metallic ores (Palacky, 1987).

Detailed interpretation of potential field and EM data requires efficient and ro-

bust inversion algorithms and an integral part of any inversion algorithm is a forward solver. In the case of potential field methods, the standard forward solvers are the analytical methods which have long been available (see, e.g., Nabighian et al., 2005a,b). The numerical schemes that are presented here are aimed at being used for gradient-based inversion algorithms which make use of the sparsity of the matrices in the numerical methods in order to increase the efficiency of the inversion in terms of computation resources (for details on gradient-based inversion see, e.g., Mackie and Madden, 1993). In the case of EM methods, however, there are only numerical methods available for solving practical forward problems. The use of unstructured grids can increase the efficiency of both the forward solvers and the inversion algorithms that use these solvers.

It is true that with the passing of time more powerful computers are invented and become available. Also, with clustering of computers much more computation memory can be provided with currently available machines. Considering these facts, it might be thought that it is not necessary anymore to attempt to increase the efficiency of the numerical schemes that are used for the modelling of geophysical data. However, it should be noted that it is usually desirable to optimize an inversion by including more information to the process and by adding more refinement to the inversion grid. These require higher amounts of memory and, consequently, more efficient modelling methods.

Today, with the advances in geophysical instruments and the emergence of airborne and space-borne potential field and EM techniques, larger amounts of data are available from geophysical surveys and it is desirable to be able to incorporate as much of these data as possible into inversion procedures. This, of course, requires larger amounts of memory. Also, there are increasingly larger amounts of *a priori* information available that could be included in the inversion. This *a priori* informa-

tion is usually in the form of already discovered geological structures and parameters (from other inversions, from borehole data or other geological surveys). Accurately representing these structures with conventional structured grids requires enormous amounts of grid cells which, in turn, results in an increase in the amount of required memory and time. Therefore, there is a need for numerical schemes that can handle complex geometries with the smallest possible number of cells. Additionally, it is always more convenient to be able to conduct modelling or inversion on a single desktop computer rather than using a network of computers. One of the means to decrease the amount of the required computation resources is to use unstructured grids instead of the conventional structured grids. In these grids, the facets of the cells conform to the interfaces of the structures and, therefore, non-necessary refinements in the grid are avoided. Also, these grids allow for local refinement wherever higher accuracies are required.

Different versions of structured and unstructured grids are schematically shown by an example in Figure 1.1. This figure shows a 2-D example in which an ellipsoid is located inside a rectangular region. Panel (a) shows the original region and the object inside it. Panels (b), (c) and (d) show, respectively, a structured rectilinear, unstructured rectilinear (Quadtree), and a triangular discretization of the domain. It can be seen that the triangular grid is more efficient than the two other methods both in forming the boundary of the ellipsoid and in terms of the number of the cells that are used. The Quadtree grid contains 394 cells which is much smaller than $1,024$ cells in the structured grid but it still cannot model the boundary of the object as well as the triangular grid which consists of 282 cells. In the structured grid and the Quadtree grid, the boundary of the ellipsoid still has a staircase shape while in the triangular grid the edges of the triangles closely conform to the boundary of the ellipsoid. A similar comparison can be made between structured and unstructured grids in 3-D to

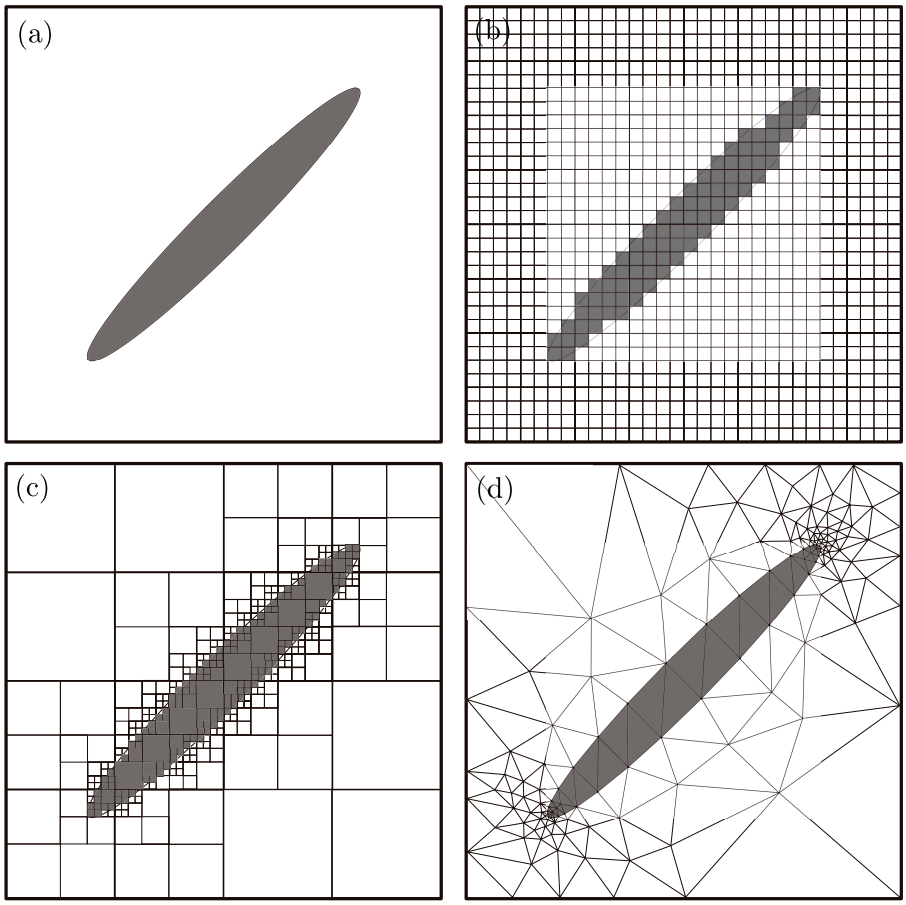


Figure 1.1: Panels (b), (c) and (d) show, respectively, a structured rectilinear, unstructured rectilinear (Quadtree), and a triangular tessellation of the region and the object inside it that is shown in panel (a).

show the advantages of unstructured tetrahedral grids over rectilinear grids.

The objective of this thesis is to develop practical programs for the forward modelling of potential field and electromagnetic data using unstructured grids. The tetrahedral tessellation is chosen, which is the most common unstructured meshing technique in 3-D. There are several open source programs available that use robust techniques for the automatic generation of tetrahedral grids (Du and Wang, 2006). For the finite-volume schemes, the dual Voronoï grids of the tetrahedral grids are also used. As gravity and magnetic methods (which comprise the potential field methods)

possess similar formulations, for the forward modelling of potential field data only the modelling of gravity data is considered in this thesis. The developed programs for gravity can, however, be easily modified to be used for the modelling of magnetic data. For the modelling of gravity data, four schemes are developed which are the cell-centred and vertex-centred finite-volume schemes and the linear and quadratic finite-element schemes. For the modelling of EM data, the finite-volume method is used and schemes are developed for the modelling of controlled-source EM data and magnetotelluric data. To the best of our knowledge, the unstructured finite-element and finite-volume schemes that are presented here are novel in the field of geophysics.

The rest of this thesis is divided into nine chapters with the first four chapters dealing with the forward modelling of gravity data and the next four chapters dealing with the modelling of EM data. Chapter 2 gives a summary of potential field theory, reviews the literature, and presents the equations that are to be solved numerically in Chapters 3 and 4 using the finite-element and finite-volume methods, respectively. The developed finite-element and finite-volume schemes are verified and assessed in Chapter 5 using both simple and realistic examples. Chapter 6 gives a brief summary of the theory of electromagnetics and reviews the literature on the numerical modelling of EM data. Chapters 7 and 8 deal, respectively, with the numerical modelling of CSEM and MT data using the direct EM-field formulation of Maxwell's equations. In these chapters, the governing equations are discretized and solved and examples are presented for the verification and evaluation of the schemes. Chapter 9 presents a CSEM scheme based on the potential formulation of Maxwell's equations and examples similar to those used in Chapter 7 are employed for verification. This chapter also presents studies for the comparison of the two CSEM schemes in terms of accuracy and resource usage. The last chapter is a summary of the entire thesis.

# Chapter 2

# Forward modelling of potential field data

## 2.1 Introduction

One of the main applications of forward methods in geophysics is their implementation in inversion procedures. One of the most important inversion families is the minimum-structure approach which has been successfully applied to the inversion of potential field data (see, e.g., Li and Oldenburg, 1996, 1998). In this approach, the objective function that is minimized is a measure of data misfit in combination with a measure of the structure of the model. This inversion, hence, avoids the over-interpretation of the data and produces geophysically interpretable models by giving the simplest acceptable solution (see, e.g., Farquharson, 2008, for more information). In a minimum-structure inversion, the earth's subsurface is discretized into cells to which the physical parameters are attributed. As the boundaries of these cells are fixed, a grid needs to be highly refined in regions of interest in order to allow the inversion to create whatever model is necessary. As a consequence, the inverse problems

that arise from the minimum-structure approach are commonly expensive in terms of computer memory. Particularly when the minimization algorithm is one of the standard Gauss-Newton methods that use analytical forward solvers, the application to real-life 3-D problems can be severely restricted.

In the context of Gauss-Newton methods, the computation of synthetic gravity data $\mathbf{d}$ due to a density model $\mathbf{m}$ can be expressed in the form

$$\mathbf{d} = \mathbf{F}\mathbf{m}, \tag{2.1}$$

where $\mathbf{d}$ and $\mathbf{m}$ are column vectors and each element, $F_{ij}$, of the matrix $\mathbf{F}$ is the gravitational acceleration at the $i$th observation point due to a unit density in the $j$th cell. When using analytical forward solvers, $\mathbf{F}$, which is also the Jacobian matrix of the Gauss-Newton algorithm, is a dense matrix that can require a considerable amount of memory storage. Also, the operations involving $\mathbf{F}$, such as the explicit formation and inversion of the approximate Hessian matrix $\mathbf{F}^T\mathbf{F}$ (which is required in the Gauss-Newton algorithm), and even simply the product of $\mathbf{F}$ with a trial vector as required in iterative solvers, can be expensive (see Section 2.4 for the forward modelling of gravity data using analytical methods).

Several methods are used to reduce the size of the Gauss-Newton equation: subspace techniques are used by Barbosa et al. (1997) and Li and Oldenburg (1998), and a data-space formulation of the Gauss-Newton equations is used by Chasseriau and Chouteau (2003) and Pilkington (2009). Alternatively, Li and Oldenburg (2003) use an iterative conjugate-gradient method to minimize the minimum-structure objective function. Instead of forming and inverting $\mathbf{F}^T\mathbf{F}$, the conjugate-gradient algorithms only require the product of $\mathbf{F}$ (and $\mathbf{F}^T$) with vectors. Mackie and Madden (1993) and Rodi and Mackie (2001) also use the conjugate-gradient method for their solu-

tions to the magnetotelluric inverse problem. However, they even avoid the explicit formation of the Jacobian matrix. In their conjugate-gradient algorithm, they evaluate the product of the Jacobian with a vector implicitly by solving a pseudo-forward problem. This pseudo-forward problem is a finite-difference solution to Maxwell's equations (like the forward problem itself). It has the same matrix as the forward problem but has a different right-hand side. Therefore, the forward problem and the inversion procedure both involve the solution of similar problems with the same matrices. As these matrices are highly sparse, these problems are solved efficiently using iterative solvers (i.e., each iteration of the conjugate-gradient optimizer involves the iterative solutions of the forward and pseudo-forward problems).

The success of the implicit approach explained above motivated the approach to the inversion of gravity data by Farquharson (2008) who uses the finite-difference method for modelling gravity data on rectilinear grids. This forward solver, which is presented separately by Farquharson and Mosher (2009), involves only sparse matrices which are suited to the conjugate-gradient matrix equation solvers. In this study, numerical forward solvers are presented for unstructured grids that are memory-efficient and suitable for use with gradient-based minimization algorithms. Both the finite-element and finite-volume techniques are considered here.

The finite-volume and finite-element schemes that are presented here discretize the computational domain into tetrahedral and Voronoï cells, and solve the discretized versions of Gauss's law and Poisson's equation to find the approximate value of the gravitational potential at all the grid points. Due to the limited number of interactions between each cell and other cells in a finite-volume or finite-element method, the resultant system of equations to be solved is highly sparse, the feature that can be exploited by the gradient-based minimization techniques to reduce inversion memory storage requirements.

Two common finite-element (FE) methods will be employed: a linear method, which is the most common FE technique, and a quadratic method which offers higher accuracy but at the same time requires more computational resources. Also, two finite-volume (FV) methods will be utilized: a cell-centred method which finds the solution at the centres of the tetrahedral cells and a vertex-centred method which finds the solution at the vertices of the tetrahedra. Using both simple and realistic synthetic models, accuracy, speed and memory requirements of these four schemes will be assessed and compared with each other.

Other numerical approaches for forward modelling of gravity data are presented by Zhang et al. (2004) and Cai and Wang (2005), who use the finite-element method to calculate the gravitational attraction of 3-D grids of rectangular prisms, and by May and Knepley (2011) who utilize the fast multipole method. Numerical methods are also used for solving geodetic boundary value problems. The finite-element and boundary-element methods are commonly used in this discipline for determining the earth's gravitational potential (see, e.g., Fašková et al., 2010, and the references therein).

In this thesis, only the forward modelling of gravity data is considered, but, as will be detailed later in this chapter, the same numerical schemes can be employed for the forward modelling of magnetic data with minor modifications. In this chapter, first tetrahedral and Voronoï grids are introduced, then potential field theory is discussed, and, finally, the equations that are used for the analytical and numerical modelling of potential field data are presented. The FE and FV schemes and their results will be given, separately, in the following chapters.

## 2.2 Tetrahedral and Voronoï grids

Tetrahedra are the simplest convex polyhedra in 3-D. Each tetrahedron has four nodes, four triangular faces and six edges. Therefore, each tetrahedron in the grid has four neighbouring tetrahedra. Voronoï grids are dual grids that can be formed for any primary grid. The Voronoï cells are formed for each node of a primary grid by connecting the circumcentres of the primary cells that share that node (circumcentres are the centres of the circumspheres of the primary cells). In this way, the Voronoï cell is the collection of the points in space that are closer to that primary node than to any other primary node in the grid. The Voronoï cells are arbitrary convex polyhedra and their faces are arbitrary convex polygons (see Figure 2.1). The Voronoï faces are always flat surfaces. A very important property of the Voronoï and tetrahedral grids is that these two grids are mutually orthogonal which means that the edges of one family of cells are perpendicular to the faces of the other family of cells. The primary node corresponding to each Voronoï cell is always located inside that Voronoï cell while the circumcentres of tetrahedra can be located inside or outside the tetrahedra. For differentiating between the elements of the primary and dual cells (elements being the vertices or nodes, edges, volumes and faces) different prefixes are used: for the tetrahedral cells "tetrahedral", "Delaunay" and "primary", and for the Voronoï cells "Voronoï", "dual" or "secondary" are used. Therefore, for example, inside each Voronoï cell there is a tetrahedral vertex (or node) and vice versa.

In this thesis, TetGen (Si, 2004) is used, which is an open-source program for generating tetrahedral and Voronoï grids. In this program, the quality of the generated tetrahedral grids can be controlled by controlling the minimum internal dihedral angle of the tetrahedra and the ratio of the smallest tetrahedral edge to the radius of the circumsphere of that tetrahedron. There is also a feature to control the maximum volume of the tetrahedra inside different regions of the grid. Moreover, the tetrahedral

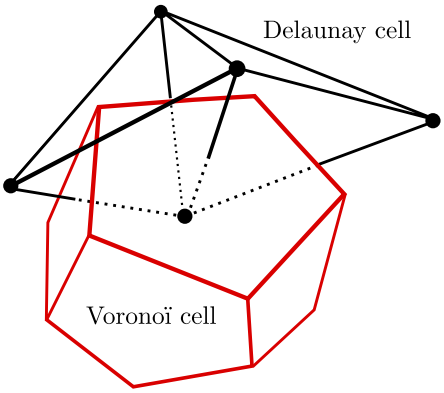


Figure 2.1: An example for the relation between tetrahedral and Voronoï cells. The vertices of the tetrahedra are the centres of the Voronoï cells and the vertices of the Voronoï cells are the circumcentres of the tetrahedra.

grids generated by TetGen are Delaunay. In a Delaunay grid, no vertex is located inside the circumspheres of the tetrahedra. This method of tetrahedralization prevents the generation of flat or skewed tetrahedra. Another interesting feature of TetGen is that the meshed domain is "conforming" meaning that all the circumcentres of the tetrahedra are located inside the domain. This is also true for all the regions that are internal to the main domain.

The input for TetGen is a file which describes the outline of the entire numerical domain and the regions that are internal to this domain. The outputs of TetGen are eight files which describe the generated tetrahedral and Voronoï grids. These files are two "node" files, two "face" files and two "cell" files for the tetrahedral and Voronoï grids, and a "neighbour" file and an "edge" file for the tetrahedral grid. Unlike structured grids, unstructured grids require these files to specify the connectivity between the nodes to form the edges, the connectivity between the edges to form the faces, and the connectivity between the faces to form the cells. Based on the definitions of the grids and the elements of the cells, it is clear that the number of tetrahedral (Voronoï) nodes equals the number of Voronoï (tetrahedral) cells, and the

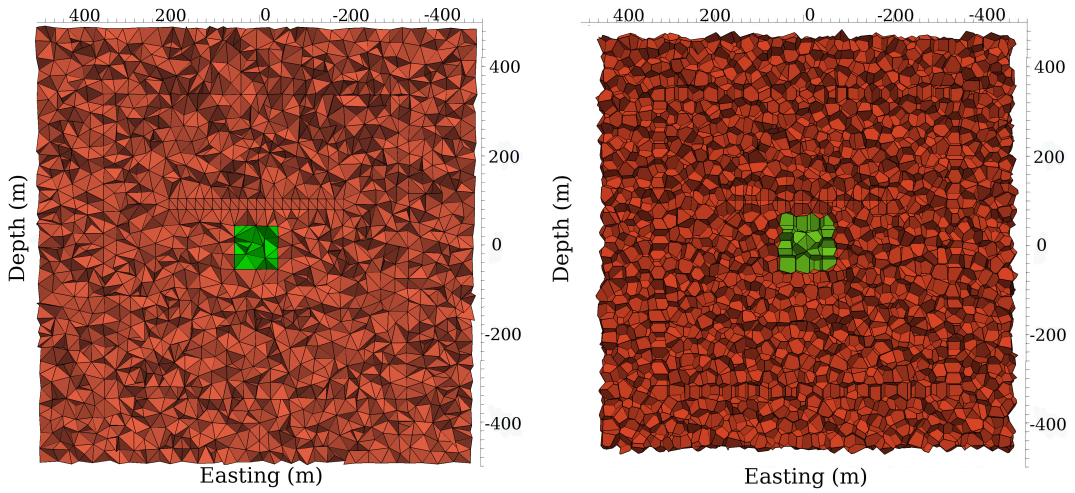


Figure 2.2: Vertical sections of an example tetrahedral grid (left panel) and its dual Voronoï grid (right panel). In the right panel, the Voronoï faces that are truncated by the domain boundary are removed for better illustration.

number of tetrahedral (Voronoï) edges equals the number of Voronoï (tetrahedral) faces. (The parentheses in the last sentence were used for avoiding the repetition of this sentence for equivalent parameters. This style will be used in the rest of this thesis.) The tetrahedra that are located on the boundary of the domain are located completely inside the domain while this boundary truncates the Voronoï cells that correspond to the primary nodes which are located on the boundary (see Figure 2.2 for examples of tetrahedral and Voronoï grids).

## 2.3 Potential field theory

### 2.3.1 Introduction

In this section, it will be shown that the potential fields (gravity and magnetism) are the solutions of second order elliptic boundary value problems. Specifically, in the presence of mass and electrical current, respectively, gravitational and magnetic

potentials satisfy Poisson's equation and in vacuum they satisfy Laplace's equation. Functions that satisfy Laplace's equation in a region are called "harmonic" in that region. These functions only have maxima or minima on the boundary of that region, a characteristic which, when combined with Green's identities, proves the uniqueness of the solution to the forward problem. In this section, which is mostly based on Blakely (1996), first the uniqueness of the forward problem for potential fields is shown and then the formulations for the forward problems are derived.

### 2.3.2 Uniqueness of the forward problem

Let $V$ and $W$ be defined as continuous functions inside region $R$, and suppose that $V$ is once continuously differentiable and $W$ is twice continuously differentiable in this region. Also, suppose that the vector field $\mathbf{F}$ is defined as

$$\mathbf{F} = V\nabla W. \tag{2.2}$$

Integrating this equation over $R$ within the closed surface $S$, using the product rule for the divergence of $V\nabla W$ and then using the divergence theorem yields Green's first identity:

$$\iiint_R V\nabla^2 W\,dv + \iiint_R \nabla W \cdot \nabla V\,dv = \oiint_S V\frac{\partial W}{\partial n}dS. \tag{2.3}$$

If $W$ is harmonic ($\nabla^2 W = 0$) and $V = 1$ then $\oiint_S V\frac{\partial W}{\partial n}dS = 0$ or

$$\oiint_S \mathbf{F}\cdot\hat{\mathbf{n}}\,dS = 0, \tag{2.4}$$

where $\hat{\mathbf{n}}$ is the unit normal vector to the surface $S$. This equation means that the normal component of $\mathbf{F}$ averages to zero over $S$. This result is Gauss's law for harmonic functions which can also be expressed as $\nabla\cdot\mathbf{F} = 0$ using the divergence theorem.

Another important result is the uniqueness of Dirichlet boundary value problems for harmonic functions: If $W_1$ and $W_2$ are two harmonic functions in $R$ and they are both zero on $S$, then the function $W_1 - W_2$ is also zero on $S$. As there should be no maxima nor minima of $W_1$ or $W_2$ inside $R$, then $W_1 - W_2$, also, needs to be zero inside $R$ or $W_1 = W_2$. A similar reasoning can be made to demonstrate the uniqueness of Neumann boundary value problems.

The second Green's identity is derived by exchanging $W$ and $V$ in the first identity and subtracting the result from the original first identity:

$$\iiint_R \left[W\nabla^2 V - V\nabla^2 W\right] dv = \oiint_S \left[W\frac{\partial V}{\partial n} - V\frac{\partial W}{\partial n}\right] dS. \tag{2.5}$$

The third Green's identity is obtained by setting $V = \frac{1}{r}$ in the relation above (in order to indicate the decay of $\mathbf{F}$ with distance), excluding the point of observation ($P$) from $R$ by a small sphere around it, and then using the solid angle at $P$ to simplify the surface integration over this sphere (Blakely, 1996):

$$W(P) = -\frac{1}{4\pi}\iiint_R \frac{\nabla^2 W}{r} dv + \frac{1}{4\pi}\oiint_S \frac{1}{r}\frac{\partial W}{\partial n} dS - \frac{1}{4\pi}\oiint_S W\frac{\partial}{\partial n}\frac{1}{r} dS, \tag{2.6}$$

which for a harmonic $W$ reduces to

$$W(P) = \frac{1}{4\pi}\oiint_S \left[\frac{1}{r}\frac{\partial W}{\partial n} - W\frac{\partial}{\partial n}\frac{1}{r}\right] dS. \tag{2.7}$$

This relation is a mixed boundary value forward problem which, as proved earlier, has a unique solution; but the converse or the inverse problem is not: the potential inside any subregion of $R$ can be attributed to an infinite number of surface distributions including the boundary of $R$ and that of the subregion. In other words, there is no unique boundary condition for a given harmonic function (Blakely, 1996).

### 2.3.3 Poisson's and Laplace's equations

It can be shown that equation 2.2 is a special case of the Helmholtz Decomposition for a continuous function $\mathbf{F}$ that vanishes at infinity. This theorem is shown as

$$\mathbf{F} = \nabla\phi + \nabla \times \mathbf{A}, \tag{2.8}$$

where $\mathbf{A}$ is a vector potential. If $\mathbf{F}$ is continuous and vanishes at infinity, we can take its integral over all space and construct

$$\mathbf{T}(P) = \frac{1}{4\pi} \iiint \frac{\mathbf{F}}{r} dv. \tag{2.9}$$

Also, if $\mathbf{T}$ tends to zero at an infinite boundary $S$, equation 2.6 for this quantity reduces to

$$\mathbf{T}(P) = -\frac{1}{4\pi} \iiint \frac{\nabla^2\mathbf{T}}{r} dv. \tag{2.10}$$

Comparing the two relations above suggests that $\mathbf{F} = -\nabla^2\mathbf{T}$ which is "Poisson's equation". Using the vector identity

$$-\nabla\left(\nabla \cdot \mathbf{T}\right) + \nabla \times \left(\nabla \times \mathbf{T}\right) = -\nabla^2\mathbf{T}, \tag{2.11}$$

and by defining $\phi = -\nabla \cdot \mathbf{T}$ and $\mathbf{A} = \nabla \times \mathbf{T}$, the Helmholtz theorem is proved. Additionally, potentials $\phi$ and $\mathbf{A}$ can be calculated from $\mathbf{F}$ by taking the divergence and curl of equation 2.9, respectively:

$$\phi = -\frac{1}{4\pi} \iiint \frac{\nabla \cdot \mathbf{F}}{r} dv \tag{2.12}$$

$$\mathbf{A} = \frac{1}{4\pi} \iiint \frac{\nabla \times \mathbf{F}}{r} dv. \tag{2.13}$$

These equations can be used to derive the magnetic scalar potential $U$ due to a distribution of magnetization $\mathbf{M}$.

Maxwell's equations in matter for the magnetic induction field $\mathbf{B}$ suggest

$$\nabla \times \mathbf{B} = \mu \nabla \times \mathbf{M} \tag{2.14}$$

$$\nabla \cdot \mathbf{B} = 0, \tag{2.15}$$

where $\mu$ is the magnetic permeability. A comparison between equation 2.14 and the following relation between $\mathbf{B}$ and the magnetizing field ($\mathbf{H}$)

$$\mathbf{B} = \mu \left( \mathbf{H} + \mathbf{M} \right) \tag{2.16}$$

shows that $\nabla \times \mathbf{H} = 0$. Therefore, according to equations 2.13 and 2.8, $\mathbf{H} = -\nabla U$. Also, if $\mu$ is the magnetic permeability of free space then taking the divergence of both sides of relation 2.16 and using $\nabla \cdot \mathbf{B} = 0$ yields

$$\nabla \cdot \mathbf{H} = -\nabla \cdot \mathbf{M}, \tag{2.17}$$

which together with equation 2.12 gives

$$U = -\frac{1}{4\pi} \iiint \frac{\nabla \cdot \mathbf{M}}{r} dv. \tag{2.18}$$

In a similar way, "Newton's law of gravitation" can be used to derive the gravitational potential $\Phi$: The gravitational force ($F'$) between two masses $m$ and $m_0$ (located, respectively, at the origin of the coordinate system and at an arbitrary position)

separated by distance $r$ is given by

$$F' = \gamma \frac{m m_0}{r^2}, \tag{2.19}$$

where $\gamma$ is the "universal gravitational constant". Division by $m_0$ gives the "gravitational acceleration" due to $m$ at the location of $m_0$:

$$\mathbf{g} = -\gamma \frac{m}{r^2} \hat{\mathbf{r}}, \tag{2.20}$$

which can be shown to have a zero curl $\nabla \times \mathbf{g} = 0$ ($\hat{\mathbf{r}}$ is a unit vector directed from $m$ to $m_0$). Consequently, the same reasoning as was made for $\mathbf{H}$ suggests

$$\mathbf{g} = \nabla \Phi, \tag{2.21}$$

and

$$\Phi = \frac{1}{4\pi} \iiint \frac{\nabla \cdot \mathbf{g}}{r} dv. \tag{2.22}$$

The results obtained so far can be used to derive Poisson's and Laplace's equations: Expressions 2.20 and 2.21 suggest that

$$\Phi = \gamma \frac{m}{r}. \tag{2.23}$$

Therefore, the potential of a distribution of mass with volume $v$ and density $\rho$ at point $Q$ is

$$\Phi(P) = \gamma \iiint_v \frac{\rho(Q)}{r} dv. \tag{2.24}$$

Comparing equations 2.22 and 2.24 gives Poisson's equation for gravity

$$\nabla^2 \Phi(P) = -4\pi\gamma\rho(P), \tag{2.25}$$

which outside matter (in vacuum) transforms to Laplace's equation:

$$\nabla^2 \Phi = 0. \tag{2.26}$$

Similarly, taking the divergence of both sides of equation 2.16 and using $\nabla \cdot \mathbf{B} = 0$ yields

$$\nabla \cdot \mu \mathbf{H} = -\nabla \cdot \mu \mathbf{M}. \tag{2.27}$$

Using $\mathbf{H} = -\nabla U$ gives Poisson's equation for magnetostatics:

$$\nabla \cdot \mu \nabla U = \nabla \cdot \mu \mathbf{M}. \tag{2.28}$$

In the absence of strongly magnetic materials (as in the earth's crust where materials are mostly weakly magnetic) this relation reduces to Laplace's equation as

$$\nabla \cdot \mu \nabla U = 0. \tag{2.29}$$

In the SI system of units, gravitational acceleration (or attraction) has the unit of $\mathrm{m/s^2}$, gravitational potential has the unit of $\mathrm{m^2/s^2}$ and magnetic field is in Tesla (N/Am). In the cgs system of units, gravitational acceleration is reported in $\mathrm{cm/s^2}$ which is also referred to as Gal. In geophysical applications, the unit which most conveniently describes gravitational anomalies is mGal and magnetic field is described by nanotesla (nT). The gravitational constant $\gamma$ has the value of $6.67 \times 10^{-8}\ \mathrm{cm^3\,g^{-1}\,s^{-2}}$ in cgs units.

## 2.4 Formulations for analytical methods

The forward modelling of gravity data in three dimensions by analytical methods has been studied by several authors during the last decades. Talwani and Ewing (1960) used horizontal polygonal plates for modelling simple geological bodies. Right rectangular prisms were introduced by Nagy (1966) and dipping prisms by Hjelt (1974) as means of modelling the sources of the gravitational field. Sources with arbitrary shapes were modelled by Barnett (1976) who proposed bodies with surfaces composed of triangular facets and by Okabe (1979) who used polygonal facets. In practice, the source region is divided into a number of cells with simple geometrical shapes and then the gravitational attraction at an observation point is calculated as the summation of the effects of all these cells.

There is a variety of methods available for obtaining closed-form expressions for polyhedral bodies (see the review by Li and Chouteau, 1998). All these methods derive expressions for the first derivative of equation 2.24 in a given direction ($k$) which can be written as

$$\Phi_k = \gamma \iiint_v \nabla (\rho\, u) \cdot \mathbf{k}\, dv, \tag{2.30}$$

where $u = -1/r$ and $\mathbf{k}$ is the direction vector of $k$ (for our application this is the downward direction). By applying the divergence theorem we have

$$\Phi_k = \gamma \oiint_s \rho\, u\, \mathbf{k} \cdot \mathbf{n}\, ds, \tag{2.31}$$

where $\mathbf{n}$ is the unit outward normal to the surface $s$ which surrounds the body. If this body is a homogeneous polyhedron with $m$ planar facets, the integral above can

be written as a summation over the polygonal facets as

$$\Phi_k = \gamma\rho \sum_{i=1}^{m} \mathbf{k} \cdot n_i \, I_i, \tag{2.32}$$

where $n_i$ is the unit outward normal to the facet $i$ and $I_i$ contains terms which are functions of the coordinates of the vertices of this facet. The difference between the analytical methods lies in the difference between the methods for deriving $I$. In this study, the analytical expressions given by Okabe (1979) are used where $I_i$ is defined as the summation of definite integrals over the edges of the facet $i$. Because tetrahedral grids are used here, in the relation above, $m = 4$. In this thesis, the analytical expressions were used for verifying the accuracy of the finite-element and finite-volume forward solvers. The relations above can also be used for deriving analytical expressions for the forward modelling of magnetic data. The equation of pseudo-gravity transformation (Blakely, 1996) can be used for showing the relation between the gravitational acceleration and the magnetic potential:

$$U = -\frac{C\,\mathbf{M}}{\gamma\rho}\,\Phi_k. \tag{2.33}$$

In this relation, $C$ is a constant (1 in the emu system of units and $10^{-7}$ in the SI). In order to use this relation for calculating the magnetic potential, $\mathbf{k}$ in relation 2.32 should be chosen as the constant magnetic intensity vector of the source body. For calculating the magnetic field a further derivative from this potential is required (Okabe, 1979).

## 2.5 Formulations for numerical methods

As was shown in Section 2.3.3, gravitational attraction, $\mathbf{g}$, is a conservative field and it can be expressed as the gradient of a potential $\Phi$ (Blakely, 1996):

$$\mathbf{g} = \nabla\Phi. \tag{2.34}$$

This relationship is valid for any point both inside and outside the mass so long as $\mathbf{g}$ is caused by a bounded distribution of piecewise-continuous density (see, e.g., Kellogg, 1967; Blakely, 1996). Also, it was shown that the relationship between density, $\rho$, and gravitational potential throughout space is described by

$$\nabla^2\Phi = -4\pi\gamma\rho, \tag{2.35}$$

where $\gamma$ is the gravitational constant. This is Poisson's equation for the gravitational potential. An alternative mathematical statement is "Gauss's law for the gravitational field" which relates the total mass, $M$, inside a region to the normal component of gravitational attraction integrated over the boundary, $s$, of the region:

$$\oiint_s \mathbf{g} \cdot \hat{\mathbf{n}}\, ds = -4\pi\gamma M, \tag{2.36}$$

where $\hat{\mathbf{n}}$ is the unit outward normal to the boundary.

In the next two chapters, Poisson's equation and Gauss's law will be approximated using FE and FV methods, respectively, and they will be solved to find the values of gravitational potential at grid points. Different methods are used in the FV and FE methods to recover the vertical component of gravitational acceleration from the potential. The potential is taken to satisfy homogeneous Dirichlet boundary

conditions and the density is discretized using a tetrahedral grid, i.e., the density is constant within each tetrahedral cell, but can be different from one cell to the next. The open-source program TetGen (Si, 2004) is used here for generating the required grids.

# Chapter 3

# Finite-element schemes for the forward modelling of gravity data

## 3.1 Introduction

The finite-element method is one of the numerical methods that is widely used for solving boundary value problems on unstructured grids. In principle, the FE method approximates the solution of the weak form of a partial differential equation by minimizing an error function. The numerical domain is discretized into finite elements, or cells, and the solution is approximated over these elements using simple polynomials of low orders which are called basis functions or interpolation functions. Although polynomials of higher orders result in more accurate approximations, they also result in numerical schemes which are more expensive to solve. The approximation in terms of basis functions transforms the continuum problem into a discrete problem which is called the weak formulation. In this formulation, the solution to be determined is a set of discrete unknown coefficients of the basis functions. For deriving this formulation, initially, an error function is constructed which quantifies the mismatch between

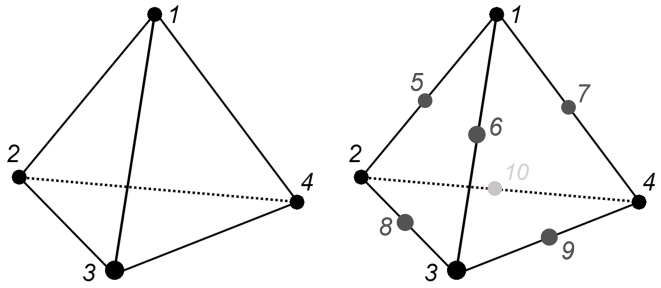


Figure 3.1: Left and right figures show the linear and quadratic tetrahedral elements, respectively, that are used in the finite-element schemes. The linear and quadratic elements possess, respectively, four and ten grid points, which are shown here as dots with their local numbering.

the true solution and the approximate solution. Afterwards, this error function is set to zero in an average sense and it is minimized in order to find the approximate solution. For this minimization, many different classes of methods are used. In this study, Galerkin's method is employed which is one of the most widely used weighted residual methods (see, e.g., Reddy, 2006).

In this chapter, the linear and quadratic finite-element schemes developed for the forward modelling of gravity data are described. The two following sections deal with the derivation and solution of these schemes for potential, and the recovery of gravity from this solution. The results for potential and gravity will be presented in Chapter 5.

## 3.2 Linear and quadratic schemes

Linear and quadratic FE schemes are developed which both use tetrahedral cells. The potential $\Phi$ is approximated over the cells using simple polynomials, i.e., basis functions, and then Galerkin's method is used to solve for the potential at the grid points. In the linear scheme, these points are the vertices of the tetrahedra while in

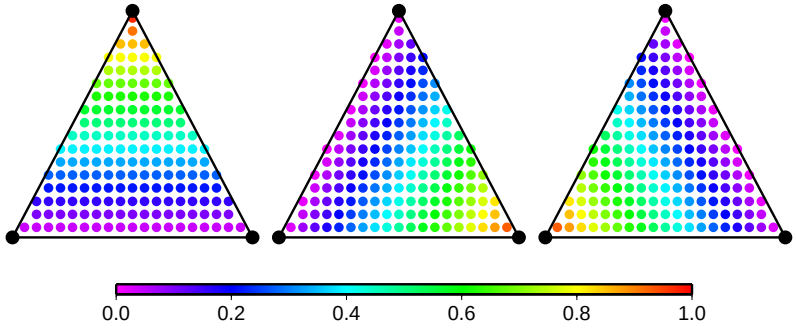


Figure 3.2: The linear basis functions for the three vertices of one of the faces of a regular tetrahedron over the relevant face. From left to right the figures show the basis functions for the top, right and left vertices, respectively. The red color shows the unit value and the purple color represents zero.

the quadratic scheme grid points are the vertices and the midpoints of the edges of the tetrahedra (see Figure 3.1). Gravitational acceleration is recovered from the primary solution (potential) as a post-processing stage.

At any point inside tetrahedron $e$, the approximate solution $\phi$ is expressed as (Jin, 2002)

$$\phi_e(x, y, z) = \sum_{j=1}^{n} N_{ej}(x, y, z)\, \phi_{ej}, \tag{3.1}$$

where $\phi_{ej}$ and $N_{ej}$ are the solutions and basis functions (linear or quadratic) attributed to the $n$ grid points of cell $e$. In the linear and quadratic FE schemes $n$ equals four and ten, respectively. The basis function of a grid point in a cell is equal to unity at that point, it vanishes towards the other points in the cell, and it is zero everywhere else in the grid:

$$N_{ei}\,(x_j, y_j, z_j) = \delta_{ij} = \begin{cases} 1 & i = j \\ 0 & i \neq j \end{cases} \tag{3.2}$$

As an example, Figures 3.2 and 3.3 show, respectively, the linear and quadratic basis functions for the grid points of one of the faces of a regular tetrahedron.

From the property stated above, it can be concluded that the interpolated so-

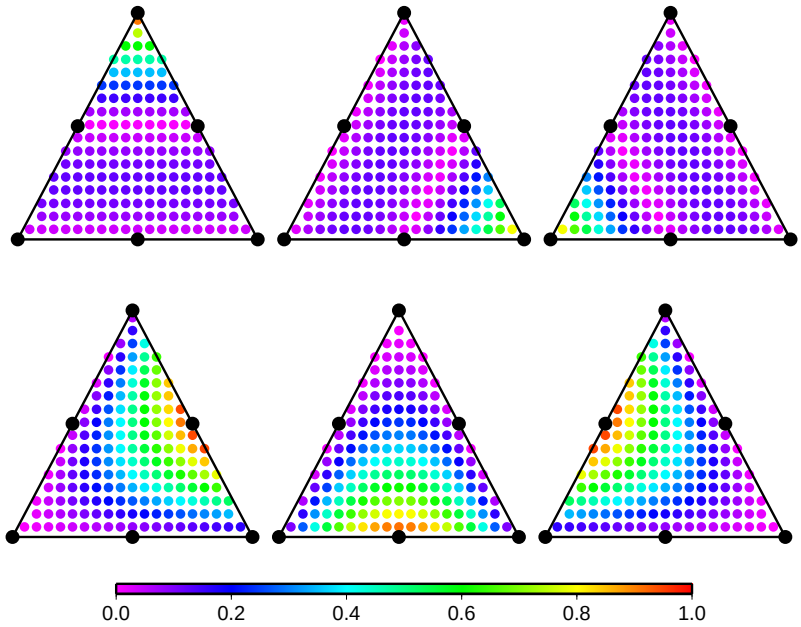


Figure 3.3: The quadratic basis functions for the grid points of one of the faces of a regular tetrahedron over this face. The grid points for this face are the three vertices and the three midpoints of the edges. From top left to top right the figures show the basis functions for the top, right and left vertices, respectively. From bottom left to bottom right the figures show the basis functions for the midpoint of the right, middle and left edges, respectively. The red color shows the unit value and the purple color represents zero.

lutions on a face which separates two elements is only the linear combination of the solutions corresponding to the grid points of that face (three and six grid points for the linear and quadratic methods, respectively). This property guarantees the continuity of $\phi$ across the inter-element faces.

In a linear tetrahedron,

$$\phi_e(x, y, z) = a_e + b_e x + c_e y + d_e z, \tag{3.3}$$

where $a_e$, $b_e$, $c_e$ and $d_e$ are constant coefficients. Therefore, for the four vertices of $e$

with coordinates $(x_i, y_i, z_i)$, $i = 1, 2, 3, 4$, we can write

$$\begin{aligned}
\phi_{e1} &= a_e + b_e x_1 + c_e y_1 + d_e z_1 \\
\phi_{e2} &= a_e + b_e x_2 + c_e y_2 + d_e z_2 \\
\phi_{e3} &= a_e + b_e x_3 + c_e y_3 + d_e z_3 \\
\phi_{e4} &= a_e + b_e x_4 + c_e y_4 + d_e z_4.
\end{aligned} \tag{3.4}$$

These four relations form a system of equations from which the constants $a_e$, $b_e$, $c_e$ and $d_e$ can be derived as

$$\begin{aligned}
a_e &= \frac{1}{6V_e}\begin{vmatrix} \phi_{e1} & \phi_{e2} & \phi_{e3} & \phi_{e4} \\ x_{e1} & x_{e2} & x_{e3} & x_{e4} \\ y_{e1} & y_{e2} & y_{e3} & y_{e4} \\ z_{e1} & z_{e2} & z_{e3} & z_{e4} \end{vmatrix} = \frac{1}{6V_e}\left(a_{e1}\phi_{e1} + a_{e2}\phi_{e2} + a_{e3}\phi_{e3} + a_{e4}\phi_{e4}\right) \\
b_e &= \frac{1}{6V_e}\begin{vmatrix} 1 & 1 & 1 & 1 \\ \phi_{e1} & \phi_{e2} & \phi_{e3} & \phi_{e4} \\ y_{e1} & y_{e2} & y_{e3} & y_{e4} \\ z_{e1} & z_{e2} & z_{e3} & z_{e4} \end{vmatrix} = \frac{1}{6V_e}\left(b_{e1}\phi_{e1} + b_{e2}\phi_{e2} + b_{e3}\phi_{e3} + b_{e4}\phi_{e4}\right) \\
c_e &= \frac{1}{6V_e}\begin{vmatrix} 1 & 1 & 1 & 1 \\ x_{e1} & x_{e2} & x_{e3} & x_{e4} \\ \phi_{e1} & \phi_{e2} & \phi_{e3} & \phi_{e4} \\ z_{e1} & z_{e2} & z_{e3} & z_{e4} \end{vmatrix} = \frac{1}{6V_e}\left(c_{e1}\phi_{e1} + c_{e2}\phi_{e2} + c_{e3}\phi_{e3} + c_{e4}\phi_{e4}\right) \\
d_e &= \frac{1}{6V_e}\begin{vmatrix} 1 & 1 & 1 & 1 \\ x_{e1} & x_{e2} & x_{e3} & x_{e4} \\ y_{e1} & y_{e2} & y_{e3} & y_{e4} \\ \phi_{e1} & \phi_{e2} & \phi_{e3} & \phi_{e4} \end{vmatrix} = \frac{1}{6V_e}\left(d_{e1}\phi_{e1} + d_{e2}\phi_{e2} + d_{e3}\phi_{e3} + d_{e4}\phi_{e4}\right),
\end{aligned} \tag{3.5}$$

where $V_e$ is the volume of the tetrahedron $e$ and the coefficients $a_{ej}$, $b_{ej}$, $c_{ej}$ and $d_{ej}$ $(j = 1, 2, 3, 4)$ are functions of the coordinates of the vertices which can be derived from the given determinants. The comparison of the relations above with equation 3.1 results in the following expression for the linear basis functions:

$$N^l_{ej}(x, y, z) = \frac{1}{6V_e}\left(a_{ej} + b_{ej}x + c_{ej}y + d_{ej}z\right) \qquad j = 1, 2, 3, 4 \tag{3.6}$$

where the superscript $l$ stands for "linear".

As already mentioned, in the quadratic method each element has ten nodes. The basis functions for these nodes are formed using the linear basis functions (Jin, 2002):

$$\begin{aligned}
N^q_{ei}(x, y, z) &= \left(2N^l_{ei} - 1\right) N^l_{ei} \qquad i = 1, 2, 3, 4 \\
N^q_{e5}(x, y, z) &= 4N^l_{e1}N^l_{e2}, \qquad N^q_{e6}(x, y, z) = 4N^l_{e1}N^l_{e3} \\
N^q_{e7}(x, y, z) &= 4N^l_{e1}N^l_{e4}, \qquad N^q_{e8}(x, y, z) = 4N^l_{e2}N^l_{e3} \\
N^q_{e9}(x, y, z) &= 4N^l_{e3}N^l_{e4}, \qquad N^q_{e10}(x, y, z) = 4N^l_{e2}N^l_{e4},
\end{aligned} \tag{3.7}$$

where the superscript $q$ stands for "quadratic" and the node numbering is shown in Figure 3.1.

One of the most widely-used finite-element methods is Galerkin's method which finds the solution of a differential equation by weighting the residual of the equation. If $\phi$ is the approximate solution of equation 2.35, then the residual $R$ for this equation is given by

$$R = \nabla^2\phi + 4\pi\gamma\rho, \tag{3.8}$$

which is generally nonzero. In Galerkin's method, the functions used for the weighting of residuals over the element $e$ are the same as the basis functions (linear or quadratic)

of that element:

$$R_{ei} = \iiint\limits_{V_e} N_{ei}\, R_e\, dv \qquad i = 1, 2, 3, \ldots, n \tag{3.9}$$

where $R_{ei}$ is the weighted residual of the $i$th node in the element. The substitution of equation 3.8 into 3.9 and setting the weighted residual to zero yields

$$\iiint\limits_{V_e} \nabla^2 \phi_e\, N_{ei}\, dv = -4\pi\gamma\rho_e \iiint\limits_{V_e} N_{ei}\, dv \qquad i = 1, 2, 3, \ldots, n. \tag{3.10}$$

Based on Green's first identity (equation 2.3) for the functions that satisfy the homogeneous Dirichlet boundary condition (i.e., the right-hand-side of equation 2.3 is zero) we can write

$$\iiint\limits_{V_e} \nabla^2 \phi_e\, N_{ei}\, dv = -\iiint\limits_{V_e} \nabla \phi_e\, \nabla N_{ei}\, dv. \tag{3.11}$$

Applying this relation to the left-hand side of equation 3.10 and incorporating equation 3.1 gives the following relation for the element $e$ (the so-called elemental equation):

$$\sum_{j=1}^{n} \phi_{ej} \iiint\limits_{V_e} \nabla N_{ei} \cdot \nabla N_{ej}\, dv = 4\pi\gamma\rho_e \iiint\limits_{V_e} N_{ei}\, dv \qquad i = 1, 2, 3, \ldots, n. \tag{3.12}$$

This relation is the discretized weak form of the Poisson's equation. It is called weak because it is an approximation of the original relation in which the continuity requirement for solving the problem is weakened. In fact, the approximated solutions at the grid points of element $e$ (i.e., $\phi_e$) are discrete coefficients of the basis functions of these grid points (i.e., $N_e$).

The elemental equation (relation 3.12) for element $e$ can be written in a matrix

form as

$$[K_e]\,\{\phi_e\} = \{b_e\}, \tag{3.13}$$

where $[K_e]$ is an $n \times n$ matrix, and $\{\phi_e\}$ and $\{b_e\}$ are $n \times 1$ column vectors. The components of $[K_e]$ and $\{b_e\}$ can be written, respectively, as

$$K_{eij} = \iiint_{V_e} \left( \frac{\partial N_{ei}}{\partial x}\frac{\partial N_{ej}}{\partial x} + \frac{\partial N_{ei}}{\partial y}\frac{\partial N_{ej}}{\partial y} + \frac{\partial N_{ei}}{\partial z}\frac{\partial N_{ej}}{\partial z} \right) dv \tag{3.14}$$

and

$$b'_{ei} = 4\pi\gamma\rho_e \iiint_{V_e} N_{ei}\, dv, \tag{3.15}$$

with $i$ and $j$ varying from one to $n$. $K_{eij}$ are sometimes referred to as "interactions" between different nodes in the cell. In the linear elements, there is only one type of interaction between the nodes of the element (i.e., the vertices) while in the quadratic method there are different types of these interactions. The integrals in the relations above can be calculated analytically using the following formula (see, e.g., Zienkiewicz and Taylor, 2000)

$$\iiint_{V_e} \left(N^l_{e1}\right)^m \left(N^l_{e2}\right)^n \left(N^l_{e3}\right)^o \left(N^l_{e4}\right)^p dv = \frac{m!\, n!\, o!\, p!}{(m+n+o+p+3)!} 6V_e, \tag{3.16}$$

which results in

$$K_{eij} = \frac{1}{36V_e}\left(b_{ei}b_{ej} + c_{ei}c_{ej} + d_{ei}d_{ej}\right) \tag{3.17}$$

and

$$b'_{ei} = \pi\gamma\rho_e V_e, \tag{3.18}$$

for the linear elements ($b$, $c$ and $d$ are the coefficients in relation 3.6). For the quadratic elements, there are seven different types of interactions between different nodes in an

element (between the vertices, between the midpoints of the edges, and between the vertices and the midpoints of the edges). Relations below give these interactions between the nodes in a quadratic element according to the numbering given in Figure 3.1

$$
\begin{aligned}
K_{e11} &= \frac{3}{180V_e}\left(b_{e1}^2 + c_{e1}^2 + d_{e1}^2\right) \\
K_{e12} &= \frac{-1}{180V_e}\left(b_{e1}b_{e2} + c_{e1}c_{e2} + d_{e1}d_{e2}\right) \\
K_{e15} &= \frac{1}{180V_e}\left(3b_{e1}b_{e2} + 3c_{e1}c_{e2} + 3d_{e1}d_{e2} - b_{e1}^2 - c_{e1}^2 - d_{e1}^2\right) \\
K_{e18} &= \frac{-1}{180V_e}\left(b_{e1}b_{e2} + b_{e1}b_{e3} + c_{e1}c_{e2} + c_{e1}c_{e3} + d_{e1}d_{e2} + d_{e1}d_{e3}\right) \\
K_{e88} &= \frac{2}{45V_e}\left(b_{e2}^2 + b_{e3}^2 + c_{e2}^2 + c_{e3}^2 + d_{e2}^2 + d_{e3}^2 + b_{e2}b_{e3} + c_{e2}c_{e3} + d_{e2}d_{e3}\right) \\
K_{e56} &= \frac{1}{45V_e}\left(b_{e1}^2 + c_{e1}^2 + d_{e1}^2 + b_{e1}b_{e2} + c_{e1}c_{e2} + d_{e1}d_{e2} + b_{e1}b_{e3} + c_{e1}c_{e3} + d_{e1}d_{e3} + \right. \\
&\quad \left. 2b_{e2}b_{e3} + 2c_{e2}c_{e3} + 2d_{e2}d_{e3}\right) \\
K_{e59} &= \frac{1}{45V_e}\left(b_{e1}b_{e3} + c_{e1}c_{e3} + d_{e1}d_{e3} + b_{e1}b_{e4} + c_{e1}c_{e4} + d_{e1}d_{e4} + \right. \\
&\quad \left. b_{e2}b_{e3} + c_{e2}c_{e3} + d_{e2}d_{e3} + + b_{e2}b_{e4} + c_{e2}c_{e4} + d_{e2}d_{e4}\right).
\end{aligned} \tag{3.19}
$$

Note that the interactions that are not given are the same interaction types as the expressions given above (e.g., $K_{e13}$ and $K_{e14}$ are the same interaction types as $K_{e12}$). There are also two types of solutions for the right-hand-side terms for the quadratic elements. These two types refer to the nodes that are located at the vertices and at the midpoints of the edges. Again, according to the numbering given in Figure 3.1:

$$
\begin{aligned}
b'_{ei} &= -\left(\pi\gamma\rho_e V_e\right)/5 \quad i = 1, 2, 3, 4 \\
b'_{ei} &= \left(4\pi\gamma\rho_e V_e\right)/5 \quad i = 5, 6, 7, 8, 9, 10
\end{aligned} \tag{3.20}
$$

In order to obtain a global system of equations, we need to sum the elemental

equations (equation 3.13) of all the elements in such a way that the number of equations equals the number of unknowns, i.e., the number of nodes in the grid. This can be done by expanding the elemental matrices and vectors in equation 3.13, with order $n$, to an order equal to the number of unknowns, $M$, and then perform a summation as

$$\sum_{e=1}^{M} \left[\bar{K_e}\right] \sum_{e=1}^{M} \{\bar{\phi_e}\} = \sum_{e=1}^{M} \{\bar{b_e}\} \tag{3.21}$$

where $\left[\bar{K_e}\right]$ is a $M \times M$ matrix, and $\{\bar{\phi_e}\}$ and $\{\bar{b_e}\}$ are $M \times 1$ column vectors. In these arrays, all the components are zero except for those corresponding to the components in the original arrays with order $n$. However, here, those components are at locations corresponding to the global numbering of the nodes in the grid (rather than the local numbering used in equation 3.13 which was based on Figure 3.1).

In practice, for finding the summations in equation 3.21, loops are used in the computer program that was written which find the sum of the interactions between two arbitrary nodes over all the elements that these nodes share together. The same summation is performed for forming the right-hand-side terms. This summation (also called "assembly") over all the elements of the grid, with total $M$ nodes, results in the matrix equation

$$[K]\,\{\phi\} = \{b\}, \tag{3.22}$$

where $[K]$ is an $M \times M$ matrix and $\{\phi\}$ and $\{b\}$ are $M \times 1$ column vectors. In the linear method, $[K]$ is a single matrix while in the quadratic method it is a block matrix which can be displayed as

$$\begin{pmatrix} K_v & K_b \\ K_b^T & K_m \end{pmatrix} \begin{pmatrix} \phi_v \\ \phi_m \end{pmatrix} = \begin{pmatrix} b_1 \\ b_2 \end{pmatrix}. \tag{3.23}$$

In this equation, $K_v$ and $K_m$ are symmetric matrices of orders $n_v$ and $n_m$, respectively,

with $n_v$ and $n_m$ being the number of vertices and the number of edges. $K_v$ contains the interactions between the nodes (i.e., the grid points) at the vertices, and $K_m$ contains the interactions between the nodes at the midpoints of the edges. $K_b$ is a $n_v \times n_m$ matrix which contains the interactions between the nodes at the vertices and those nodes at the midpoints of the edges. $\phi_v$ and $\phi_m$ are, respectively, $n_v \times 1$ and $n_m \times 1$ column vectors that contain unknown potentials at the vertices and at the edges.

Figure 3.4 shows examples of linear and quadratic coefficient matrices (matrix $[K]$ in equation 3.22) corresponding to a grid with $4,294$ tetrahedral cells, 798 vertices and $5,266$ tetrahedral edges. It can be seen that these matrices are highly sparse. In fact, the number of nonzero components inside each row of these matrices equals the "degree of freedom" of the node which corresponds to that row plus one (for the diagonal component). The degree of freedom of a node is defined as the number of nodes that share a linear/quadratic element with that node or, in other words, have interaction with that node. Also, both the linear and quadratic coefficient matrices are symmetric matrices due to the reciprocity of the interaction between each pair of nodes in the grid. The matrix corresponding to the quadratic method is, however, much larger than the matrix of the linear method. The number of nonzero components for the quadratic scheme is $165,742$ while this number is $11,330$ for the linear scheme.

The explicit Dirichlet boundary condition for this problem is approximated by setting the potential of the nodes located on the boundary of the domain to zero. This is done by setting the diagonal component of the coefficient matrix $[K]$ in equation 3.22 for these nodes equal to one (the remainder of the row should be zero) and setting the corresponding component on the right-hand-side of this equation equal to zero. To ensure the efficiency of the approximation of the boundary condition, a zero density region is constructed around the main region.

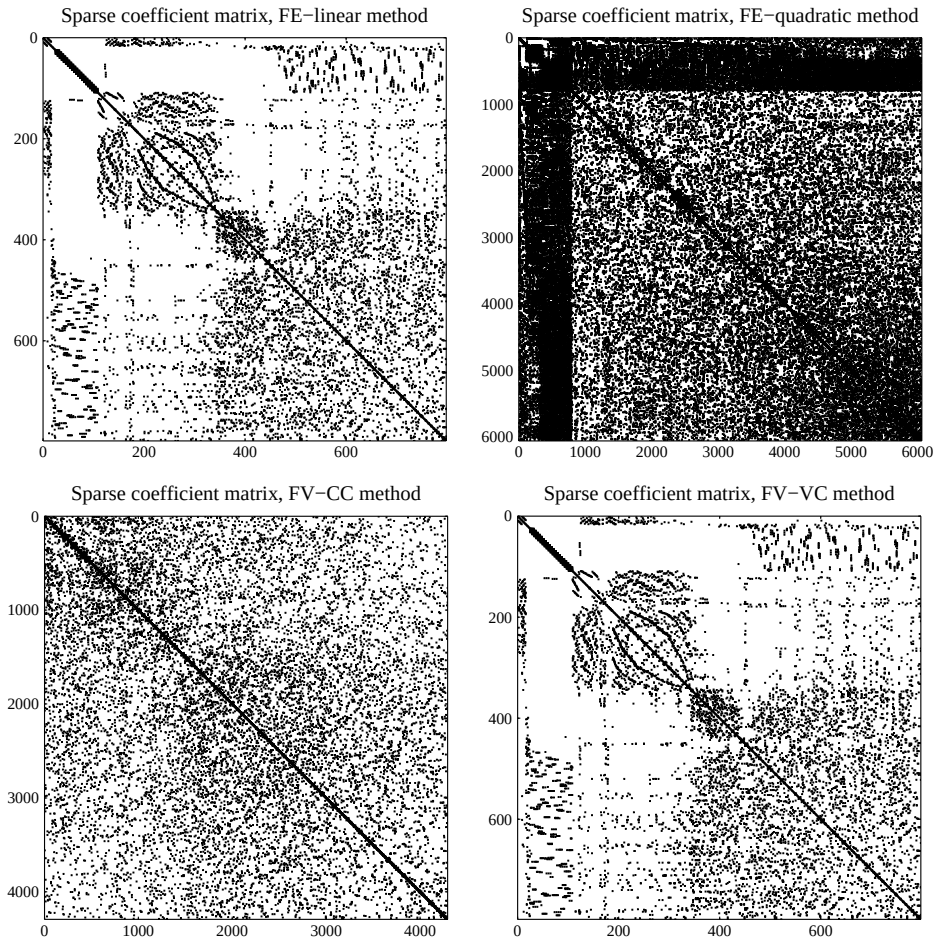


Figure 3.4: These plots show examples of coefficient matrices for the linear and quadratic finite-element schemes (FE-linear and FE-quadratic, top left and right, respectively) and for the cell-centred and vertex-centred finite-volume schemes (FV-CC and FV-VC, bottom left and right, respectively). These matrices correspond to a grid with $4,294$ tetrahedral cells, 798 vertices and $5,266$ tetrahedral edges. The horizontal and vertical axes give the numbers for the rows and the columns of the matrix, respectively, and the black points show the location of the nonzero components. The numbers of nonzero components for the FV-CC and FV-VC matrices are $21,120$ and $11,314$, respectively, and for the FE-linear and FE-quadratic matrices they are $11,330$ and $165,742$, respectively.

In order to exploit the sparsity of the coefficient matrices, the system of equations is solved for the unknown potentials in Compressed Sparse Row (CSR) format using the biconjugate gradient stabilized iterative solver (BiCGStab) from the SPARSKIT package with an ILUT preconditioner (Saad, 1990). (ILUT is a preconditioner based

on a dual Threshold Incomplete LU factorization.) In the FE schemes the coefficient matrices are symmetric and, therefore, other variants of conjugate gradient solvers like BiCG can also be used. However, in order to use a single solver for both FE schemes and FV schemes (where the matrices are not symmetric) BiCGStab and ILUT were used which are both more suitable for non-symmetric matrices (Saad, 1990). The recovery of gravity from the gravitational potential is explained in the next section.

## 3.3 Recovery of gravity from potential

In the FE schemes, the recovery of the vertical component of gravitational acceleration, $g_z$, from the primary solution (i.e., the potential $\phi$) is performed by taking the vertical derivative of equation 3.1:

$$g_z(x,y,z) = \frac{\partial \phi_e(x,y,z)}{\partial z} = \sum_{j=1}^{n} \frac{\partial N_{ej}(x,y,z)}{\partial z} \phi_{ej}. \tag{3.24}$$

In the linear scheme, the approximate gravitational acceleration inside a cell is a constant while in the quadratic scheme it varies linearly inside the cells. The quadratic scheme can also be used to find the gradient of the gravitational field in an arbitrary direction. This gradient, which is a constant inside a quadratic cell, is found by taking a further derivative from the relation above. (The gravity gradient is not treated in this thesis.) By substituting the linear basis functions, equation 3.6, in the relation above, the constant $g_z$ inside a linear element $e$ is obtained as

$$g_z = \frac{1}{6V_e} \left( d_{e1}\phi_{e1} + d_{e2}\phi_{e2} + d_{e3}\phi_{e3} + d_{e4}\phi_{e4} \right), \tag{3.25}$$

which is also equal to $d_e$ in relation 3.5. For the quadratic elements, we should use the basis functions in equation 3.7 which results in the following relation for the

calculation of $g_z$:

$$g_z(x,y,z) = \frac{1}{6V_e}\Bigg( d_{e1}\left(4N^l_{e1}(x,y,z)-1\right)\phi_{e1} + d_{e2}\left(4N^l_{e2}(x,y,z)-1\right)\phi_{e2} + d_{e3}\left(4N^l_{e3}(x,y,z)-1\right)\phi_{e3} + d_{e4}\left(4N^l_{e4}(x,y,z)-1\right)\phi_{e4}\Bigg) + \frac{2}{3V_e}\Bigg( \left(d_{e1}N^l_{e2}(x,y,z) + d_{e2}N^l_{e1}(x,y,z)\right)\phi_{e5} + \left(d_{e1}N^l_{e3}(x,y,z) + d_{e3}N^l_{e1}(x,y,z)\right)\phi_{e6} + \left(d_{e1}N^l_{e4}(x,y,z) + d_{e4}N^l_{e1}(x,y,z)\right)\phi_{e7} + \left(d_{e3}N^l_{e4}(x,y,z) + d_{e4}N^l_{e3}(x,y,z)\right)\phi_{e9} + \left(d_{e2}N^l_{e4}(x,y,z) + d_{e4}N^l_{e2}(x,y,z)\right)\phi_{e10}\Bigg) \tag{3.26}$$

As $g_z$ varies linearly in quadratic elements, it has a higher accuracy compared to the solutions from the linear method. Therefore, in order to achieve the same degree of accuracy in the linear method, higher refinements at the observation points are required.

It is known that the optimal point for sampling the gradient of a solution (here, gravitational acceleration) is the centroid of each tetrahedron (Zienkiewicz and Taylor, 2000). Therefore, for each observation point a regular tetrahedron is inserted inside the grid during the grid's construction such that the observation point is located at the tetrahedron's centroid.

# Chapter 4

# Finite-volume schemes for the forward modelling of gravity data

## 4.1 Introduction

The finite-volume method directly discretizes the integral form of "conservation laws" in space. Some of the features of this method are its relative simplicity of idea, the possibility of application to both structured and unstructured domains and, most importantly, that it satisfies the conservativeness of the numerical flux after discretization (see, e.g., Hirsch, 2007; Eymard et al., 2000). The latter feature, which guarantees the continuity of the physical quantities across the cell boundaries, is achieved by writing a "balance equation" for each control volume. The relative simplicity of the idea behind the finite-volume method makes this technique close to the finite-difference method while its generality and flexibility are similar to the finite-element method. The finite-volume technique uses the integral form of the governing equations which is the most general form (Hirsch, 2007). In this method, for each grid point a small cell, also called a "control volume", is attributed and then the integral form of the conser-

vation law is applied to this volume. Therefore, unlike the finite-difference method where the grid consists of a set of points, in the finite-volume method the grid consists of cells.

For the finite-volume discretization of the governing equations, as mentioned above, the integral form of the equations is applied over the control volumes. Then, the divergence theorem is used to transform the volume integrals into surface integrals over the bounding surfaces of the volumes. Afterwards, the surface flux is approximated using equations which should be independent from the original conservation laws. There exists a wide range of finite-volume techniques based on the choice of the method for the approximation of this surface flux (see, e.g., Eymard et al., 2000). The last step in the discretization is to approximate the unknown quantities by their volumetric or surficial averages. Therefore, in the finite-volume method, the solutions of the problem are the average values of the unknown quantities.

The conservativeness of the finite-volume discretization can be shown by a simple 2-D example: The conservation law for a scalar quantity, $U$, states that there is a balance between the sum of the sources or sinks of that quantity, $Q$, in the domain $\Omega$ and the net amount of this quantity that passes through the boundaries of this region (the amount of $U$ crossing the unit of surface is called the "numerical flux", $\mathbf{F}$):

$$\oint_S \mathbf{F} \cdot d\mathbf{S} = \iint_\Omega Q \, d\Omega, \tag{4.1}$$

where $S$ is the closed boundary of $\Omega$ and $\mathbf{F}$ is positive outward. The important property of the finite-volume method is that it leads to a conservative numerical scheme, i.e., the equations remain conservative after discretization. A non-conservative discretization might lead to numerical sources that result in numerical errors (Hirsch, 2007).

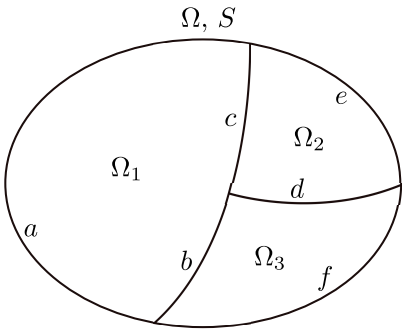


Figure 4.1: Region $\Omega$ with its boundary $S$ is divided into three smaller regions $\Omega_1$, $\Omega_2$ and $\Omega_3$. The smaller boundary segments are indicated with letters $a$, $b$, $c$, $d$, $e$ and $f$ (adapted from Hirsch, 2007).

Equation 4.1 can be written for an arbitrary $\Omega$. If we divide $\Omega$ into three regions, as in Figure 4.1, for the smaller volumes we can write

$$\begin{aligned}
\oint_{a\,b\,c} \mathbf{F} \cdot d\mathbf{S} &= \iiint_{\Omega_1} Q_1 \, d\Omega \\
\oint_{c\,d\,e} \mathbf{F} \cdot d\mathbf{S} &= \iiint_{\Omega_2} Q_2 \, d\Omega \\
\oint_{b\,d\,f} \mathbf{F} \cdot d\mathbf{S} &= \iiint_{\Omega_3} Q_3 \, d\Omega.
\end{aligned} \tag{4.2}$$

Note that the normal flux through a boundary which is common between two regions has different signs for the two regions. For example, while $c$ is common between $\Omega_1$ and $\Omega_2$

$$\int_c \mathbf{F} \cdot d\mathbf{S}|_{\Omega_1} = -\int_c \mathbf{F} \cdot d\mathbf{S}|_{\Omega_2}. \tag{4.3}$$

Therefore, by summing up the equations in 4.2 all the internal flux terms cancel out and what remains forms equation 4.1. Now, if the same property is satisfied after a FV discretization the FV scheme can be called conservative.

In the finite-volume method, the flux, $\mathbf{F}$, and the sources, $Q$, are approximated by their averages, $F$ and $q$, respectively, over the boundaries and the volumes, $V$.

These approximations result in

$$F\,S = q\,V_\Omega, \tag{4.4}$$

which is the discretized form of equation 4.1, and

$$\begin{aligned} F\,S_a|_{\Omega_1} + F\,S_b|_{\Omega_1} + F\,S_c|_{\Omega_1} &= q_1\,V_{\Omega_1} \\ F\,S_c|_{\Omega_2} + F\,S_d|_{\Omega_2} + F\,S_e|_{\Omega_2} &= q_2\,V_{\Omega_2} \\ F\,S_b|_{\Omega_3} + F\,S_d|_{\Omega_3} + F\,S_f|_{\Omega_3} &= q_3\,V_{\Omega_3}, \end{aligned} \tag{4.5}$$

which is the discretization of the relations in equation 4.2. Again, adding up these relations results in equation 4.4 which indicates that no internal flux nor numerical sources are created. This confirms the conservativeness of the finite-volume discretization.

The equation that is discretized using the finite-volume method in this chapter is the conservation law for gravitational potential. In the next sections, two FV schemes are developed that solve for the gravitational potential at the vertices and at the circumcentres of the tetrahedral cells. Gravity is derived from potential using a differencing method. The results from these schemes are presented in the next chapter. The finite-volume method is also used here for the modelling of electromagnetic data which is the subject of the second half of this thesis.

## 4.2 Cell-centred and vertex-centred schemes

Two FV schemes are presented here: a cell-centred (CC) scheme in which control volumes are the tetrahedral cells and the unknown potentials are approximated at the circumcentres of these tetrahedra, and a vertex-centred (VC) scheme in which control volumes are the dual Voronoï cells of the tetrahedra and the potentials are

approximated at the vertices of the tetrahedra. The Voronoï cell for a vertex node is the convex hull formed by the circumcentres of the tetrahedra that share that node. These cells are polyhedra with each polygonal face corresponding to one of the tetrahedral edges that share the central vertex node (see Figure 2.1). In both of the CC and VC schemes, density is constant within the tetrahedral cells. This allows the use of these schemes to find the potential at different locations of a single density distribution. However, for a certain grid the VC and CC control volumes have different configurations which causes different speeds and accuracies for the CC and VC schemes.

Gauss's law (equation 2.36) for gravitational field represents a conservation law by stating that the net flux of the gravitational field through a closed surface is proportional to the internal sources, i.e., the density distribution:

$$\oiint_S \mathbf{g} \cdot \hat{\mathbf{n}}\, ds = -4\pi\gamma \iiint_V \rho\, dv. \tag{4.6}$$

In the FV method, the numerical flux and sources are approximated by their cell-average values. In the CC method, $\rho$ is constant inside each control volume, i.e., tetrahedron. Replacing $\mathbf{g}$ over the faces with averages gives

$$\sum_{i=1}^{4} \mathbf{g}_i \cdot \hat{\mathbf{n}}_i S_i = -4\pi\gamma\rho\, V, \tag{4.7}$$

where $S_i$ and $\hat{\mathbf{n}}_i$ are the area and the unit outward normal to the $i$th face, respectively, $\mathbf{g}_i$ is the average field over this face, and $V$ is the volume of the tetrahedron. In the VC method, the average density of a Voronoï cell is the volume-weighted average of

the densities due to the tetrahedra that form the Voronoï control volume:

$$\sum_{i=1}^{n} \mathbf{g}_i \cdot \hat{\mathbf{n}}_i S_i = -4\pi\gamma \sum_{j=1}^{m} \rho_j V_j, \tag{4.8}$$

where $n$ is the number of faces, $m$ is the number of the tetrahedra whose circumcentres are the vertices of the Voronoï cell, $V_j$ is the volume of the intersection of the Voronoï cell and the $j$th tetrahedron and $\rho_j$ is the density of this tetrahedron. In both of the FV methods presented here, the grid points (i.e., control volume centres) are located at the intersection of the normals of the faces. Therefore, the average outward normal field over the $i$th face of control volume $c$ can be approximated by differencing:

$$\mathbf{g}_i \cdot \hat{\mathbf{n}}_i \approx (\phi_i - \phi_c)/d_i, \tag{4.9}$$

where $\phi_c$ and $\phi_i$ are the potentials at grid points associated with the control volume $c$ and a neighbouring control volume which shares the face $i$ with volume $c$, respectively, and $d_i$ is the distance between these two points (examples for tetrahedral and Voronoï control volumes are given in Figure 4.2). The substitution of this approximation into equations 4.7 and 4.8 gives the balance equations:

$$\phi_c \sum_{i=1}^{4} \frac{S_i}{d_i} - \sum_{i=1}^{4} \frac{S_i}{d_i}\phi_i = 4\pi\gamma\rho V, \tag{4.10}$$

for the CC scheme, and

$$\phi_c \sum_{i=1}^{n} \frac{S_i}{d_i} - \sum_{i=1}^{n} \frac{S_i}{d_i}\phi_i = 4\pi\gamma \sum_{j=1}^{m} \rho_j V_j, \tag{4.11}$$

for the VC scheme. These relations are the discretized forms of Poisson's equation for gravity (equation 2.25) using the finite-volume method on tetrahedral and Voronoï

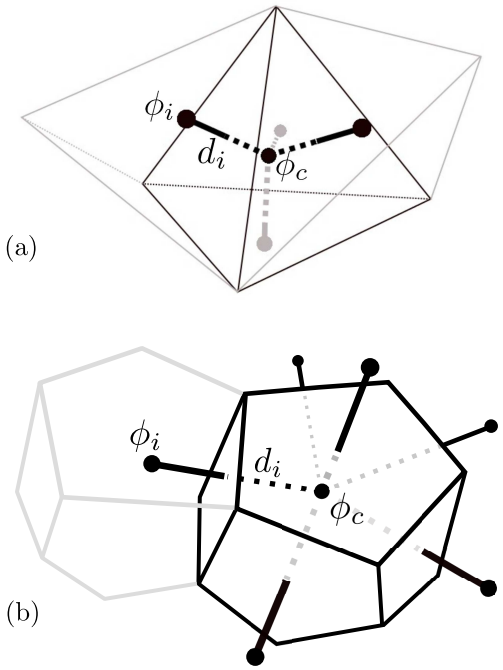


Figure 4.2: The average outward normal field through facet $i$ of control volume $c$ is approximated as the difference between the solutions at the grid points on both sides of this facet ($\phi_c$ and $\phi_i$) divided by their distance ($d_i$). Figures (a) and (b) show examples for the locations of the quantities that are involved in this approximation for tetrahedral and Voronoï faces, respectively.

grids.

Writing these relations for all the control volumes of a grid results in a system of equations like equation 3.22 where the coefficient matrix $[K]$ is a $M \times M$ matrix with $M$ being the number of control volumes, i.e., the number of unknowns. $[K]$ is a highly sparse symmetric matrix in which the nonzero off-diagonal components are $-\frac{S}{d}$ and the diagonal components are the sum of the off-diagonal components. The number of nonzero components inside each row is called the degree of the row. The degree of the row for each grid point equals the number of faces of the control volume surrounding that grid point which is four for the CC scheme and it is an arbitrary number for the VC scheme. $\{\phi\}$ and $\{b\}$ are $M \times 1$ column vectors where $\{\phi\}$ is the vector of unknowns and $\{b\}$ contains the source terms equal to the right-hand-side of

the equations 4.10 or 4.11 for the CC and VC schemes, respectively. Figure 3.4 shows examples of coefficient matrices for the cell-centred and vertex-centred methods. The same figure also shows coefficient matrices for the linear and quadratic FE methods. It can be seen that the nonzero patterns of the matrices of the FV-VC and FE-linear match exactly. This is because of the similar numbers of unknowns and similar degrees of freedom for the two methods. However, the nonzero components of the two matrices possess different values.

The homogeneous Dirichlet boundary condition is imposed by setting the potential of the nodes that are located on the boundary of the domain to zero. In the VC scheme, similar to the FE schemes, there are nodes that are directly located on the boundary. In the CC method, however, the boundary nodes are the circumcentres of the tetrahedra that are attached to the boundary. For both the VC and CC schemes, the rows in the coefficient matrix that correspond to the boundary nodes will only have a single nonzero component equal to one which is the diagonal component. Also, the right-hand-side values for these rows will be zero.

In the finite-volume schemes, the nonzero terms in the coefficient matrices are functions of the lengths of the edges, the areas of the faces and the volumes of the Voronoï and tetrahedral cells. There are standard methods available for calculating the tetrahedral volumes and the areas of the triangles for the tetrahedral grid. For the Voronoï grids, the volumes and the surfaces of the Voronoï cells are split into smaller tetrahedra and triangles and then the Voronoï volumes and areas are found as the sum of the smaller quantities. A Voronoï face is split into triangles which are formed by the centroid of this Voronoï face and the edges of this face, and a Voronoï volume is split into tetrahedra formed by each of these triangles on the faces and the centroid of the Voronoï cell.

As with the finite-element schemes discussed in the previous chapter, the system

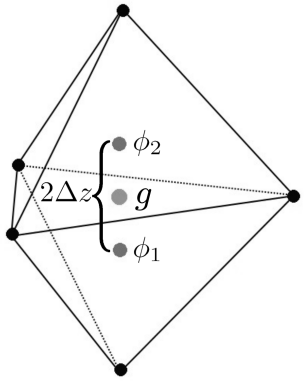


Figure 4.3: The two tetrahedra inserted into the grid for recovering the vertical component of gravitational acceleration at each observation point in the CC scheme. $\phi_1$ and $\phi_2$ are the solutions at the centroids (also circumcentres) of these cells, and $g$ is the observation point.

of equations for the CC and VC schemes are solved in sparse format using the biconjugate gradient stabilized iterative solver (BiCGStab) from the SPARSKIT package with an ILUT preconditioner (Saad, 1990). The solutions from the CC and VC methods are the unknown gravitational potentials at the vertices and at the circumcentres of the tetrahedra, respectively. The recovery of gravity from this potential is explained in the next section.

## 4.3 Recovery of gravity from potential

In this study, the centred-difference scheme was used for finding the vertical component of gravitational attraction ($g_z$) at the points inside the grid. For doing this, two points with known potentials ($\phi_1$ and $\phi_2$) located at the same distance ($\Delta z$) below and above the observation point are required. Then, gravitational acceleration is found by

$$g_z = \frac{\phi_2 - \phi_1}{2\Delta z}. \tag{4.12}$$

In the VC scheme, primary solutions are found at the vertices of the tetrahedra. Therefore, for each observation point two nodes are directly inserted into the grid. These nodes will form tetrahedral vertices and the solutions found at these nodes will be used in the relation above in order to find the gravitational acceleration at the observation point. In the CC method, potentials are found at the circumcentres of the tetrahedra. For this scheme, five nodes are inserted for each observation point such that they form two regular tetrahedra with a common horizontal facet with the observation point located at the centroid of this common facet. In this way, the solutions resolved for the circumcentres of these tetrahedra can be set as $\phi_1$ and $\phi_2$ in the relation above (see Figure 4.3).

It should be noted that the techniques of recovery of gravitational acceleration described above for the FV schemes and for the FE schemes in the previous chapter are post-processing stages and independent from the process of the solution of these schemes. Therefore, as the primary solutions in the VC scheme and the linear FE scheme are found at the same locations in the grid, the methods of recovery of the acceleration for these two schemes can be used interchangeably.

# Chapter 5

# Examples for the forward modelling of gravity data

## 5.1 Introduction

In order to evaluate the four schemes presented here two different models are used. A simple density model comprising a dense cube in a zero density background is employed to analyze the schemes. Then, a realistic geological model is used to evaluate the application of the schemes to complex geometries. In all cases, the numerical results are compared with values computed using the analytic expressions of Okabe (1979) for the vertical component of the gravitational field, and the expressions of Waldvogel (1976) for the gravitational potential.

Different discretizations are used for the simple density model: uniformly discretized grids, in which the mesh quality is the most consistent throughout the grid, are used for assessing the accuracy of the numerical schemes (in terms of primary and secondary solutions) as well as studying the resources required (computation time and memory). However, as one of the main features of the unstructured grids is their

flexibility for the adaptive refinement of the mesh, the accuracy is also assessed for locally refined grids. Here, the local refinement is the side-effect of the insertion of additional nodes. In fact, the insertion of nodes serves two purposes: recovery of gravitational acceleration from the primary solution, which is the main purpose, and causing the grid to be refined at the location of observation points in order to achieve the most accurate results with the lowest possible number of elements. Therefore, the size of the inserted tetrahedra controls the amount of refinement and accuracy of the numerical results.

## 5.2 Example 1: simple model

Figure 5.1 shows vertical sections through three discretizations of the same density model: tetrahedralized uniformly, and locally refined at the observation points. In this model, the entire computational domain is composed of three concentric cubes: a nonzero density mass with dimensions $100 \times 100 \times 100$ metres and density of 2 g/cm$^3$, a zero density wholespace with dimensions $700 \times 700 \times 700$ metres, and an external padding layer also of zero density. For an efficient approximation of the physical boundary conditions for the gravitational potential by Dirichlet boundary conditions, this padding layer should have large dimensions ($10^7 \times 10^7 \times 10^7$ metres was used for the model described above and the results shown in Figure 5.2). However, if the desired solution is gravitational acceleration much smaller dimensions are sufficient ($1000 \times 1000 \times 1000$ metres was used for the results shown in Figures 5.4 and 5.5). (The difference between the powers of $r$ in relations 2.20 and 2.23 for, respectively, gravitational acceleration and potential indicates that the damping of the acceleration with distance is faster than potential.) For the uniform grids, calculation of potential and gravitational acceleration was performed at 21 points along a horizontal profile

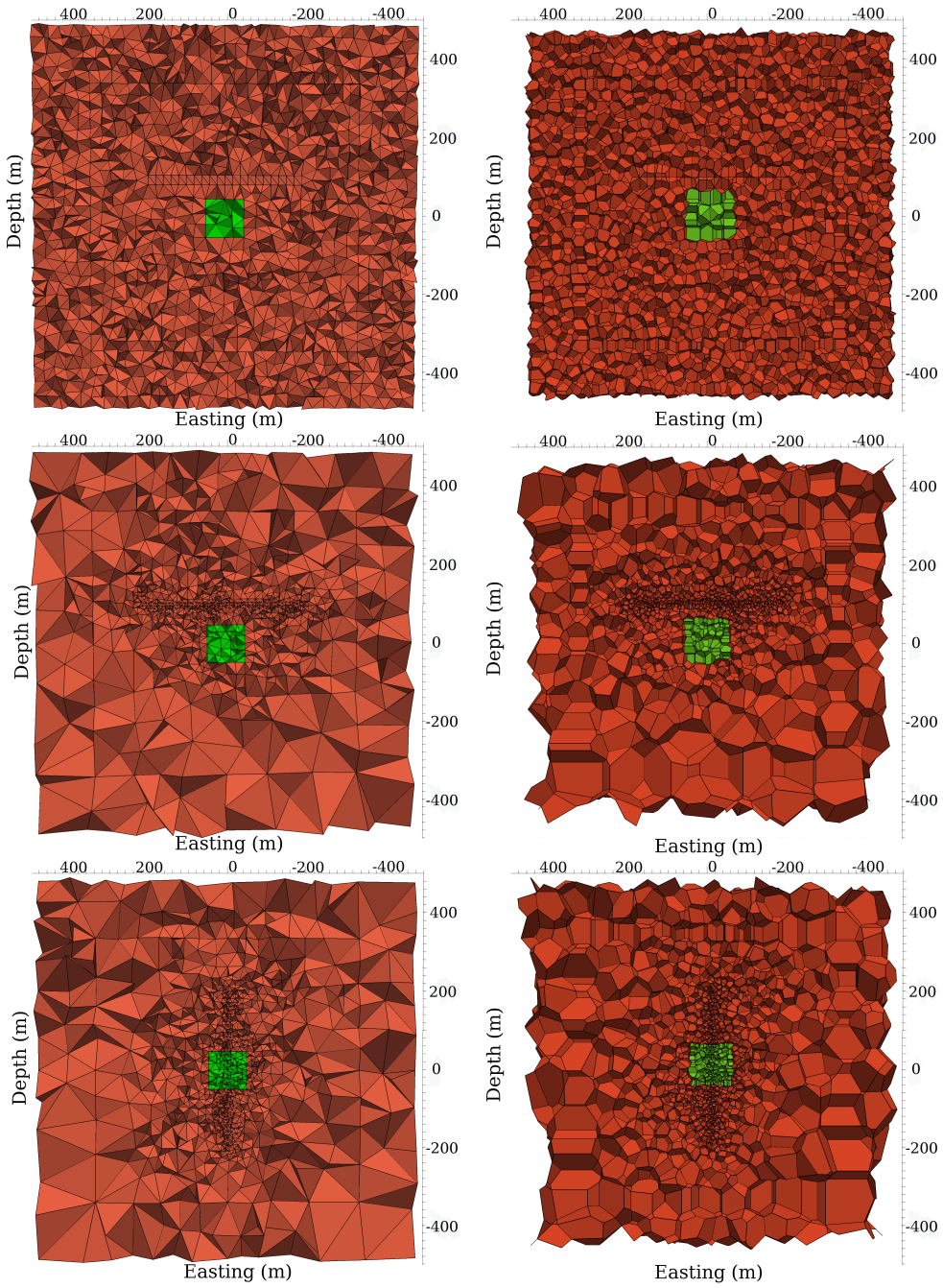


Figure 5.1: Examples of different discretizations of the simple density model. Top: uniform grids. Middle and bottom: locally refined grids for the horizontal and vertical profiles, respectively. The green and red colors correspond to densities of 2 and zero g/cm$^3$, respectively. Left and right figures show tetrahedral and Voronoï grids, respectively.

at the height of 100 metres, northing = 0, and easting between −200 and 200 metres. In addition to this horizontal profile, for the locally refined grids a vertical profile was also considered with the same length passing through the centre of the dense cube (depth from −200 to 200 and with zero easting and northing).

For the uniform grids the average edge size (or cell size) was defined as the cube root of the average volume of the tetrahedra times six. It was explained earlier in Sections 3.3 and 4.3 that for optimizing the recovery of gravity from the gravitational potential nodes are inserted into the grid at the observation locations. However, to avoid disturbing the uniformity of the cells in the uniform grids, the insertion of nodes is only performed for the FV-VC method. The grid that was used for the FV-VC was also used for the FV-CC method but an interpolation was required to find the solutions at the nodes from the solutions at the circumcentres. For the FE methods no node was inserted inside the grids (i.e., observation points were located in arbitrary tetrahedra). For the locally refined grids, on the other hand, the cell size was defined as the size of the edges of the regular tetrahedra inserted for the observation points in the FE methods and the FV-CC method, and as the distance between the two inserted nodes for the FV-VC method (see Sections 3.3 and 4.3).

For the generation of grids, constraints are imposed on the "minimum dihedral angle" in the tetrahedral grid and on the "maximum tetrahedra radius-edge ratio" (i.e., the ratio of the radius of each tetrahedron's circumsphere to its shortest edge). Here, these two constraints are 18 degrees and 1.4, respectively. (These values are chosen based on the experience with TetGen so that the generated mesh is high quality but not too refined.) These constraints increase the quality of the mesh by preventing the generation of very thin or flat tetrahedra. For all the FE and FV methods, the system of equations is solved using the BiCGStab iterative solver with an ILUT preconditioner from the SPARSKIT package (Saad, 1990). *lfil* = 3 and

*droptol* = 0 were used for preconditioning and the target tolerance for the residual norm was $10^{-20}$. (*lfil* is the maximum number of non-zero off-diagonal elements in each row of the triangular matrices in the incomplete LU factorization, and *droptol* sets the threshold for dropping small terms in this factorization.) The computer was a Dell Optiplex desktop with a 3 GHz Dual-Core Intel Q43 processor.

Figure 5.2 shows the primary solutions (i.e., gravitational potential) and their respective errors for the four schemes along the horizontal profile in the locally refined grids described above. Table 5.1 lists the computation time and the 2-norm errors for the different cell sizes (the errors are calculated with respect to analytical solutions). In the FEM-quadratic plot, the graphs of different cell sizes are not distinguishable. As mentioned earlier, satisfying the boundary condition for the gravitational potential requires very large grids. Figure 5.3 gives an example to demonstrate the effect of the grid size on the primary solution. This figure shows solutions for the FV-VC method along the horizontal profile in a locally refined grid. The cell-size at the observation points was 50 metres.

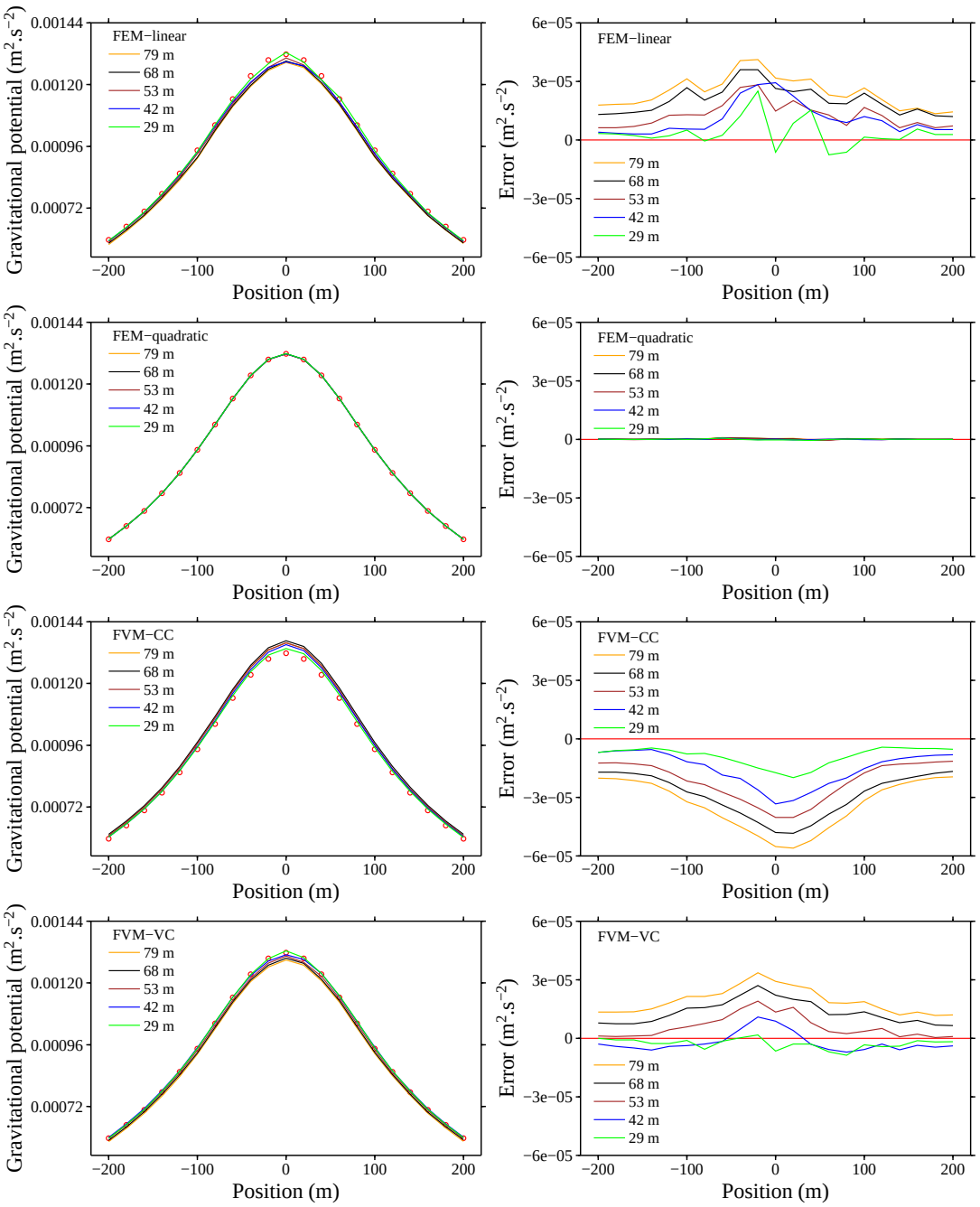


Figure 5.2: Primary solutions (i.e., gravitational potential) and their errors for the horizontal profile in locally refined grids. Results for different cell sizes are plotted with different colors as indicated by the inset legends. Red circles show the analytical solutions using the expressions of Waldvogel (1976).

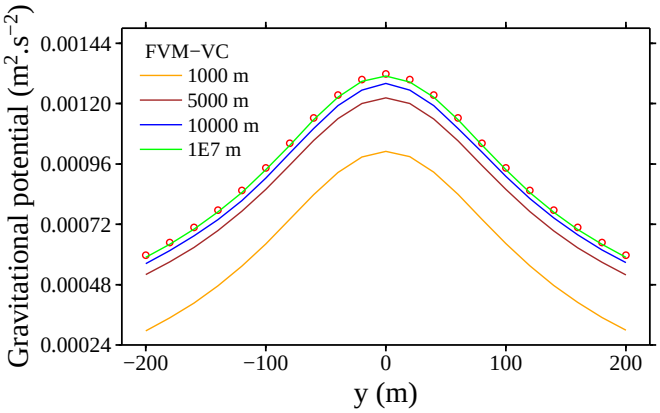


Figure 5.3: The primary solutions for the FV-VC method along the horizontal profile in a locally refined grid where the cell-size was 50 metres at the observation points. Results for different grid sizes are plotted with different colors as indicated via the inset legend.

Table 5.1: Computation times and 2-norm errors for potential for the different cell sizes in Figure 5.2. This table also shows the number of unknowns for each numerical scheme.

| Cell size (m) | No. of tetrahedral elements | FEM-linear (s) , $(m^2.s^{-2})$ No. of unknowns | FEM-quadratic (s) , $(m^2.s^{-2})$ No. of unknowns | FVM-CC (s) , $(m^2.s^{-2})$ No. of unknowns | FVM-VC (s) , $(m^2.s^{-2})$ No. of unknowns |
|---|---|---|---|---|---|
| 79 | 72,558 | 0.7 , 1.2E-4 | 657.3 , 2.0E-6 | 4.0 , 1.6E-4 | 0.6 , 9.2E-5 |
| | | 11,963 | 95,380 | 72,558 | 11,963 |
| 68 | 90,597 | 1.0 , 9.9E-5 | 976.2 , 1.5E-6 | 4.6 , 1.4E-4 | 1.3 , 6.7E-5 |
| | | 14,749 | 118,156 | 90,597 | 14,749 |
| 53 | 142,089 | 2.1 , 6.5E-5 | 1689.4 , 1.0E-6 | 12.4 , 1.1E-4 | 1.7 , 3.7E-5 |
| | | 21,788 | 175,898 | 142,089 | 21,788 |
| 42 | 219,012 | 3.8 , 6.2E-5 | 3521.1 , 9.0E-7 | 23.7 , 8.0E-5 | 3.6 , 2.4E-5 |
| | | 33,953 | 275,248 | 219,012 | 33,953 |
| 29 | 554,730 | 14.6 , 3.6E-5 | 10134.8 , 8.0E-7 | 226.0 , 4.6E-5 | 14.3 , 1.7E-5 |
| | | 93,972 | 764,991 | 554,730 | 93,972 |

Figures 5.4 and 5.5 show the calculated values of the vertical component of the gravitational acceleration and their errors with respect to the analytic values along the horizontal and vertical profiles in the locally refined grids. These figures show the convergence of the numerical solutions to the analytic values with decreasing cell size. The relatively higher error of the linear FE method is due to the fact that in this method gravitational acceleration has a constant value inside each element and, therefore, might have a substantial deviation from the true values inside large elements. In the quadratic FE method, the linear variation of gravitational acceleration inside the elements decreases this error. In Figure 5.5, the FV-CC method shows lower errors compared to the FV-VC method which can be interpreted as the result of the higher number of nodes inserted for each observation point and hence greater refinement for the CC method.

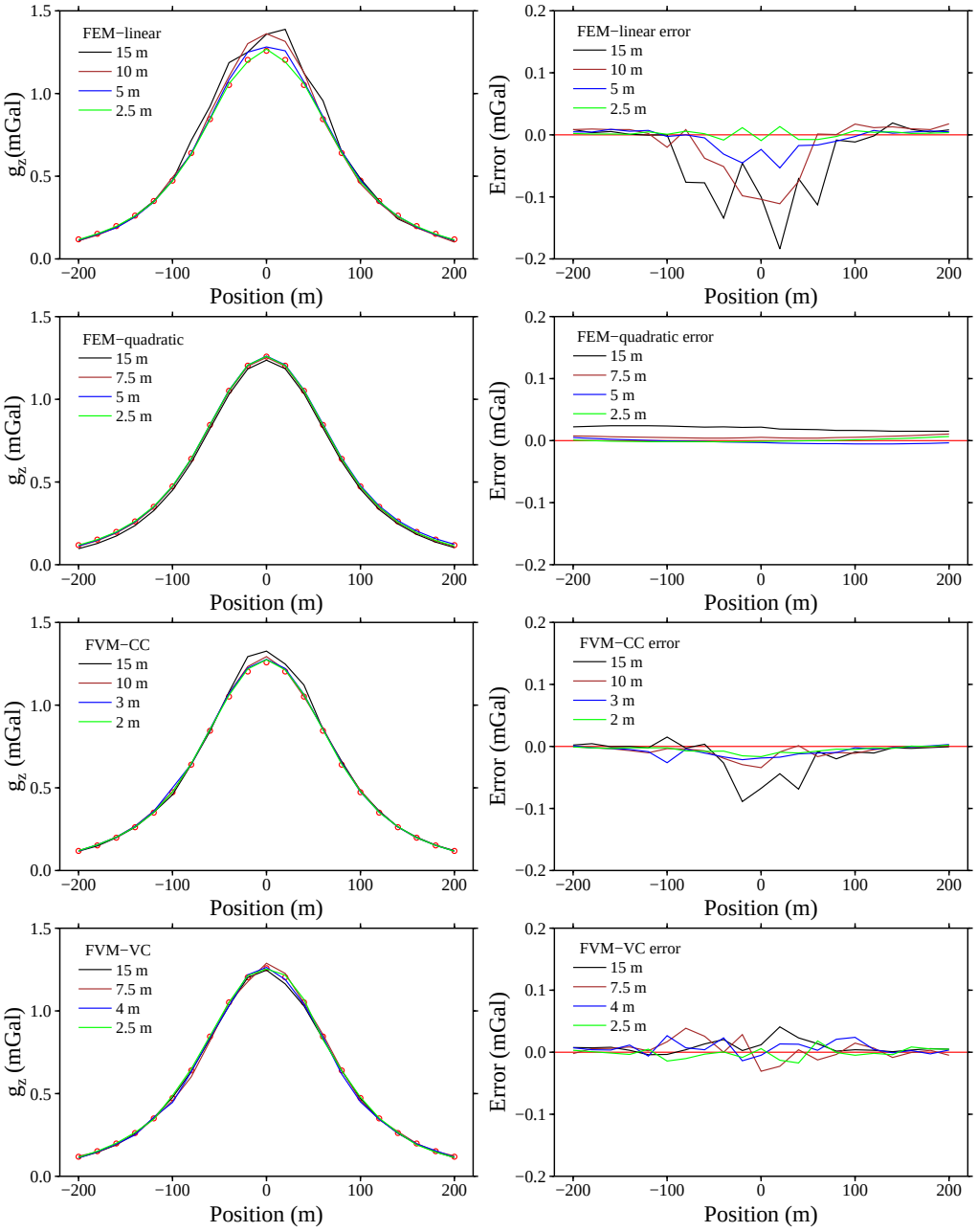


Figure 5.4: The numerical results for gravitational acceleration (left figures) and their errors (right figures) with respect to the analytic values (red circles in the left figures) for the horizontal profile in locally refined grids. Results for different cell sizes are plotted with different colors as indicated by the inset legends.

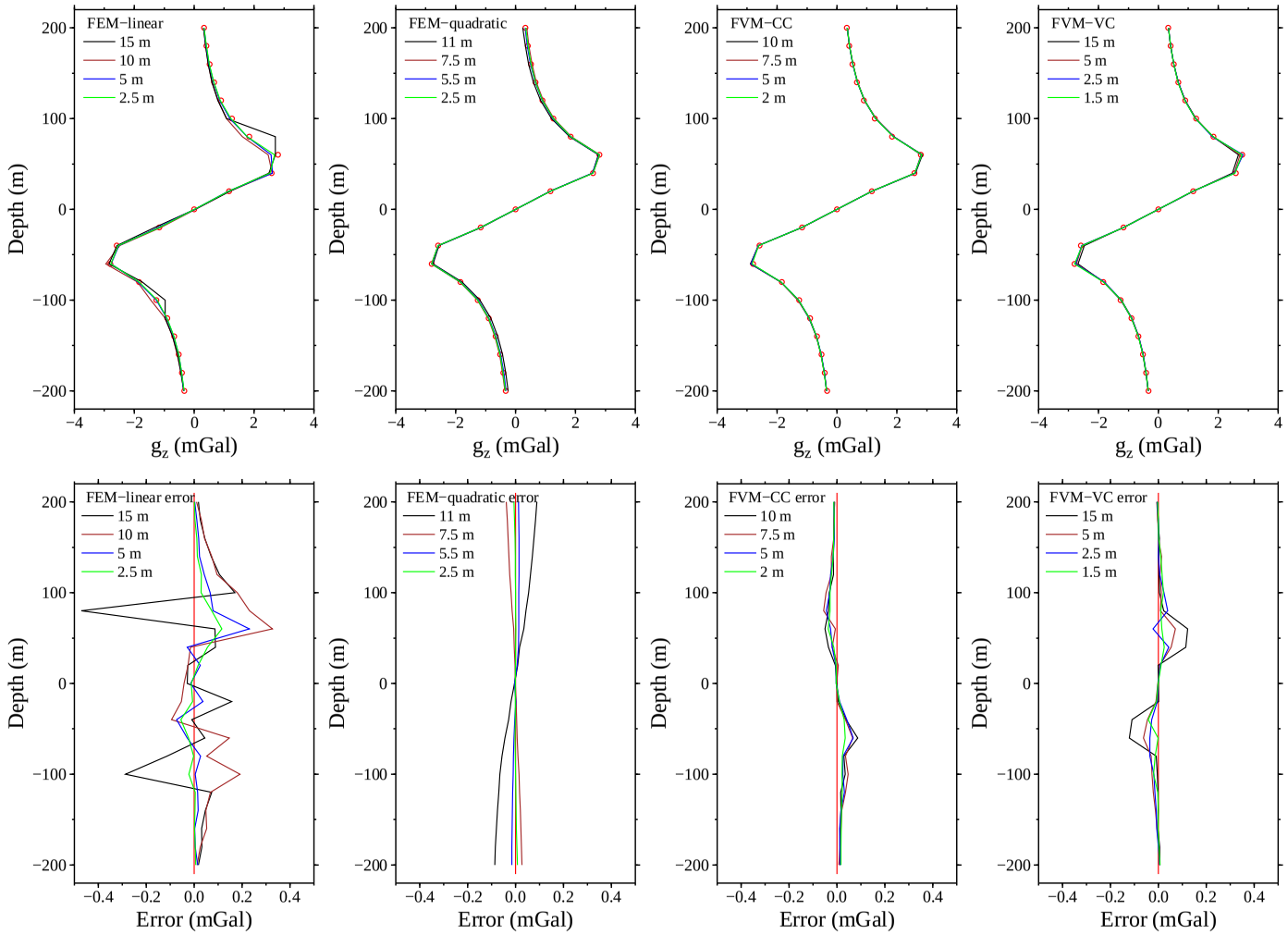


Figure 5.5: The numerical results for gravitational acceleration (top figures) and their errors (bottom figures) with respect to the analytic values (red circles) for the vertical profile in the locally refined grids. Results for different cell sizes are plotted with different colors as indicated by the inset legends.

## 5.3 Accuracy and resource usage

Figures 5.6 and 5.7 show comparisons between the methods in terms of the error estimates for, respectively, the primary solution (gravitational potential) and gravitational acceleration as functions of average cell size (for uniform grids) and cell size (for locally refined grids). Schemes are also compared in terms of computation time and memory usage as functions of the number of tetrahedral elements in the grid (Figure 5.8). The cumulative error is the square root of the sum of the squares of the errors at the observation points. Computation times for the numerical schemes correspond to the time needed for preconditioning and solving the matrix equation by the iterative solver.

As can be seen in Figure 5.6, for the uniform grids and in terms of primary solution (i.e., potential), all the methods are second order accurate, which is the same as for structured rectilinear grids (see, e.g., Farquharson and Mosher, 2009). Comparing this with the fact that FV schemes are only first order accurate over general admissible grids (Eymard et al., 2000) indicates the positive effect of Delaunay triangulation and the imposed quality constraints on the grids. In the locally refined grids, however, the methods show lower orders of accuracy in terms of the primary solution (between orders one and two). For the smallest cell sizes, it can be seen that the cumulative errors level off, which is thought to be due to the approximation of the boundary conditions (Farquharson and Mosher, 2009).

The accuracy of the recovered gravitational acceleration is determined for the uniform as well as refined grids (Figure 5.7). The FE techniques show similar accuracy trends over both kinds of grids (order two for the quadratic FE method and between one and two for the linear FE method), while the FV techniques show slightly lower accuracies on the refined grids (between orders one and two on uniform grids and order one or less for refined grids). This shows the higher sensitivity of the recovery

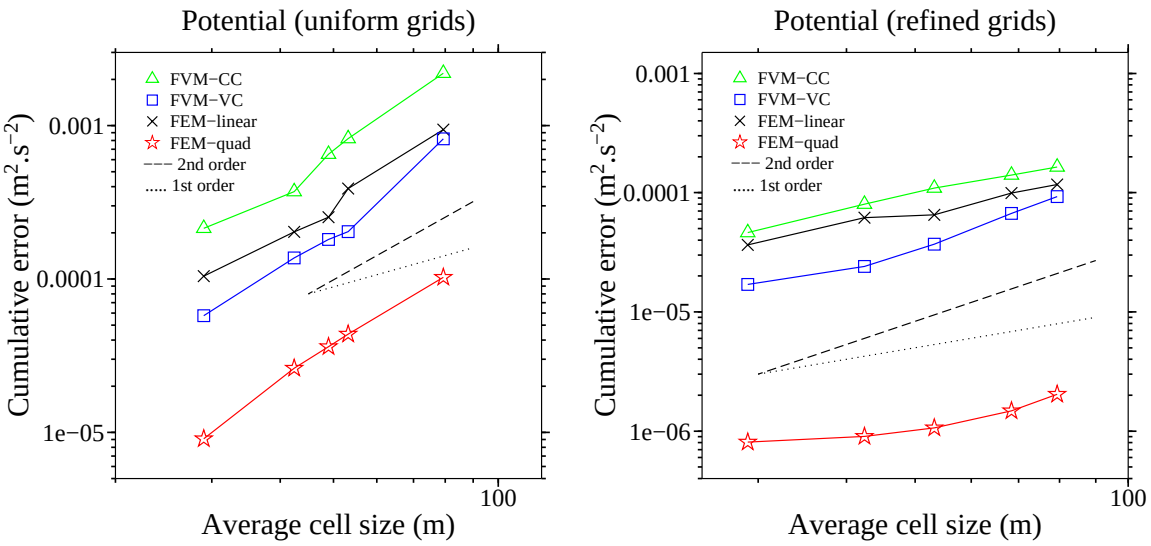


Figure 5.6: Left and right panels show, respectively, the cumulative error for gravitational potential versus the average cell-size for the uniform grids and versus the cell-size for the locally refined grids. The linear FE, quadratic FE, FV-CC and FV-VC are shown by cross, star, triangle and square symbols, respectively. The first and second order trends are shown on each graph by dotted and dashed lines, respectively.

methods used for the FV schemes (discussed in Section 4.3) to the inevitable reduction of grid quality due to local refinement. (While local refinement at a point improves the accuracy of the solution at that point, it decreases the quality of the grid by disturbing the uniformity of the mesh at that location which might adversely affect the order of accuracy.) However, it is observed that for the refined grids the cumulative error of the FV schemes (particularly the FVM-VC) is generally lower than for the linear FE method.

The results for the computation time indicate a second order trend for the FV-CC and first order for the other methods (Figure 5.8). This can be explained by the fact that the increase in the number of tetrahedra linearly increases the number of equations in the FV-CC; it increases the number of equations in the other methods, which are node-based, by a lower rate. The decreasing computation time with increasing number of cells from the second to the third point in the quadratic FE graph is due

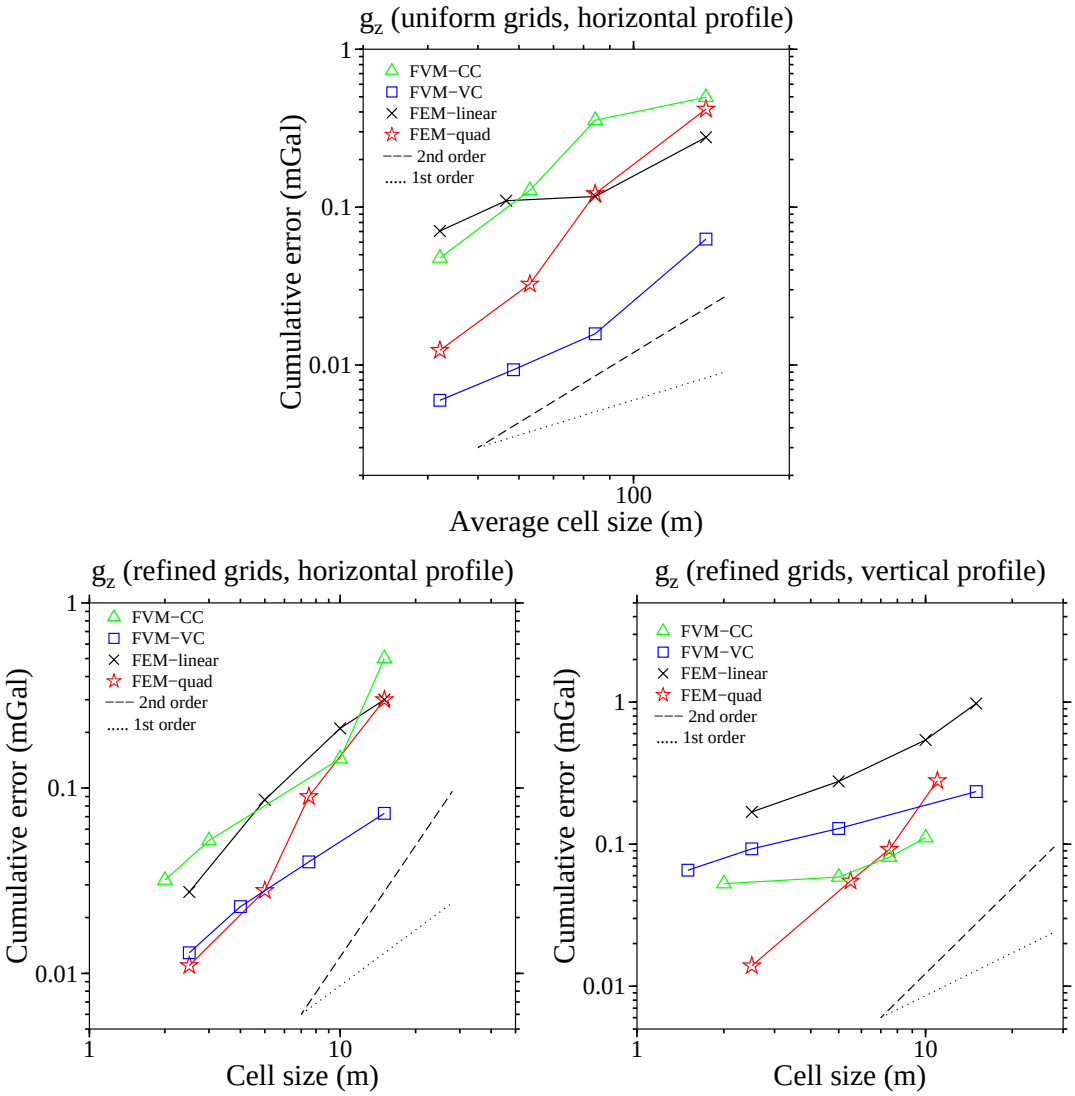


Figure 5.7: Top panel shows for gravitational acceleration the cumulative error versus the average cell-size for the uniform grids. Bottom left and right panels show the accuracy of gravitational acceleration for the horizontal and vertical profiles, respectively, in locally refined grids. The linear FE, quadratic FE, FV-CC and FV-VC are shown by cross, star, triangle and square symbols, respectively. The first and second order trends are shown on each graph by dotted and dashed lines, respectively.

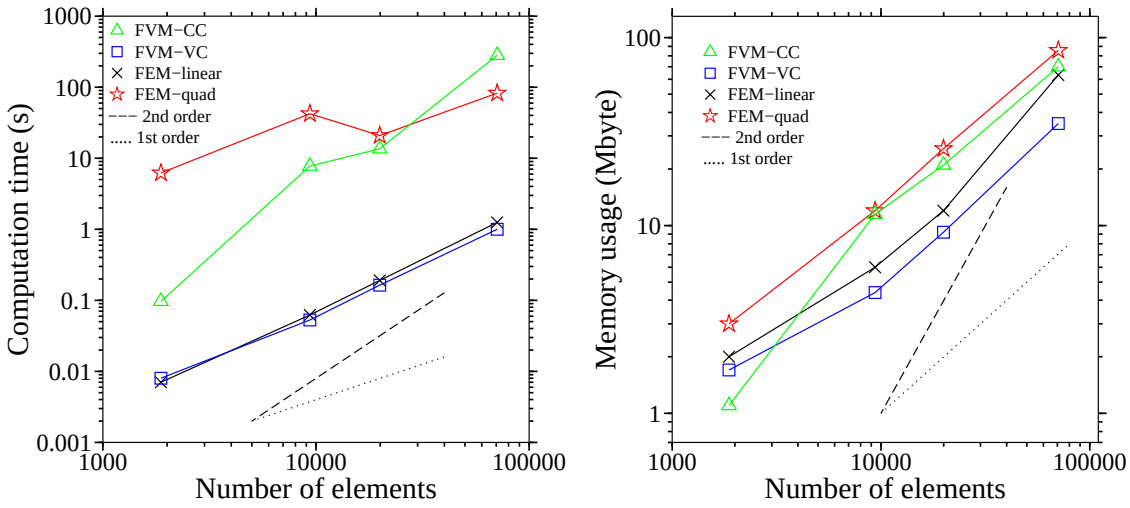


Figure 5.8: Left and right panels show computation time and memory usage as functions of the number of tetrahedral elements, respectively. The linear FE, quadratic FE, FV-CC and FV-VC are shown by cross, star, triangle and square symbols, respectively. The first and second order trends are shown on each graph by dotted and dashed lines, respectively.

to the fact that in unstructured methods computation time depends on both the size of the problem (the number of elements) and the quality of the grid. Sometimes an increase in the number of cells causes a reconfiguration of the whole grid into one with a much higher quality such that the solution is easier (with an iterative solver). (This phenomenon depends on the technique that the mesh generator uses for generating and refining the grids and cannot be predicted.) Finally, the results of the memory usage show a first order trend for all the methods.

## 5.4 Example 2: realistic model

The practicality of the developed methods is evaluated by application to the realistic model shown in Figure 5.9. This model represents the Voisey's Bay massive sulphide deposit located in Labrador, Canada. 58 observation points form two vertical profiles that pass through this body and are located at zero northing, eastings 200 and −150

metres (in a local coordinate system), and elevations from $-60$ to 80 metres. A constant density of 2 g/cm$^3$ is used for the whole body and zero everywhere else. The tetrahedral grids prepared for this model are locally refined at the observation points by inserting the nodes required for each method. The size of the tetrahedra inserted for all the methods is one metre. As examples, vertical sections of the grids generated for the quadratic FE and FV-VC methods are shown in Figure 5.10. Table 5.2 shows the numbers of tetrahedral elements, computation times and the 2-norm errors for each method, and Figure 5.11 shows the gravity data along the two profiles. The large difference between the numbers of elements in the different schemes is the result of the difference in the number of required insertion nodes for different methods (four nodes for each observation point in the FE schemes and five and two nodes for the FE-CC and FE-VC schemes, respectively). The number of elements is also a function of the amount of refinement required to achieve the desired grid quality. This refinement was most necessary at the location of the observation points which were close to the boundary of the mineral deposit where the constrained boundary degraded the quality of the grid. The data from the table show that except for the quadratic FE scheme considerable refinement was required for the other methods.

The results for computation time show that the FV schemes and the linear FE method are efficient in terms of computation time when compared to Okabe's analytical method. Indeed, Okabe's method can compute the gravitational response due to the constant density region in much less time than the values presented in table 2 (0.5 second) taking into account only the surface integral of the boundary of this body. However, in the context of minimum-structure inversion methods the models that emerge during the procedure possess highly complicated density distributions and density is rarely constant from one cell to its adjacent cell. Therefore, here, the computation times due to the numerical schemes have been compared with the times

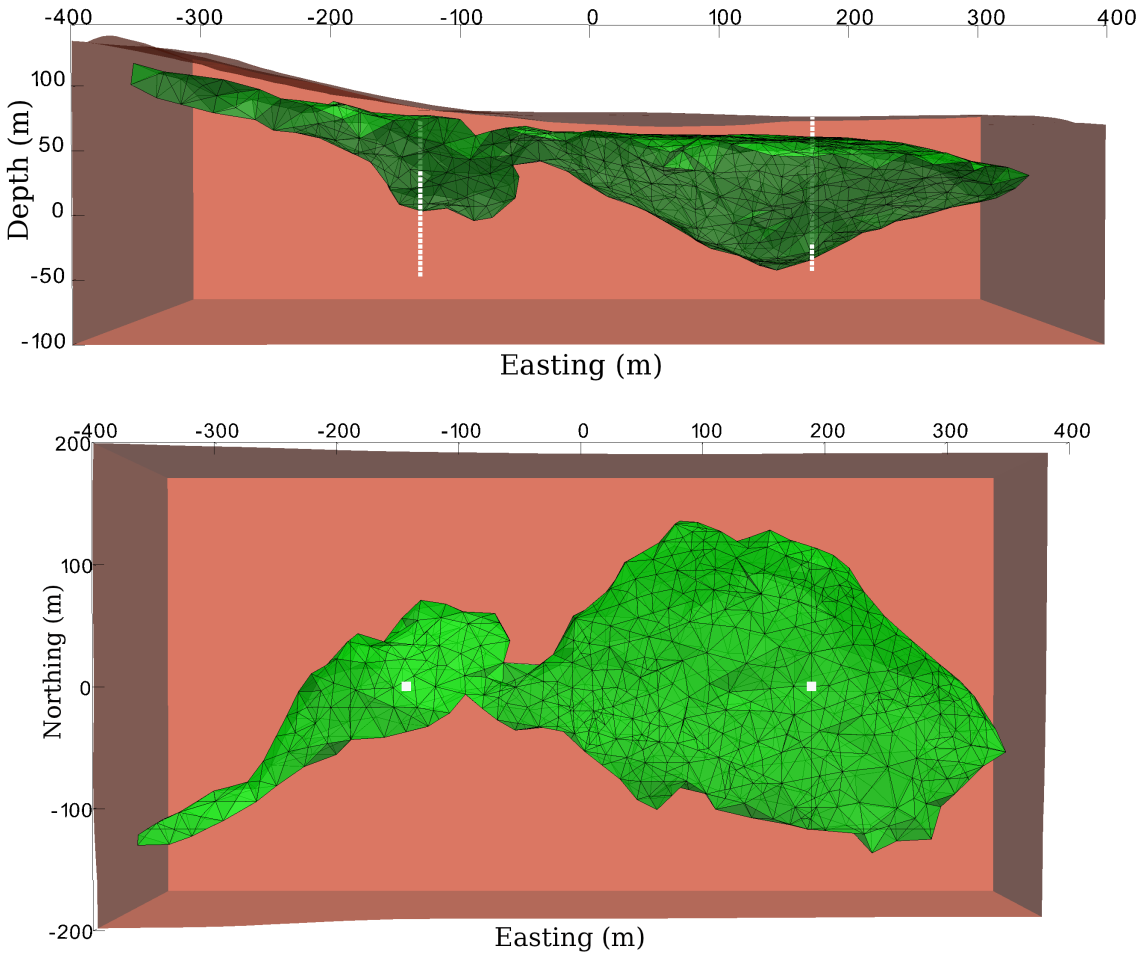


Figure 5.9: Top and bottom images show the side and plan views of the Voisey's Bay deposit, respectively. In these images, the observation points are shown as white filled squares and form two vertical profiles that pass through the body (the body in the top figure is made partially transparent).

for Okabe's method when it considers all the individual cells in the region. The large computation time that is observed for the quadratic FE method can be the result of the worse conditioning of the matrix in this method caused by the relatively low quality of the grid that is used for solving this problem.

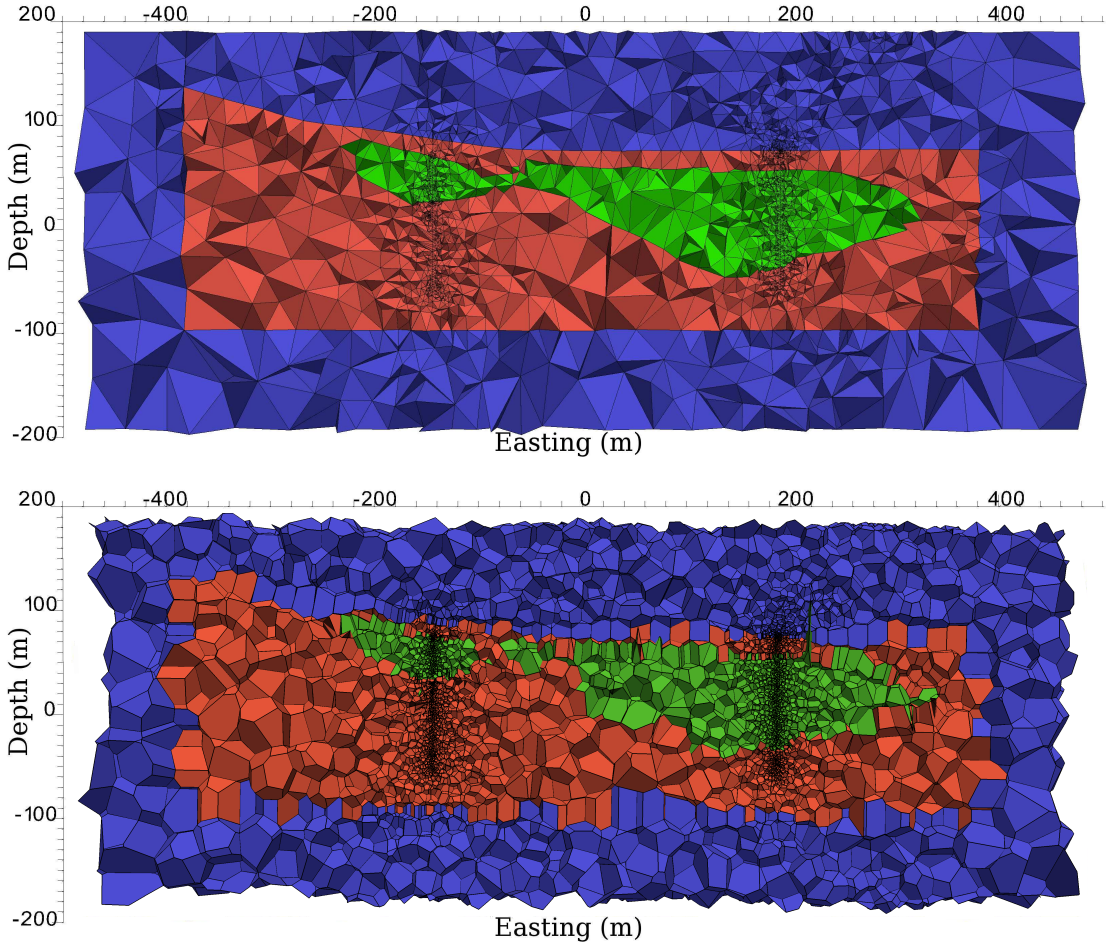


Figure 5.10: Top and bottom images show examples of tetrahedral and Voronoï grids used for the modelling of gravity data for the Voisey's Bay model. These grids were used for the quadratic FE and FV-VC schemes and they show vertical sections at zero northing.

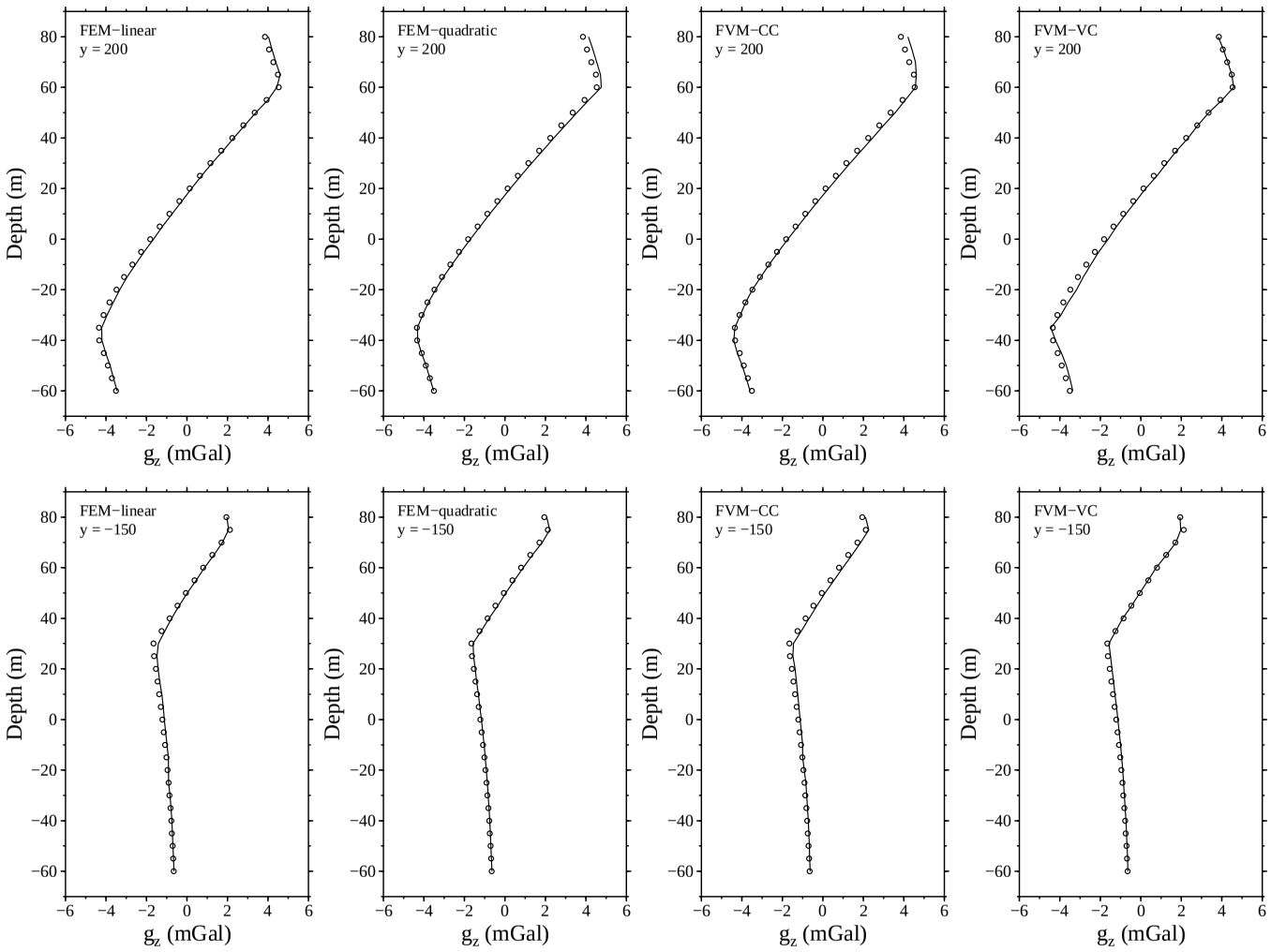


Figure 5.11: Gravity data due to the Voisey's Bay density model along two vertical profiles (at eastings 200 and −150 m) using different numerical schemes. Exact solutions are shown by circles.

Table 5.2: The number of tetrahedral elements in the grids prepared for the Voisey's Bay model and the computation times for different schemes. Table also shows the computation times for Okabe's analytical method (Okabe, 1979) and the 2-norm errors for the two profiles.

| Numerical method | No. of tetrahedral elements | Iterative solver comp. time (s) | Analytical method comp. time (s) | error (mGal) y=200 | error (mGal) y=-150 |
|---|---|---|---|---|---|
| quadratic FE | 140,927 | 1168.3 | 101.5 | 0.83 | 0.39 |
| linear FE | 228,758 | 3.2 | 167.2 | 0.65 | 0.50 |
| cell-centred FV | 176,182 | 15 | 140.2 | 0.85 | 1.97 |
| vertex-centred FV | 154,234 | 1.8 | 122.4 | 2.24 | 0.37 |

## 5.5 Conclusions

The subject of the first half of this thesis was the application of the finite-volume (FV) and finite-element (FE) methods in forward modelling of gravity data using unstructured grids. The main purpose of developing these methods is providing forward solvers for the iterative, gradient-based minimization algorithms used in minimum-structure inversions. These algorithms exploit the sparsity of the matrices used by these forward solvers in order to decrease the amount of memory required for the inversion procedure.

The cell-centred and vertex-centred FV methods employ tetrahedral and Voronoï grids; the linear and quadratic FE methods use linear and quadratic tetrahedral elements. All the schemes are shown to be convergent and second order accurate in terms of the primary solution, i.e., the gravitational potential, on uniform grids. The schemes are also evaluated in terms of the recovered gravitational acceleration on uniform and locally refined grids. The quadratic FE method is second order accurate over both kinds of grids. The other methods are between first and second order accurate on uniform grids. However, on locally-refined grids the FV recovery techniques show lower accuracies.

The application of the schemes to a realistic geological model shows their applicability to complex structures. The quadratic FE scheme is shown to be the most accurate scheme and the least sensitive to the quality of the grid for recovering the vertical component of gravitational acceleration from potential. Therefore, unlike the other schemes, it does not require excessive refinements at the locations with high gradient of solution or with low grid quality. However, this scheme requires higher amounts of computational resources compared to the other schemes. The best trade-offs between accuracy and resource requirements are achieved by the linear FE and FVM-VC which show comparable accuracies and require similar resources.

The FVM-CC is different from the other schemes in that it finds the primary solutions at the circumcentres of the tetrahedra. For a certain grid, FVM-CC requires higher computational resources than the linear FE and FVM-VC while it does not show higher accuracies. The current study has shown that, for the computation of gravitational acceleration, the critical locations in the grid in terms of quality are the observation points around which the grid should be carefully refined. Refinement at the boundary of the dense region is not as crucial. The results also show that for applications in minimum-structure procedures the FV methods and the linear FE method are efficient in terms of computation time when compared to a conventional analytical method.

# Chapter 6

# Numerical modelling of EM data

## 6.1 Introduction

The first chapters of this thesis dealt with the forward modelling of potential field data using the finite-element and finite-volume methods on unstructured tetrahedral and Voronoï grids. The success of the implementations for unstructured grids motivated an attempt at the modelling of electromagnetic (EM) data on unstructured grids. The second half of this thesis investigates the finite-volume modelling of EM data on unstructured staggered grids which is, to the best of our knowledge, new in the field of Geophysics.

For solving the forward electromagnetic problem both numerical and analytical methods exist (Sadiku, 2000). However, the application of analytical methods is restricted to very basic and unrealistic cases. These cases are simple EM sources in homogeneous media or for objects with simple geometries like very thin sheets, spheres or cylinders where the boundaries of the conductive object correspond to constant-coordinate surfaces (Hohmann, 1983). Therefore, numerical methods are the primary tools for modelling purposes in geophysical applications.

The application of numerical methods started in the 1960s with the emergence of modern computers. Currently, the major numerical methods that are used for solving geophysical EM problems are the finite-difference (FD) method, finite-volume (FV) method, finite-element (FE) method and the integral-equation (IE) method. Although the FV method naturally supports unstructured grids, in geophysical EM applications the implementation of this method has been restricted to regular or irregular rectilinear grids. In this thesis, the application of the FV method on unstructured grids is investigated.

In the following sections, first, a literature review on the numerical modelling of EM data on unstructured grids is given. Then, the considerations for the generation of the required unstructured grids are explained and, afterwards, Maxwell's equations and the electromagnetic boundary conditions are presented. There are two main approaches for solving the EM problems. One of them directly solves for the EM fields and the other for the EM potentials. Both of these approaches are considered in this thesis. The next two chapters deal with the modelling of the controlled-source electromagnetic (CSEM) and magnetotelluric (MT) data using the direct approach, and the chapter that follows solves the CSEM problem using the potentials.

## 6.2 Background

Being able to work with an accurate representation of geological structures and interfaces is an important advantage for the numerical schemes that are used for the modelling of geophysical electromagnetic (EM) data. The conventional structured rectilinear grids have limitations in this respect due to the step-like nature of these grids. Also, in the modelling of total field EM data, where the grid needs to be refined at particular locations, the schemes that use structured rectilinear grids produce very

large numbers of cells and, therefore, result in very large problems. Unstructured grids have features which enable them to efficiently model highly irregular interfaces and also to refine the grid locally without affecting the whole grid. Finite-volume (FV) and finite-element (FE) methods both have the ability to directly discretize the governing equations of EM on unstructured grids. Due to their closeness to the finite-difference method, finite-volume schemes can be derived that retain the simplicity of the standard finite-difference methods. One of these finite-difference methods is that of Yee (Yee, 1966) which uses staggered rectilinear grids. The finite-volume method can be used to derive a scheme similar to Yee's scheme on staggered Delaunay-Voronoï grids. As Delaunay and Voronoï grids are mutually orthogonal, the finite-volume scheme displays the simplicity of the original Yee method while providing the features that are particularly favorable for total field EM approaches.

In the numerical modelling of EM data, it is common to separate the total fields into primary and secondary fields and solve the problem only for the secondary fields due to anomalous regions. This is usually done because of the singularity that exists at the EM source location which can cause numerical errors close to the source (Lowry et al., 1989). Unlike the total fields which have high gradients close to the source, the secondary fields due to anomalous regions possess smoother spatial dependence and smaller values compared to the total fields. Therefore, the problems that are solved by this separation approach generally possess higher solution stability and give more accurate results compared to the total field approach (Newman and Alumbaugh, 1995). However, when solving for the secondary fields, the primary fields need to be approximated precisely for the background model using analytical expressions. There is a limitation here if there are topographical features present in the background model because analytical expressions are only available for very simple earth models (Mitsuhata, 2000). As it is difficult for the separation approach to implement irregular

topographical features, the total field methods are preferred in such situations.

Yee's scheme is the standard finite-difference method which has been successfully used for several decades. Being staggered makes this method divergence free, it facilitates the implementation of boundary conditions, and it satisfies the continuity of the tangential components of the EM fields. This scheme is also physically meaningful as Faraday's and Ampère's laws are directly applied over the interleaved contour lines of the grid (for a complete analysis of Yee's scheme see Taflove, 2000). The time-domain Yee method was used in geophysics by Wang and Hohmann (1993), and later by Commer and Newman (2004) and Mulder (2008) for the transient electromagnetic method (TEM), and for marine controlled-source EM (CSEM) by Maaø (2007). In the frequency domain, Madden and Mackie (1989) employed a finite-volume approach to derive a magnetotelluric (MT) scheme using Yee's staggered grid. This approach was further developed for modelling in MT by Mackie et al. (1993) and by Fomenko and Mogi (2002). For CSEM, Newman and Alumbaugh (1995) used the scattered-field version of Maxwell's equations and Haber et al. (2000) used a potential formulation of Maxwell's equations. These methods were extended to fully anisotropic media by Weidelt (1999) and by Weiss and Newman (2002, 2003) (see the review by Börner, 2010, for further references).

The use of rectilinear grids makes Yee's scheme simple and efficient. However, the original scheme uses regular rectilinear grids which are not flexible. One of the early approaches for making refinements possible was using irregular rectilinear grids (i.e., structured rectilinear grids with nonuniform cells). Finite-difference, finite-volume and finite-element methods have been used for this purpose (examples are the references given in the previous paragraph). Although this approach is simple and efficient in terms of accuracy, any local refinement in the grid spreads from that location toward the boundaries of the grid that are parallel to the directions of refinement. This

not only increases the size of the resulting problem, but also adversely affects the conditioning of the problem as the affected cells can have very large aspect ratios (in fact the aspect ratio increases toward the grid boundaries mentioned above). To cope with these issues, OcTree meshes are used by Horesh and Haber (2011). OcTree methods keep many of the advantages of the rectilinear grids but the schemes are more complicated than the original Yee's scheme and they require more cells compared to completely unstructured methods to adapt to topography and irregular interfaces (see, e.g., Figure 3 in Lelièvre et al., 2012).

To derive more flexible schemes, past efforts have tried all the major numerical methods. Finite-difference methods have been proposed that modify the standard Yee method for application on non-rectilinear grids for specific applications (see, e.g., Taflove, 2000; Weiss, 2010). Higher flexibilities are offered by finite-element and finite-volume methods which naturally support unstructured meshes. While the results from these two methods can be comparable they possess different characteristics (Hermeline et al., 2008; Hermeline, 2009). Compared to the FE methods, the FV methods are less mathematically involved, they are simpler in idea, more general and also physically meaningful (see, e.g., Hirsch, 2007). Many different finite-element approaches have been proposed for solving the EM problems which in general solve either for the electric field or for the electric and magnetic potentials using nodal based or edge based elements (e.g., Badea et al., 2001; Li and Key, 2007; Börner et al., 2008; Um et al., 2010; Key and Ovall, 2011; Schwarzbach et al., 2011; Um et al., 2012a,b, 2013; Puzyrev et al., 2013; Schwarzbach and Haber, 2013). (Also, see the reviews by Börner, 2010; Hou et al., 2006; Ansari and Farquharson, 2014, for more finite-element references.) Alternatively, finite-volume schemes have been proposed for general control volumes: Shankar et al. (1990) and Remaki (2000) defined all the fields co-located at the centres of the control volumes while Madsen and Ziolkowski (1990) employed a staggered grid

in which the full 3-D vectors of electric and magnetic fields are defined on the edges of the primary and dual cells, respectively. Also, Yee and Chen (1994, 1997) proposed a slightly different approach by locating the electric and magnetic fields at the vertices of primary and dual cells.

The generalized FV methods mentioned above can be applied on any unstructured configuration. However, the generation of general unstructured grids (e.g., unstructured hexahedral grids) is not a trivial task. Also, these methods lack the efficiency of the original Yee scheme. In particular, for the staggered schemes this is due to the lack of mutual orthogonality between general primary and dual grids. However, there are dual unstructured grids that are mutually orthogonal. The dual tetrahedral-Voronoï configuration is probably the most famous example of this kind and there are programs available for the automatic generation of these grids. The finite-volume schemes based on these grids possess the simplicity of Yee's scheme. The employment of these grids has been presented in the electrical engineering literature for the solution of Maxwell's equations in the time domain (Sazonov et al., 2006; Hermeline, 1993; Xie et al., 2011). In these schemes, the magnetic field remains divergence free, the method is non-dissipative, and it has been shown to be first-order convergent (Hermeline et al., 2008; Nicolaides and Wang, 1998). Here, staggered tetrahedral-Voronoï grids are used for discretizing the governing equations and the applicability of the derived schemes to geophysical applications is investigated.

## 6.3 Mesh generation

As mentioned in the previous section, in this study Delaunay tetrahedral grids and their dual Voronoï grids are used. There are several open-source programs available that use different tetrahedralization methods for the automatic generation of tetrahe-

dral grids. These methods share different characteristics, but the grids generated by them are comparable in terms of grid quality (Sazonov et al., 2007). In this study, TetGen (Si, 2004) was chosen for generating the grids. This program directly generates both the tetrahedral and Voronoï grids that are required. Also, it provides desirable features for inserting nodes inside the mesh. This property is particularly important because the inclusion of sources and interfaces, and any local refinement of the grid, are all performed by implanting nodes inside the mesh. Also, TetGen offers convenient criteria for controlling the quality of the generated tetrahedral grids. This quality directly affects the accuracy of the solutions and also influences the effectiveness of the Dirichlet boundary condition.

The generation of high quality unstructured grids is still an active field of research. However, with some basic knowledge of grid quality, it is possible to generate high quality grids with existing programs. In principle, the quality of a grid is decided by the regularity of the single elements and the uniformity of the grid as a whole (Hirsch, 2007). However, we know that it is not possible to fill the 3-D space with regular tetrahedra. Also, local refinement is one of the main aspects of this work and, therefore, by default we have nonuniform grids. Therefore, instead, we have to generate grids in which single elements are as close to regular tetrahedra as possible and, also, where we have a local refinement the size change from one element to its neighbour is as small as possible. We know that grids with higher qualities are generally those with larger numbers of elements and which result in problems that are more expensive to solve. Therefore, there is always a trade-off between the grid quality and the computation resources.

An important feature of the tetrahedral grids that are generated by TetGen is that these grids are Delaunay. By definition, in Delaunay grids no tetrahedron vertex is located inside the circumscribed sphere of any other tetrahedron. This property

ensures a high quality for the whole grid by maximizing the minimum dihedral angle in the grid. It is proved that any 3-D space can be filled with such a tetrahedralization (Si, 2004). Besides this default quality of Delaunay grids, there are two criteria in TetGen that can be used for controlling the quality of the generated tetrahedral grids (as previously mentioned in Section 5.2). These two criteria serve the same purpose and, therefore, we can use both of them together or use only one of them (Si, 2004). In the next chapters, the only criterion that is considered is the "maximum tetrahedra radius-edge ratio" (i.e., the ratio of the radius of each tetrahedron's circumsphere to its shortest edge). The smaller this ratio the closer the tetrahedra in the grid are to conforming and regular tetrahedra. In TetGen, the default value for this parameter is 2. Based on my experience with TetGen, values between 1.2 down to 1.1 are the appropriate values for generating grids. Using ratios smaller than 1.1 usually results in unnecessarily fine grids for which the solution is too expensive to solve.

For any tetrahedral grid a Voronoï grid can be formed. This "dual" or "secondary" grid is formed for each tetrahedral grid by connecting the circumcentres of adjacent tetrahedra. In other words, a Voronoï cell is formed for each tetrahedral vertex by connecting the circumcentres of the tetrahedra that share that vertex (see Figure 2.1). The most important property of the tetrahedral-Voronoï duality is that these two grids are mutually orthogonal, i.e., the edges of one family of cells are orthogonal to the faces of the other family. This quality is critical in deriving simple discretizations for governing equations. However, in TetGen, unlike for the tetrahedral grid, there is no direct control over the quality of the generated Voronoï grid and the quality of the Voronoï grid depends on the quality of the tetrahedral grid. Several methods exist for generating optimum Voronoï grids (see, e.g., Xie et al., 2011; Du and Wang, 2006). However, these methods are either not automatic or they do not support the local refinement that was needed in this work.

For refinement at the sources and observation locations and for embedding the EM sources, nodes are directly positioned inside the grid. The grid is automatically refined at the insertion locations to satisfy the chosen quality criteria. For each observation point, a regular tetrahedron is inserted by positioning its four vertices inside the grid such that the observation point is located at the centre of the tetrahedron. As magnetic dipoles are defined at the Voronoï edges, for embedding a point magnetic dipole source two regular tetrahedra with a common face are inserted. The point magnetic dipole is then located at the centre of this common face and its direction is given by the line that connects the circumcentres of the two tetrahedra (see, e.g., Figure 7.8 where tetrahedra are inserted for vertical magnetic dipoles). For embedding line sources inside a grid, nodes along the direction of the source are inserted. When the grid is generated, the connection of these nodes gives the desired line source. While the amount of refinement for observation points and magnetic sources is controlled by the size of the inserted tetrahedra, for the line sources it is decided by the number of nodes that are inserted along the line. In this study, no specific refinement was considered at the earth-air interface. The grids were only moderately refined at the boundaries of the anomalous regions by setting a maximum volume for the tetrahedra inside these regions. The relative importance of these refinements is discussed in the next chapter.

## 6.4 Maxwell's equations

The behavior of electromagnetic fields is described by a set of rules that are known as Maxwell's equations. The macroscopic form of Maxwell's equations (in matter) are

$$\oint_C \mathbf{e} \cdot d\mathbf{l} = -\iint_S \frac{\partial \mathbf{b}}{\partial t} \cdot d\mathbf{S} \qquad \nabla \times \mathbf{e} = -\frac{\partial \mathbf{b}}{\partial t} \tag{6.1}$$

$$\oiint_S \mathbf{d} \cdot d\mathbf{S} = \iiint_V \rho \, dV \qquad \nabla \cdot \mathbf{d} = \rho \tag{6.2}$$

$$\oint_C \mathbf{h} \cdot d\mathbf{l} = \iint_S \mathbf{j} \cdot d\mathbf{S} + \iint_S \frac{\partial \mathbf{d}}{\partial t} \cdot d\mathbf{S} \qquad \nabla \times \mathbf{h} = \mathbf{j} + \frac{\partial \mathbf{d}}{\partial t} \tag{6.3}$$

$$\oiint_S \mathbf{b} \cdot d\mathbf{S} = 0 \qquad \nabla \cdot \mathbf{b} = 0, \tag{6.4}$$

where the relations on the left and right represent, respectively, the integral and differential forms of these equations in the time domain (Inan and Marshall, 2011). Relation 6.1 is called Faraday's law. It states that the time-varying flux of the magnetic flux density $\mathbf{b}$ through the contour $C$ which encloses the surface $S$ induces an electromotive force inside $C$ that generates the electric field intensity $\mathbf{e}$. Relation 6.2 is Coulomb's law which says that the net electric flux density $\mathbf{d}$ (also called displacement current) through a closed surface is proportional to the electric-charge volume density $\rho$ that is enclosed by that surface. The third equation (equation 6.3) is Ampère's law which expresses the relation between the line integral of the magnetic field intensity $\mathbf{h}$ around $C$ and the total current enclosed by this contour. The last relation (equation 6.4) is the no-monopole law which indicates there is no magnetic monopole by stating that the net magnetic flux density $\mathbf{b}$ through any closed surface is zero.

In the relations above, $\mathbf{j}$ is the electric current density which can be defined

through the equation of continuity for electric charges:

$$-\oiint_S \mathbf{j}\cdot d\mathbf{S} = \frac{\partial}{\partial t}\iiint_V \rho\, dV \qquad\qquad \nabla\cdot\mathbf{j} = -\frac{\partial\rho}{\partial t}. \tag{6.5}$$

In homogeneous regions of the earth, free charge $\rho$ dissipates in less than $10^{-6}$ s (Stratton, 1941). Therefore, in low-frequency geophysical applications $\partial\rho/\partial t \sim 0$ which results in $\nabla\cdot\mathbf{j} = 0$. However, at the interface between two different media the discontinuity of the normal component of the electric field indicates the accumulation of surface charges (Ward and Hohmann, 1988).

There are constitutive equations in electromagnetism which relate $\mathbf{b}$ and $\mathbf{e}$ to $\mathbf{h}$, $\mathbf{d}$ and $\mathbf{j}$. These relations are

$$\mathbf{d} = \epsilon\,\mathbf{e} \quad ; \quad \mathbf{h} = \mu^{-1}\mathbf{b} \quad ; \quad \mathbf{j} = \sigma\mathbf{e}, \tag{6.6}$$

where $\epsilon$, $\mu$ and $\sigma$ are the permittivity, permeability and conductivity of the media, respectively. Here, we assume that these quantities are independent of time, temperature and pressure and all the earth materials are linear and isotropic. Therefore, although in general these quantities are complex tensors, they are considered as real scalars here.

Alternatively, Faraday's and Ampère's laws can be written in the frequency domain (time-harmonic) using the Fourier transform as

$$\nabla\times\mathbf{E} = -i\omega\mathbf{B} \tag{6.7}$$

$$\nabla\times\mathbf{H} = \mathbf{J} + i\omega\mathbf{D}, \tag{6.8}$$

where $i = \sqrt{-1}$ and $\omega$ is the angular frequency. There is an $e^{i\omega t}$ time dependence and

the Fourier transform pair that was used is

$$F(\omega) = \int_{-\infty}^{+\infty} f(t) e^{-i\omega t} dt \tag{6.9}$$

$$f(t) = \frac{1}{2\pi} \int_{-\infty}^{+\infty} F(\omega) e^{i\omega t} d\omega. \tag{6.10}$$

By taking the curl of the time-domain Faraday's and Ampere's laws and using the constitutive relations for homogeneous media we have

$$\begin{aligned} \nabla \times \nabla \times \mathbf{e} + \mu \nabla \times \frac{\partial}{\partial t} \mathbf{h} = 0 \\ \nabla \times \nabla \times \mathbf{h} - \epsilon \nabla \times \frac{\partial}{\partial t} \mathbf{e} = \sigma \nabla \times \mathbf{e}. \end{aligned} \tag{6.11}$$

As $\mathbf{h}$ and $\mathbf{e}$ are piecewise continuous and possess continuous first and second derivatives the operators $\nabla\times$ and $\partial/\partial t$ can be interchanged. By substituting $\nabla \times \mathbf{e}$ and $\nabla \times \mathbf{h}$ from, respectively, Faraday's and Ampère's laws, by using the vector identity 2.11, and with the knowledge that $\nabla \cdot \mathbf{e} = 0$ and $\nabla \cdot \mathbf{h} = 0$ in homogeneous regions we obtain the symmetric pair

$$\begin{aligned} \nabla^2 \mathbf{e} - \mu\epsilon \frac{\partial^2 \mathbf{e}}{\partial t^2} - \mu\sigma \frac{\partial \mathbf{e}}{\partial t} = 0 \\ \nabla^2 \mathbf{h} - \mu\epsilon \frac{\partial^2 \mathbf{h}}{\partial t^2} - \mu\sigma \frac{\partial \mathbf{h}}{\partial t} = 0, \end{aligned} \tag{6.12}$$

which gives the wave equations for the electric and magnetic fields in the time domain. The equivalent frequency-domain pair is

$$\begin{aligned} \nabla^2 \mathbf{E} + \left(\mu\epsilon\omega^2 - i\mu\sigma\omega\right) \mathbf{E} = 0 \\ \nabla^2 \mathbf{H} + \left(\mu\epsilon\omega^2 - i\mu\sigma\omega\right) \mathbf{H} = 0, \end{aligned} \tag{6.13}$$

which are also known as Helmholtz equations in **E** and **H**. In the above equations, the expression in parenthesis is called the wave number usually depicted as $k$. For frequencies smaller than $10^5$ Hz (which is commonly the case in geophysical surveys) and for common values of $\mu$, $\epsilon$ and $\sigma$ of earth materials, it can be seen that $\mu\epsilon\omega^2 << \mu\sigma\omega$. This suggests that for common geophysical applications displacement currents in the earth are much smaller than conduction currents and, therefore, may be neglected. This assumption is usually called the quasi-static approximation which transforms the wave equations above into

$$\begin{aligned} \nabla^2\mathbf{e} - \mu\sigma\frac{\partial\mathbf{e}}{\partial t} &= 0 \\ \nabla^2\mathbf{h} - \mu\sigma\frac{\partial\mathbf{h}}{\partial t} &= 0, \end{aligned} \tag{6.14}$$

and

$$\begin{aligned} \nabla^2\mathbf{E} - i\mu\sigma\omega\mathbf{E} &= 0 \\ \nabla^2\mathbf{H} - i\mu\sigma\omega\mathbf{H} &= 0. \end{aligned} \tag{6.15}$$

These relations are diffusion equations for the electric and magnetic fields in homogeneous media. In these equations, the wave number is

$$k = (-i\mu\sigma\omega)^{1/2}. \tag{6.16}$$

An important result of the solution of the diffusion equations is that the electromagnetic wave is attenuated inside the earth (Ward and Hohmann, 1988). In fact, it can be shown that in the medium the amplitudes of **e** and **h** reduce by a factor of $1/e$

over the distance $\delta$ known as the skin depth which is given by

$$\delta = \left(\frac{2}{\omega\mu\sigma}\right)^{1/2}. \tag{6.17}$$

All the relations presented thus far in this section directly use the electric and magnetic fields. They are based on the "direct EM-field formulation" of Maxwell's equations. An alternative common formulation is based on electric and magnetic potentials. As a result of the no-monopole law (equation 6.4) and the Helmholtz theorem (equation 2.8), the magnetic flux density can be written as the curl of a vector, $\mathbf{a}$, defined as the magnetic vector potential:

$$\mathbf{b} = \nabla \times \mathbf{a}. \tag{6.18}$$

The substitution of this expression into Faraday's law and, again, using the Helmholtz theorem results in

$$\mathbf{e} = -\frac{\partial \mathbf{a}}{\partial t} - \nabla\phi \tag{6.19}$$

or

$$\mathbf{E} = -i\omega\mathbf{A} - \nabla\phi \tag{6.20}$$

in the frequency domain. In this relation, $\phi$ is called the electric scalar potential. The substitution of $\mathbf{E}$ from the relation above into Maxwell's equations results in the potential formulation or the A-$\phi$ formulation of Maxwell's equations. The scalar and vector potentials are not unique: any function whose curl is zero can be added to the vector potential, $\mathbf{a}$, without altering the value of $\mathbf{b}$. To keep the electric field unique, equation 6.19 suggests that $\phi$ should also be changed accordingly. Such changes in the values of vector and scalar potentials are called "gauge transformations" (Griffiths, 1999). This freedom of choosing the values of the potentials can be exploited to adjust

the divergence of $\mathbf{a}$ (i.e., gauge fixing). The simplest choice is a vanishing divergence:

$$\nabla \cdot \mathbf{a} = 0, \tag{6.21}$$

which is called the "Coulomb gauge". In Chapters 7 and 8, the CSEM and MT problems that are solved are based on the direct EM-field formulation. In Chapter 9, the CSEM problem is based on the potential formulation and the Coulomb gauge is used. In the next section, the boundary conditions for the geophysical EM problem are introduced.

## 6.5 Boundary conditions

The geophysical EM problem is a boundary value problem, i.e., a solution of this problem should satisfy both the differential equation of the problem and the boundary conditions. The boundary conditions of the EM problem are specific conditions that exist at the interfaces of the media with different EM properties and at the outer boundaries of the numerical domain. In this section, these conditions for the EM fields are briefly introduced.

The boundary conditions at the interface between two media, 1 and 2, can easily be derived by integrating Maxwell's equations (the integral from of Maxwell's equations) over infinitesimal Gaussian pill-boxes or rectangular loops at an interface (see, e.g., Jin, 2002). These conditions for the tangential and normal components of the

electromagnetic fields can be summarized as

$$E_{t1} = E_{t2} \tag{6.22}$$

$$J_{n1} = J_{n2} \tag{6.23}$$

$$H_{t1} = H_{t2} \tag{6.24}$$

$$B_{n1} = B_{n2} \tag{6.25}$$

$$D_{n2} - D_{n1} = \rho_s, \tag{6.26}$$

where subscripts $t$ and $n$ denote the tangential and normal components, respectively. Note that equation 6.23 is the result of the stationary situation where $\partial\rho/\partial t = 0$.

The boundary conditions 6.22-6.26 show that the tangential components of the electric field, $E_t$, and magnetic field intensity, $H_t$, are continuous across interfaces. Also, the normal components of the electric current density, $J_n$, and magnetic flux density, $B_n$, are continuous across interfaces between two arbitrary media. However, the normal component of the electric displacement current, $D_n$, is discontinuous due to the accumulation of a surface-charge density, $\rho_s$, at the interface. The combination of equations 6.23 and 6.26 shows that the amount of this charge density depends on the values of conductivities of the two media and the values of $E_{n1}$ and $E_{n2}$ (Ward and Hohmann, 1988). In the next chapter, the direct EM-field formulation of Maxwell's equations is considered. In this method, the solution of the problem is the electric field and, therefore, the only condition that needs to be satisfied is equation 6.22. This condition is automatically satisfied here as the electric field is defined along the tetrahedral edges of the grid and the tetrahedral grid is piecewise constant with respect to conductivity.

Similarly, the interface conditions for the EM potentials can be derived by integrating Maxwell's equations in terms of the scalar and vector potentials ($\phi$ and $\mathbf{A}$)

over infinitesimal Gaussian pill-boxes:

$$\mathbf{A}_{t1} = \mathbf{A}_{t2} \tag{6.27}$$

$$\mathbf{A}_{n1} = \mathbf{A}_{n2} \tag{6.28}$$

$$\sigma_1(\mathbf{A} + \nabla\phi)_{n1} = \sigma_2(\mathbf{A} + \nabla\phi)_{n2} \tag{6.29}$$

$$\nabla\phi_{n2} - \nabla\phi_{n1} = \frac{\rho_s}{\epsilon}. \tag{6.30}$$

As for the electric field, the first condition is automatically satisfied here because the vector potential is defined at the same location as the electric field (along the tetrahedral edges). The other three conditions do not need to be considered here because the normal components of $\mathbf{A}$ and $\nabla\phi$ do not intersect the interfaces that separate two different media.

As mentioned in the previous section, the diffusion equations (6.15) indicate that the EM fields attenuate inside a conductive region. This means that if the EM sources are located inside the numerical domain (as in the CSEM methods) and they are far enough away from the boundaries of the domain, then the EM fields vanish on the boundaries. This is the condition that is considered in this thesis and it is called the homogeneous Dirichlet boundary condition. There are other boundary conditions that do not need to approximate the infinity with very large grids (see, e.g., Zhdanov et al., 1997). However, these methods are more complicated. Also, one of the advantages of unstructured grids is that they can increase the size of the grid without an excessive increase in the number of cells.

The boundary condition that is considered for the MT problem in Chapter 8 is the inhomogeneous Dirichlet boundary condition. For this condition, analytical expressions for a 1-D earth are used as the constant values of the electric field at the top and at the bottom of the numerical domain and also the decreasing values of this

field on the vertical sides of the domain.

The boundary conditions explained in this section are parts of the modelling problems that are dealt with in the next three chapters. The next chapter investigates the solution of the CSEM problem using the direct EM-field formulation of Maxwell's equations.

# Chapter 7

# Finite-volume modelling of CSEM data using the direct EM-field formulation

## 7.1 Introduction

This chapter deals with the finite-volume modelling of CSEM data on unstructured staggered grids using a direct EM-field formulation. The idea is to replace the conventional staggered rectilinear grids with staggered tetrahedral-Voronoï grids (see Figure 7.1). In this manner, this method can be seen as a generalization of the finite-volume method employed, for example, by Madden and Mackie (1989) or, from another perspective, as the simplification of the scheme proposed by Madsen and Ziolkowski (1990). Unstructured grids not only provide a greater flexibility for modelling complex geometries and interfaces, but they also allow local refinement of the grid where high gradients of the EM fields are present such as at the EM sources, in the total field approaches, and at interfaces that separate regions with high conductivity

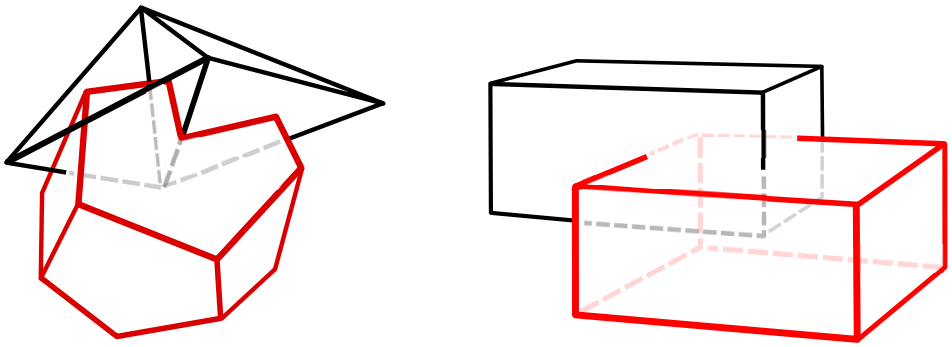

Dual tetrahedral-Voronoï grid

Dual rectilinear grid

Figure 7.1: Examples of the relation between the primary and dual cells in staggered grids. The figure on the right shows an example for the staggered rectilinear grids and the figure on the left shows an example for the unstructured staggered grids that are used in this study.

contrasts.

The finite-volume scheme developed here solves the time-harmonic Helmholtz equation for the electric field in isotropic media (in principle, it can be extended to handle anisotropic media according to Madsen and Ziolkowski, 1990). To the author's best knowledge, this is the first application of a finite-volume scheme on completely unstructured grids for solving the geophysical EM forward problem. Here, the solution is the projection of the total electric field along the edges of the tetrahedral elements. The solutions at these edges are then used to calculate the electric and magnetic fields at any point inside the grid by interpolation. For this interpolation, the edge vector interpolation functions of the tetrahedral elements are used.

In the following sections, first, the governing equations are presented. Then, they are discretized using staggered tetrahedral-Voronoï grids and, finally, the applicability of the scheme is shown by giving examples which represent common geophysical survey contexts. These examples show the capability of the presented scheme for calculating the responses of anomalous body-in-halfspace models to geophysical electric and

magnetic sources. The first two examples represent benchmark solutions to assess the accuracy of the scheme. Using the model in the second example, the parameters that affect the accuracy of the solutions in an unstructured grid are also discussed. The third example represents a realistic model with complex geometry and topography and the solutions are compared with real HEM (helicopter-borne EM) data.

## 7.2 The CSEM problem

The version of Maxwell's equations that is used in low-frequency geophysical applications has particular properties. First, the common values of permeability, permittivity and conductivity of the subsurface materials and the frequencies that are used in the electromagnetic studies of the subsurface are consistent with the quasi-static approximation which is equivalent to ignoring the displacement current everywhere in the earth (Grant and West, 1965). Second, as the materials in the earth's crust are only weakly magnetic the permeability of the subsurface rocks can be approximated by the permeability of free space ($\mu$=$\mu_0$). Moreover, in electromagnetic methods, the primary source of the EM fields can be either an impressed electric current density, $\mathbf{J}_p$, or magnetic dipole moment, $\mathbf{M}_p$ (Hohmann, 1983). Therefore, at any point the total electric and magnetic fields ($\mathbf{E}$ and $\mathbf{H}$) are related by the following form of Maxwell's equations in the frequency domain:

$$\nabla \times \mathbf{E} = -i\omega\mu_0\mathbf{H} - i\omega\mu_0\mathbf{M}_p \tag{7.1}$$

$$\nabla \times \mathbf{H} = \sigma\,\mathbf{E} + \mathbf{J}_p, \tag{7.2}$$

where $\sigma$ is conductivity, $\omega$ is angular frequency, $i$ is the imaginary unit and a time-dependence of $e^{i\omega t}$ is assumed. Taking the curl of equation 7.1 and substituting in 7.2

gives the Helmholtz equation for electric field:

$$\nabla \times \nabla \times \mathbf{E} + i\omega\mu_0\sigma\mathbf{E} = -i\omega\mu_0\mathbf{J}_p - i\omega\mu_0(\nabla \times \mathbf{M}_p). \tag{7.3}$$

In this study, this equation is solved for the electric field as a Dirichlet problem which assumes a zero field at infinity. The electric and magnetic sources can be characterized as

$$\mathbf{J}_p = J_p\,\hat{\mathbf{u}}\,\delta(\mathbf{x} - \mathbf{x}_s) \tag{7.4}$$

$$\mathbf{M}_p = M_p\,\hat{\mathbf{u}}\,\delta(\mathbf{x} - \mathbf{x}_s), \tag{7.5}$$

where $J_p$ and $M_p$ are the magnitudes of the sources, $\mathbf{x}_s$ is the position vector, $\hat{\mathbf{u}}$ gives the direction, and $\delta$ is the Dirac delta function.

## 7.3 Discretization of the problem

The finite-volume method uses the integral form of Maxwell's equations applied over the Delaunay and Voronoï faces of the grid (an example of the relation between these grids is shown in Figure 2.1). It is the tetrahedral grid that is piecewise constant with respect to conductivity. Therefore, in order to maintain the continuity of the tangential component of the electric field at the boundaries of regions with different conductivities, the electric (magnetic) field components are defined along the Delaunay (Voronoï) edges and over Voronoï (Delaunay) faces. Therefore, using Stokes' theorem, Faraday's and Ampère's laws are written as

$$\oint_{\partial S^D} \mathbf{E} \cdot d\mathbf{l}^D = -i\mu_0\omega \iint_{S^D} \mathbf{H} \cdot d\mathbf{S}^D - i\mu_0\omega \iint_{S^D} \mathbf{M}_p \cdot d\mathbf{S}^D \tag{7.6}$$

$$\oint_{\partial S^V} \mathbf{H} \cdot d\mathbf{l}^V = \iint_{S^V} \sigma \mathbf{E} \cdot d\mathbf{S}^V + \iint_{S^V} \mathbf{J}_p \cdot d\mathbf{S}^V, \tag{7.7}$$

where the superscripts $D$ and $V$ signify "Delaunay" and "Voronoï", respectively. $S$ and $\partial S$ are the face and the contour surrounding that face, and $\mathbf{S}$ and $\mathbf{l}$ are unit vectors normal to $S$ and along $\partial S$, respectively.

The finite-volume discretization is based on replacing the quantities with their averages. Here, we replace the normal components of $\mathbf{E}$ and $\mathbf{H}$ over the faces and the tangential components of these fields along the edges by their averages, $E$ and $H$, such that the results of the integrations in equations 7.6 and 7.7 equal their respective terms in the following equations. By considering the $m$th ($j$th) Delaunay (Voronoï) edge and orthogonal to it the $m$th ($j$th) Voronoï (Delaunay) face, and with $W$ indicating the number of edges surrounding each face, equations 7.6 and 7.7 can be discretized as

$$\sum_{q=1}^{W_j^D} E_{j,q}\, l_{j,q}^D = -i\mu_0\omega H_j\, S_j^D - i\mu_0\omega \iint_{S_j^D} \mathbf{M}_{p_j} \cdot d\mathbf{S}_j^D \tag{7.8}$$

$$\sum_{k=1}^{W_m^V} H_{m,k}\, l_{m,k}^V = \sigma E_m\, S_m^V + \iint_{S_m^V} \mathbf{J}_{p_m} \cdot d\mathbf{S}_m^V \tag{7.9}$$

where $l$ is a term with size equal to the length of each edge and a positive or negative sign determined by the mutual orientation of the Delaunay and Voronoï edges $m$ and $j$. This mutual orientation is determined based on the right-hand rule (see Figure 7.2 for more details). For finding this orientation between each two Delaunay and Voronoï edges, first, a global arbitrary orientation is attributed to each edge. In this way, each edge can be seen as a vector with size equal to the length of the edge and direction equal to the attributed arbitrary orientation. The mutual orientation of each two Delaunay and Voronoï edges is given by the sign of the cross product of their corresponding vectors. As the tetrahedral grid is piecewise constant with

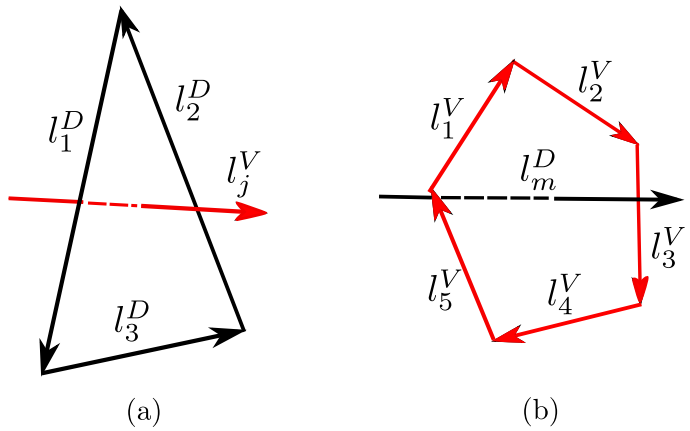


(a) (b)

Figure 7.2: The relation between the $j$th ($m$th) Voronoï (Delaunay) edge and its corresponding Delaunay (Voronoï) face is shown in panel a (in panel b). The mutual orientation of the Delaunay and Voronoï edges is determined based on their global orientations which are shown here by arrows. In panel (a) these mutual orientations all have a positive sign while they are negative in panel (b).

respect to conductivity, in the relations above $\sigma$ is the average of the conductivities of the tetrahedra that share the $m$th Delaunay edge. This average is defined here as an area-weighted average of the conductivities for the $m$th Voronoï face (see Figure 7.3 for more details). The integral form of the source terms is kept for the easier treatment of the Dirac delta functions in the next step.

For deriving a discretized formula for the Helmholtz equation equations 7.8 and 7.9 need to be combined. For doing this, the mutual orthogonality between the Delaunay (Voronoï) edges and Voronoï (Delaunay) faces can be used and an approximation made by assuming that the average electric (magnetic) field that is attributed to the $m$th ($j$th) Delaunay (Voronoï) edge equals the average value of the normal component of electric (magnetic) field that is attributed to the $m$th ($j$th) Voronoï (Delaunay) face. An equivalent of this approximation is also made in the discretizations on nonuniform rectilinear grids as mentioned by the early work of Madden and Mackie (1989). This approximation adds some error to the discretization because it is known that there are

always Voronoï edges present in the mesh that do not pass through their respective Delaunay faces (because not all the circumcentres are located inside their respective tetrahedra). One of the measures to control this discretization error is the general quality of the grid which is discussed in Section 6.3 and which is studied in Section 7.5.4. With the above approximation, the discretized form of the Helmholtz equation (relation 7.3) is derived by finding an expression for $H$ from relation 7.8 and substituting in 7.9:

$$\sum_{k=1}^{W_m^V} \left( \left( \sum_{q=1}^{W_{m,k}^D} E_{m,k,q}\, l_{m,k,q}^D \right) \frac{l_{m,k}^V}{S_{m,k}^D} \right) + i\omega\mu_0\sigma E_m\, S_m^V$$

$$= -i\omega\mu_0 \sum_{k=1}^{W_m^V} \frac{M_{p_{m,k}}}{S_{m,k}^D} - i\omega\mu_0 J_{p_m}. \tag{7.10}$$

Note that the terms with index $j$ from relation 7.8 possess index $(m, k)$ in the equation above. Also, for deriving the source terms the definitions of the sources given in relation 7.5 are used. In these terms, $M_p$ and $J_p$ are defined at the same locations as the magnetic and electric fields, i.e., along the Voronoï and tetrahedral edges, respectively. The magnitude and direction of magnetic and electric sources are determined by the magnitude and sign of $M_p$ and $J_p$, respectively.

## 7.4 Solution of the problem

Relation 7.10 can be written for all of the $N$ tetrahedral edges (or Voronoï faces) of the grid and the system of equations is solved for the unknown electric fields $E$. In practice, the complex relation above can be transformed into two real valued equations

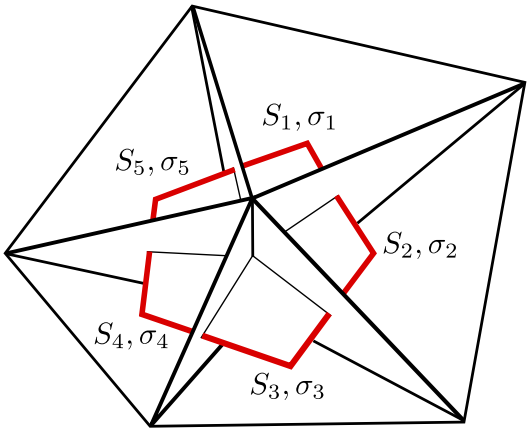


Figure 7.3: An example Voronoï face which is shared by five tetrahedra. $S_n$ and $\sigma_n$ ($n = 1, 2, 3, 4, 5$) are the portions of the face area located in the five tetrahedra and the conductivities of these tetrahedra, respectively. The conductivity that is attributed to the Voronoï face is the area-weighted average of the five conductivities.

by the decomposition of $E$ into real and imaginary parts:

$$E = E_{re} + iE_{im}$$

This results in a new system of equations that can be written as a block matrix equation

$$\begin{pmatrix} \mathbf{A}' & -\omega\mu_0\mathbf{B}' \\ \omega\mu_0\mathbf{B}' & \mathbf{A}' \end{pmatrix} \begin{pmatrix} \mathbf{E}_{re} \\ \mathbf{E}_{im} \end{pmatrix} = \begin{pmatrix} 0 \\ -\omega\mu_0\mathbf{S} \end{pmatrix}, \tag{7.11}$$

where $\mathbf{A}'$ and $\mathbf{B}'$ are $N \times N$ square matrices and $\mathbf{E}_{re}$, $\mathbf{E}_{im}$ and $\mathbf{S}$ are $N \times 1$ column matrices. The elements of matrix $\mathbf{A}'$ are functions of the sizes of the edges and areas of the faces and matrix $\mathbf{B}'$ is a diagonal matrix with diagonal elements equal to $\sigma S_m^V$. (An example for the coefficient matrix in the equation above is shown in Figure 7.4.) $\mathbf{E}_{re}$ and $\mathbf{E}_{im}$ are the real and imaginary parts of the unknown electric fields, and $\mathbf{S}$ is the right-hand side of equation 7.10 divided by $-i\omega\mu_0$. In this study, the MUMPS sparse direct solver (Amestoy et al., 2006) is used for solving this problem, and the

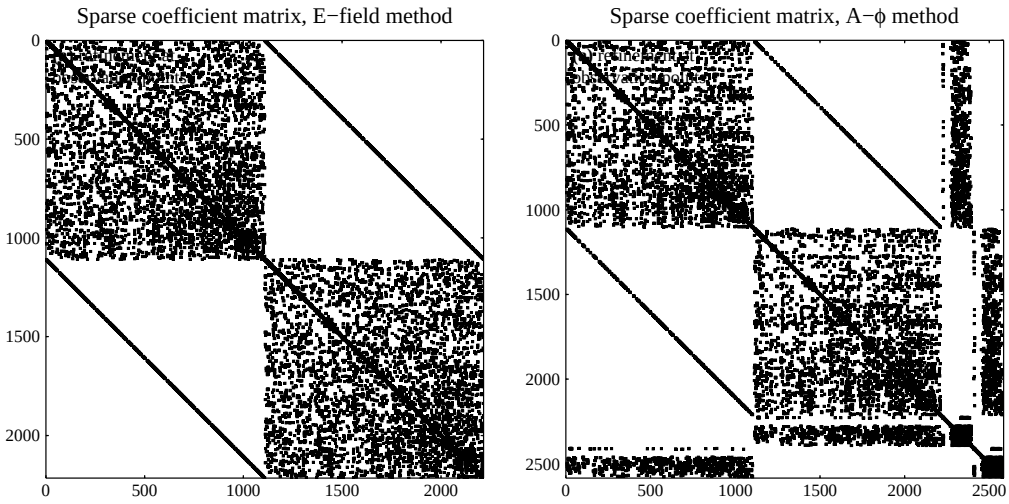


Figure 7.4: Examples of the coefficient matrices for the direct EM-field method (left) and for the EM potential method (right). These matrices correspond to a grid with $4,294$ tetrahedral cells, 798 tetrahedral nodes (vertices) and $5,266$ tetrahedral edges. The horizontal and vertical axes give the numbers for the rows and columns of the matrix, respectively, and the black dots show the locations of nonzero components.

approximate Dirichlet boundary condition is applied by assigning a zero value to the electric fields on the boundary of the domain. (MUMPS can also solve the complex system with a comparable amount of computation resources. The decomposition, however, allows for the use of a greater range of solvers.)

Direct solvers are generally more expensive than iterative solvers in terms of computation time and memory (Grayver and Streich, 2012). However, they also have advantages. Unlike iterative solvers, the convergence of direct solvers does not depend on the condition number of the coefficient matrix and the solutions to general problems are highly accurate (Operto et al., 2007). Also, direct solvers can show higher efficiency in the modelling and inversion of multi-transmitter problems (Oldenburg et al., 2013).

The solutions at the observation points can be found by interpolation using linear vector interpolation functions. At any point inside the grid with coordinates $(x, y, z)$

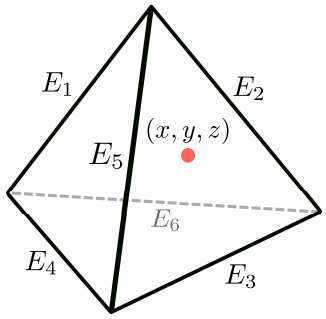


Figure 7.5: The electric and magnetic fields at any point inside a tetrahedron can be found by an interpolation among the primary electric field solutions at the six edges of the tetrahedron.

this interpolated solution is expressed as

$$\mathbf{E}^e(x, y, z) = \sum_{n=1}^{6} \mathbf{N}_n^e(x, y, z) E_n^e, \tag{7.12}$$

where the $\mathbf{N}_n^e$ terms are the linear vector interpolation functions of the edges of the tetrahedron $e$ in which the observation point is located, and $E_n^e$ are the solutions at these edges (see Figure 7.5). Relation 7.12 can also be used to find the magnetic field at an observation point by taking the curl of $\mathbf{E}$ and using Faraday's law. The vector interpolation functions are given by

$$\mathbf{N}_n^e = \left( L_{n_1}^e \nabla L_{n_2}^e - L_{n_2}^e \nabla L_{n_1}^e \right) l_n^e, \tag{7.13}$$

where $l_n^e$ is the length of the edge $n$, and $L_{n_1}^e$ and $L_{n_2}^e$ are the nodal interpolation functions of the endpoints of this edge (Jin, 2002). (Nodal interpolation functions are introduced in Section 3.2.) As an example, Figure 7.6 shows the linear vector interpolation functions of the three edges of a face of a regular tetrahedron over this face. These functions possess the magnitude of one at their respective edges and vanish towards the edge of the tetrahedron which does not share a node with their

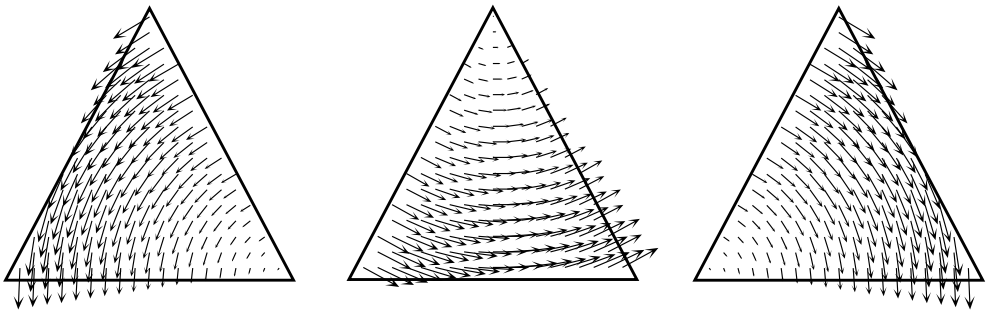


Figure 7.6: These three figures show, separately, the linear vector interpolation functions of the three edges of a face of a regular tetrahedron over this face. Figures (a), (b) and (c) correspond, respectively, to the edges on the left, in the middle and on the right hand side of this face. The sizes of the vectors show the magnitude of the interpolation functions with the largest ones showing the magnitude of one.

edge. Also, these vector functions are tangential to the middle of their respective edges and gradually become perpendicular to it at the endpoints of this edge. They are perpendicular to the other four edges of the tetrahedron which share a node with their respective edge.

## 7.5 Examples

### 7.5.1 Introduction

The accuracy of the finite-volume scheme is studied in this section using three examples. In the first two examples that follow, the magnetic and electric responses of an anomalous block-in-a-halfspace due to magnetic and electric sources are calculated. For both examples, the results from the finite-volume method are compared with results from the literature. For the second example, the effect of refinements at the observation points and at the source, and also the effect of grid quality on the accuracy of the solutions are also studied. The third example includes a realistic model with a complex geometry and topography. The solutions from this example

are compared with real HEM (helicopter-borne EM) data.

### 7.5.2 Example 1: magnetic dipole source

The first example represents a magnetic dipole source-receiver combination over a buried conductive cube. This scenario models airborne EM surveys where the transmitter-receiver pair moves in the air above the anomalous region. The large conductivity contrast that is considered here is typical of highly conductive metallic ore bodies contained in resistive shield rocks (see, e.g., Palacky and West, 1987). To verify the solutions, they are compared with the results of physical scale modelling (PSM) and the integral-equation (IE) method presented in Farquharson et al. (2006), and with finite-element solutions by Ansari and Farquharson (2014). Physical scale modelling is a laboratory study in which actual measurements are performed for idealized miniature geological models. The equivalence between laboratory measurements and real-life geological dimensions is achieved by appropriate scaling of the spatial dimensions, conductivities and frequency (for details of the physical scale modelling method see Frischknecht et al., 1987). For the numerical modelling in this example, the actual parameters that had been used in the physical scale modelling are used. The measurements had been conducted for a small graphite cube immersed in brine (Figure 7.7). The cube had side lengths of 14 cm with its top 2 cm below the brine surface. The transmitter and receiver were small horizontal loops of wire with a fixed separation of 20 cm. This pair moved along in the $x$-direction at a height of 2 cm above the brine surface. Graphite and brine had conductivities of $63,000$ and 7.3 S/m, respectively, and measurements had been conducted for frequencies 1, 10, 100, 200 and 400 kHz.

Figure 7.7 shows the tetrahedral and Voronoï grids used for solving the problem in this first example. 26 infinitesimal vertical unit magnetic dipoles are located inside the grid on the $xz$ plane from $x = -25$ to 25 cm and at the height of 2 cm. These dipoles

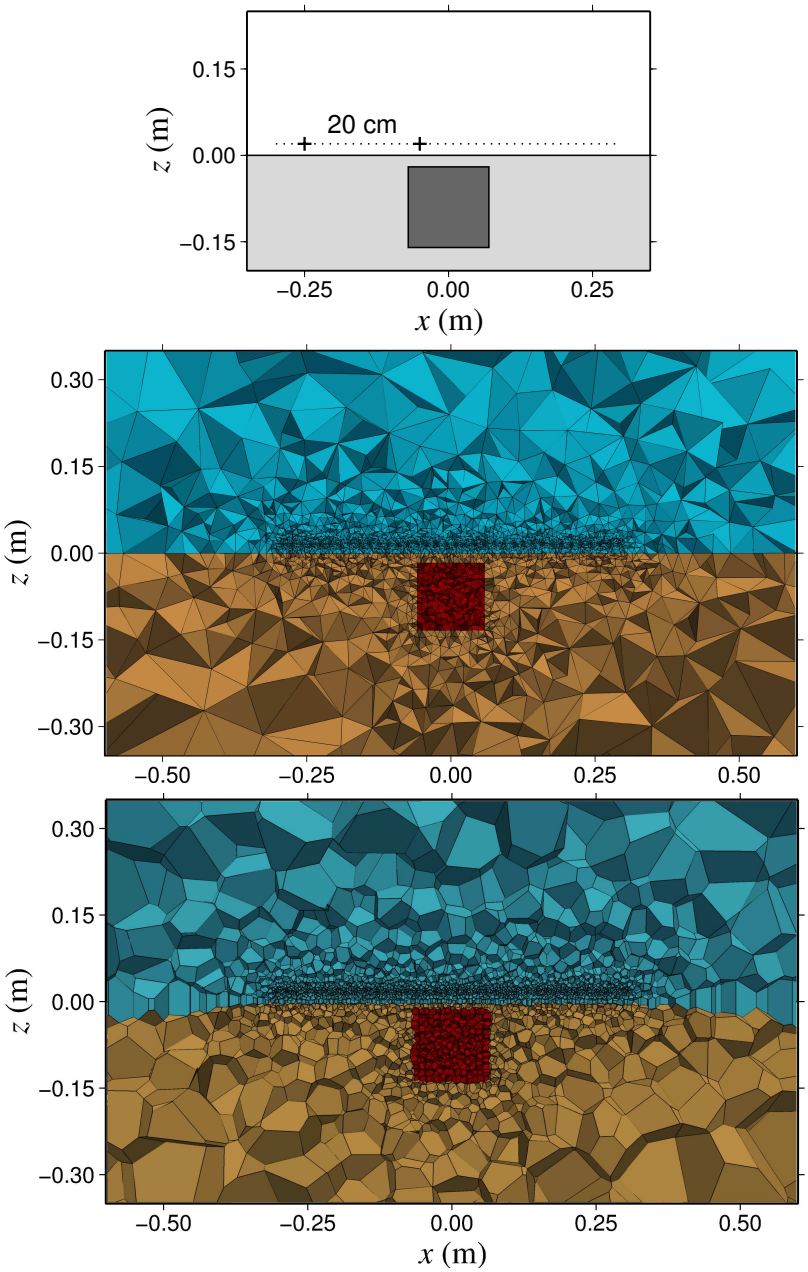


Figure 7.7: Top panel shows a vertical section through the model used in the first example which is a graphite cube (dark gray) immersed in brine. The source and the receiver which are 20 cm apart move parallel to the $x$ axis at the height of 2 cm above the brine surface. Middle and bottom panels show the tetrahedral and Voronoï grids, respectively, that are used for solving the problem. Grids are highly refined at the sources and the observation points and moderately refined at the graphite location.

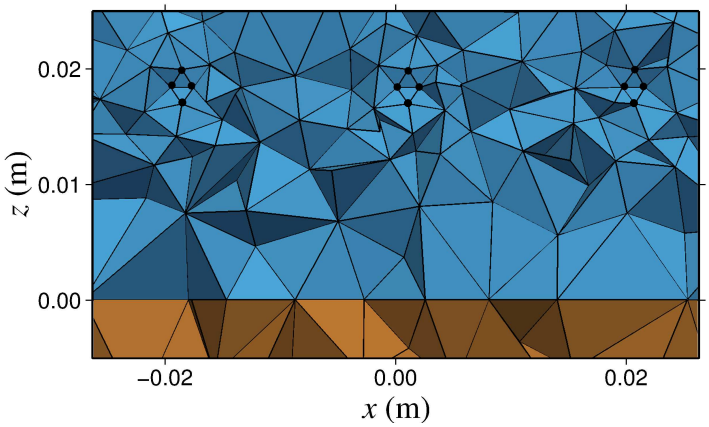


Figure 7.8: A close up to the location of some of the tetrahedra inserted inside the grid in order to position the infinitesimal vertical magnetic dipoles inside the tetrahedral grid for the first example. For each source, five nodes are inserted such that they form two regular tetrahedra with a common horizontal facet. The point magnetic dipole is located at the centroid of this common facet and it is directed along the Voronoï edge that connects the centroids of the two regular tetrahedra. The nodes are shown here as black dots.

were positioned by inserting tetrahedra with the edge size of 2 mm for each magnetic dipole (see Figure 7.8). No additional tetrahedra were inserted for the receivers as these receivers fell inside the tetrahedra that were inserted for the dipole sources. The observations are the secondary magnetic fields which are defined here as the total field minus the free-space (homogeneous wholespace) field normalized by the free-space field. The observations are attributed to the midpoint of the source-receiver pairs. Besides the refinements at the sources, a moderate refinement was imposed at the cube location by setting the maximum volume for the tetrahedra inside the cube as $10^{-7}$ $\mathrm{m}^3$. No particular refinement was considered at the earth-air interface. The entire numerical domain chosen for solving the problem had dimensions of $40 \times 40 \times 40$ km. A maximum tetrahedra radius-edge ratio of 1.12 was used for generating the tetrahedral grid which resulted in $425,239$ tetrahedra and $67,978$ Voronoï cells. The number of tetrahedral edges (which also equals the number of complex-valued unknowns) was

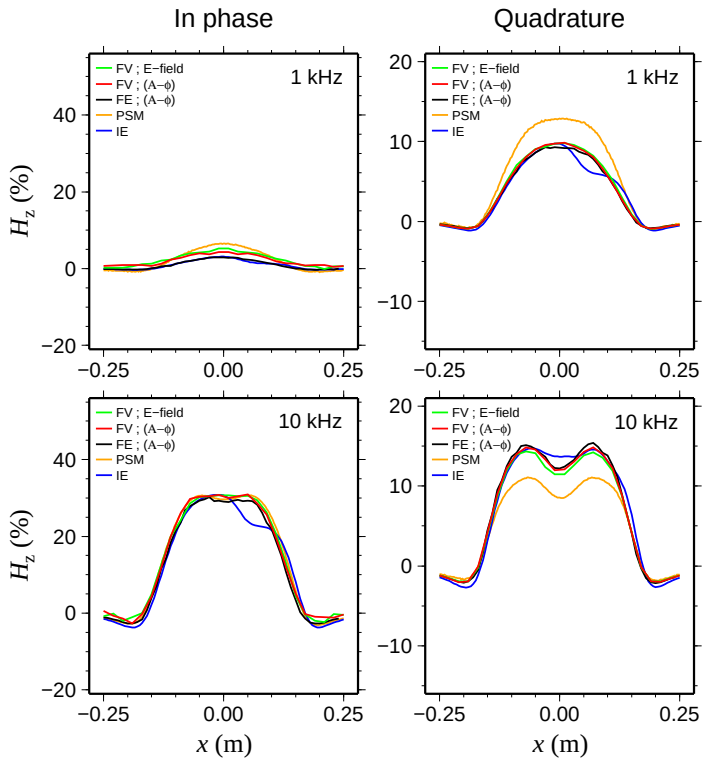


Figure 7.9: The in-phase and quadrature parts of the vertical component of the secondary magnetic field for frequencies 1 and 10 kHz used in the first example. The finite-volume solutions (direct EM-field method green lines and EM potential method red lines) are compared with physical scale modelling measurements (orange lines), integral-equation (blue lines) and finite-element solutions (black lines).

493, 678. The numerical domain did not really need to be this large (40 km) for satisfying the boundary condition. But, in unstructured grids, increasing the grid size does not increase the number of cells dramatically. For instance, in this example using dimensions of $40 \times 40 \times 40$ m instead of $40 \times 40 \times 40$ km only reduces the number of tetrahedral cells from 425, 239 to 316, 095. The results are, of course, very similar for both domain sizes.

Figures 7.9 and 7.10 show the in-phase and quadrature parts of the vertical component of magnetic field solutions for the five frequencies mentioned above compared with the physical scale modelling measurements and with the integral-equation and

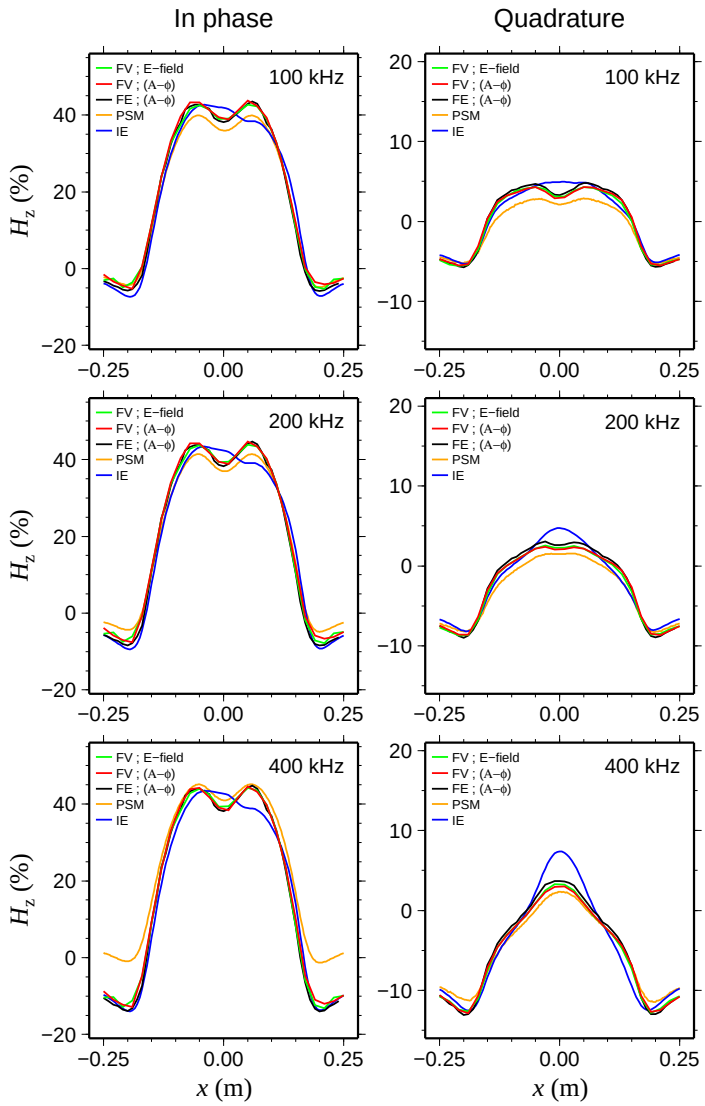


Figure 7.10: The in-phase and quadrature parts of the vertical component of the secondary magnetic field for frequencies 100, 200 and 400 kHz used in the first example. The finite-volume solutions (direct EM-field method green lines and EM potential method red lines) are compared with physical scale modelling measurements (orange lines), integral-equation (blue lines) and finite-element solutions (black lines).

finite-element solutions. Considering the fact that the laboratory measurements are subject to noise and measurement errors, there is a good agreement between the numerical results and the measurements. The discrepancy that can be seen between the physical scale modelling and the numerical results for the in-phase values at 400 kHz

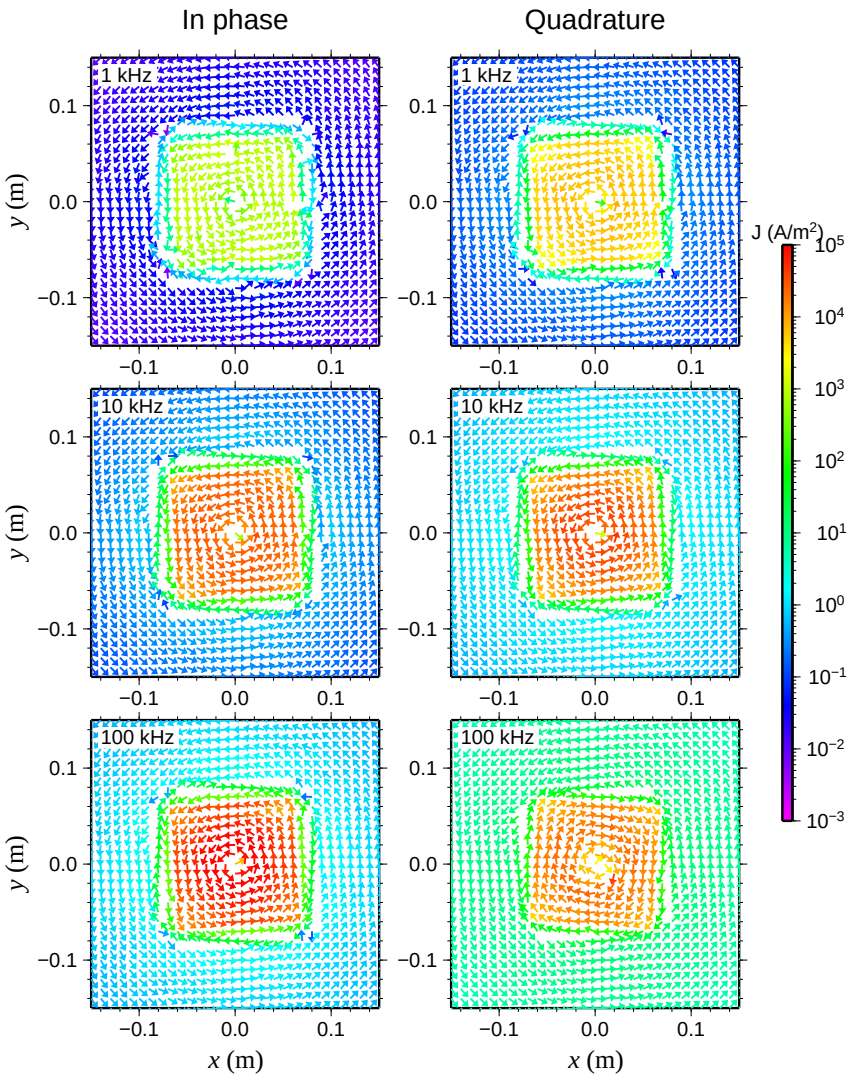


Figure 7.11: Total current density for frequencies 1, 10 and 100 kHz (from top to bottom) at a horizontal section passing through the graphite cube at the depth of 25 mm. For these sections, a single vertical magnetic dipole is located right at the top-centre of the cube at the height of 2 cm above the brine surface.

is thought to be from a capacitive effect in the physical scale modelling apparatus (see Farquharson et al., 2006, for more details). The finite-volume solutions agree well with those from the other numerical methods, i.e., finite-element and integral-equation results. We see that the finite-volume scheme has been able to solve the problem in spite of the large conductivity contrast that exists. Solutions have also

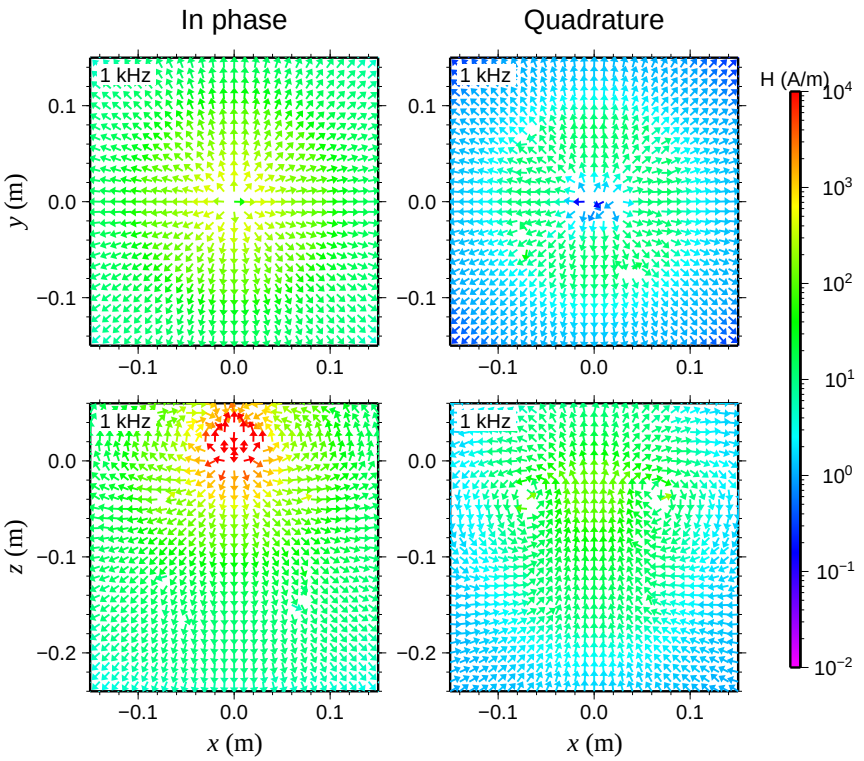


Figure 7.12: Total magnetic field at a horizontal section passing through the graphite cube at the depth of 25 mm, and at a vertical section passing through the cube at the *xz* plane for the frequency of 1 kHz.

been plotted as the vector representation of the fields on vertical and horizontal sections. For these sections, the grid was refined at all the observation points by inserting tetrahedra. Figure 7.11 shows the vector representation of the total current density for three frequencies (1, 10 and 100 kHz) at a horizontal section passing through the cube at the depth of 25 mm. For these sections, a single magnetic dipole is located right at the top-centre of the cube at the height of 2 cm above the brine surface. There is an obvious relation between the amplitudes of the vectors in this figure and the corresponding magnetic fields in Figures 7.9 and 7.10: the color scale shows the increasing dominance of the in-phase part over the quadrature part with increasing frequency. For the same frequencies and source location, Figures 7.12, 7.13 and 7.14, show the vector representation of the total magnetic field at the horizontal section

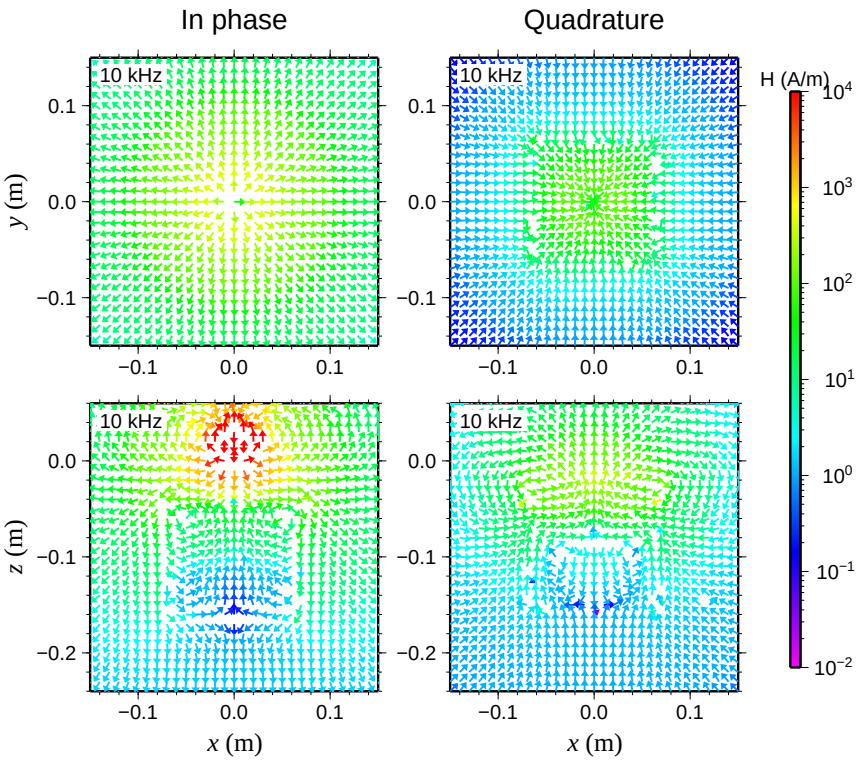


Figure 7.13: Total magnetic field at a horizontal section passing through the graphite cube at the depth of 25 mm, and at a vertical section passing through the cube at the $xz$ plane for the frequency of 10 kHz.

described above and at a vertical section passing through the cube at the $xz$ plane.

### 7.5.3 Example 2: grounded wire source

The second example represents a different geophysical survey scenario where the EM source is a long grounded wire operating at a low frequency and the anomalous region is located far from the source. This is depicted in Figure 7.15. In this model, a conductive block with dimensions $120 \times 200 \times 400$ m in the $x$-, $y$- and $z$-directions, respectively, is buried in a halfspace such that the centre of the top of the block is at $(1000, 0, -100)$ m. The EM source was a 100 m straight grounded wire with ends located at the air-earth interface at $(0, 0, 0)$ m and $(100, 0, 0)$ m (see Figure 7.16),

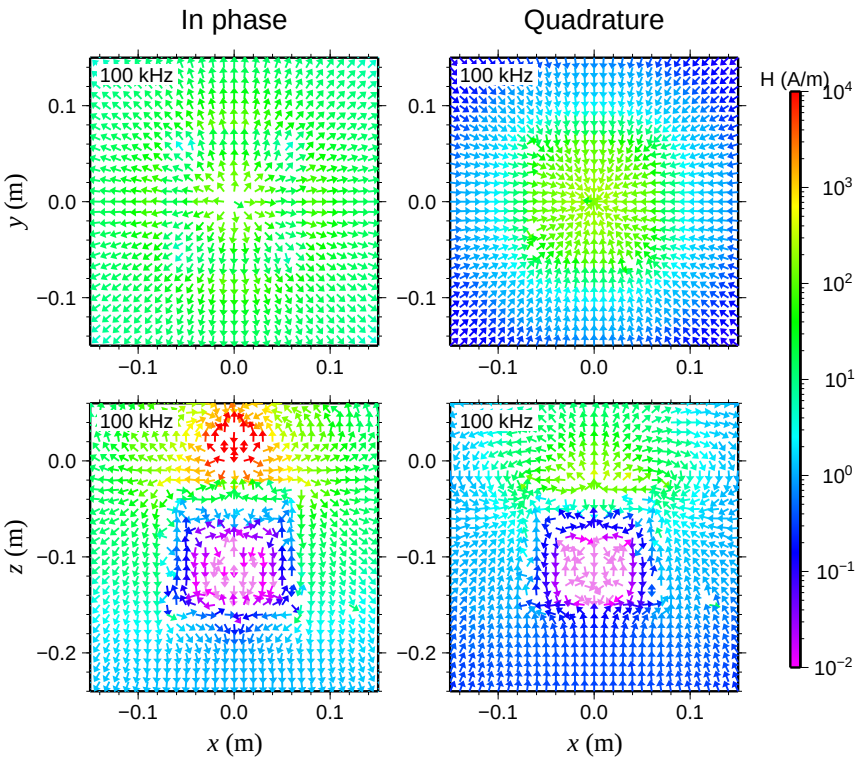


Figure 7.14: Total magnetic field at a horizontal section passing through the graphite cube at the depth of 25 mm, and at a vertical section passing through the cube at the $xz$ plane for the frequency of 100 kHz.

and the observation profile was along the $x$-axis from $(500, 0, 0)$ m to $(1500, 0, 0)$ m at the interface. The block and the halfspace had conductivities of 0.2 and 0.02 S/m, respectively. A frequency of 3 Hz and a unit current value were used. The entire computational domain had dimensions of $40 \times 40 \times 40$ km which was comprised of $162,689$ and $26,129$ tetrahedral and Voronoï cells, respectively, and $189,105$ Delaunay edges. Figure 7.15 also shows the tetrahedral and Voronoï grids used for this example. The observation points were spaced 10 m apart along the observation profile and for each observation point a tetrahedron with the edge size of 5 m was inserted inside the grid. The conductive block was refined, moderately, by setting the maximum volume of the tetrahedra inside this block equal to 5000 $\text{m}^3$. Also, the line source location was refined by dividing the wire into 20 smaller segments (each segment is a tetrahedral

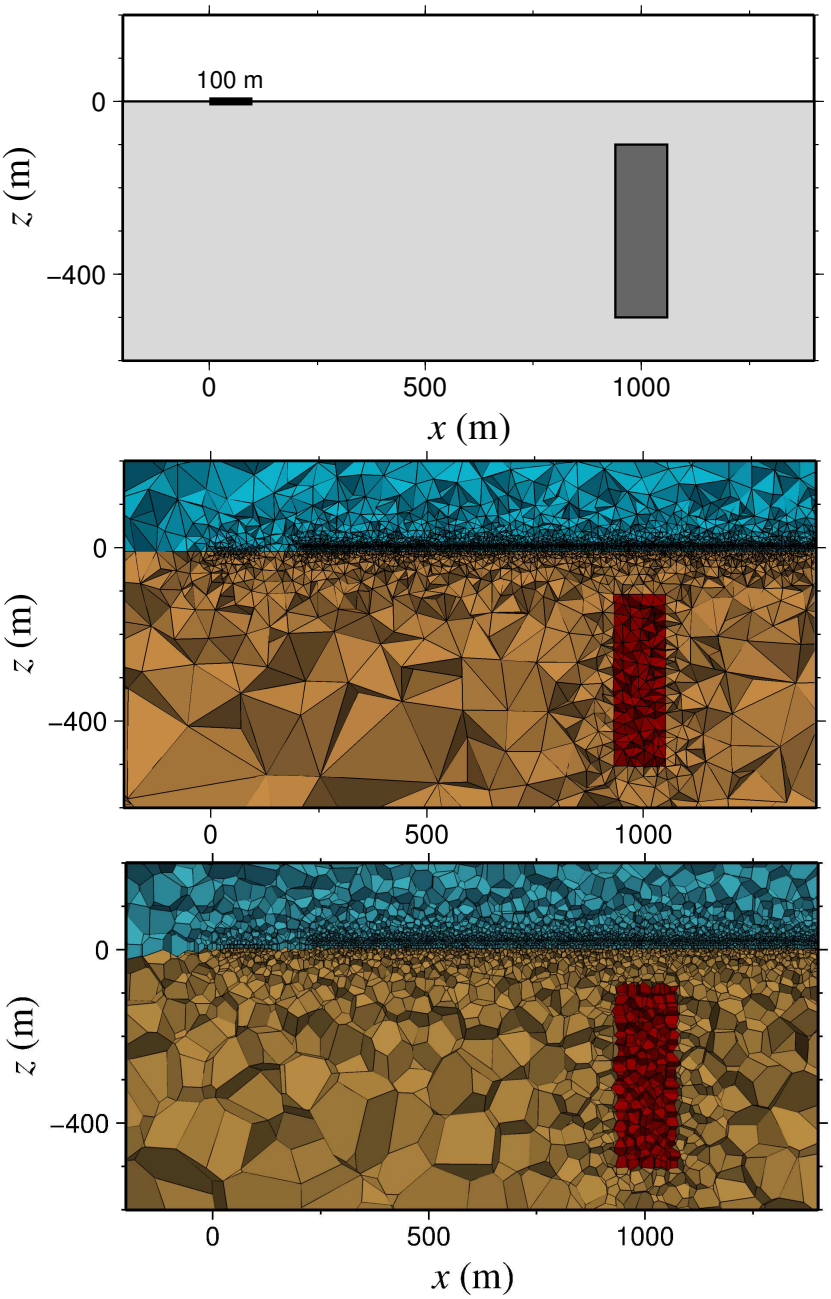


Figure 7.15: Top panel shows a vertical section through the model used in the second example. It shows the location of the 100 m line source (the thick black segment) and the anomalous region (dark gray). Middle and bottom panels show the tetrahedral and Voronoï grids, respectively, that are used for solving the problem. Grids are refined at the source and at the observation points and moderately refined at the anomalous region.

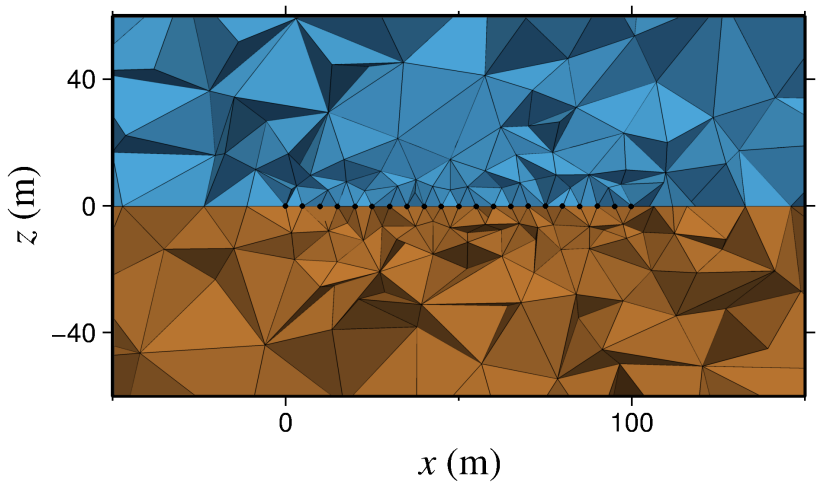


Figure 7.16: A close up to the location of the grounded wire source in the tetrahedral grid for the second example. The source has been placed inside the grid by inserting 21 nodes at the air-earth interface. The nodes are shown here as black dots.

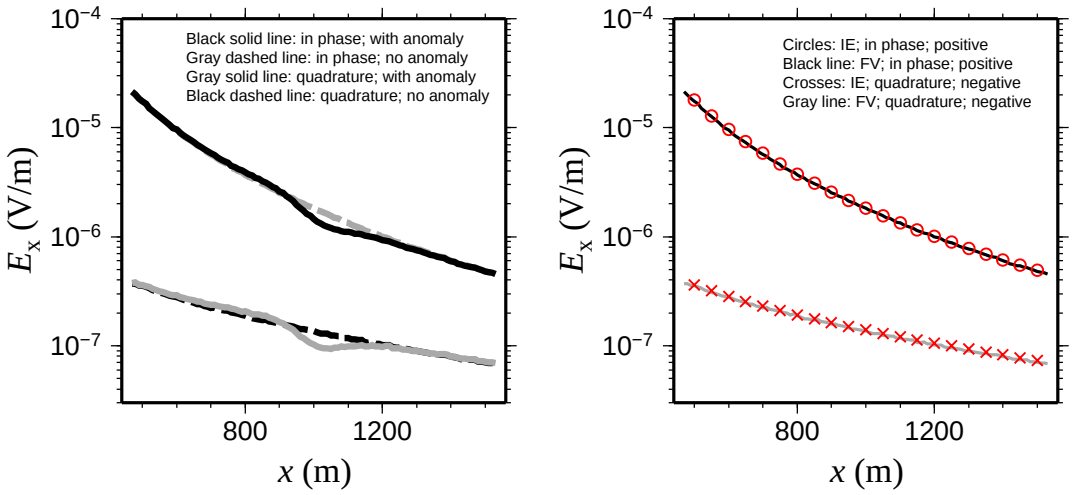


Figure 7.17: The in-phase and quadrature parts of the $x$-component of the total electric field at the observation points for the second example when the anomalous region is present (left panel) and for the homogeneous halfspace (right panel). The solutions are compared with the solutions from an integral-equation code (Farquharson and Oldenburg, 2002).

edge). The total computation time and memory usage for solving this problem using the MUMPS direct solver were 40 s and 4 Gbytes, respectively (on an Apple Mac Pro computer; 2.26 GHz Quad-Core Intel Xeon processor).

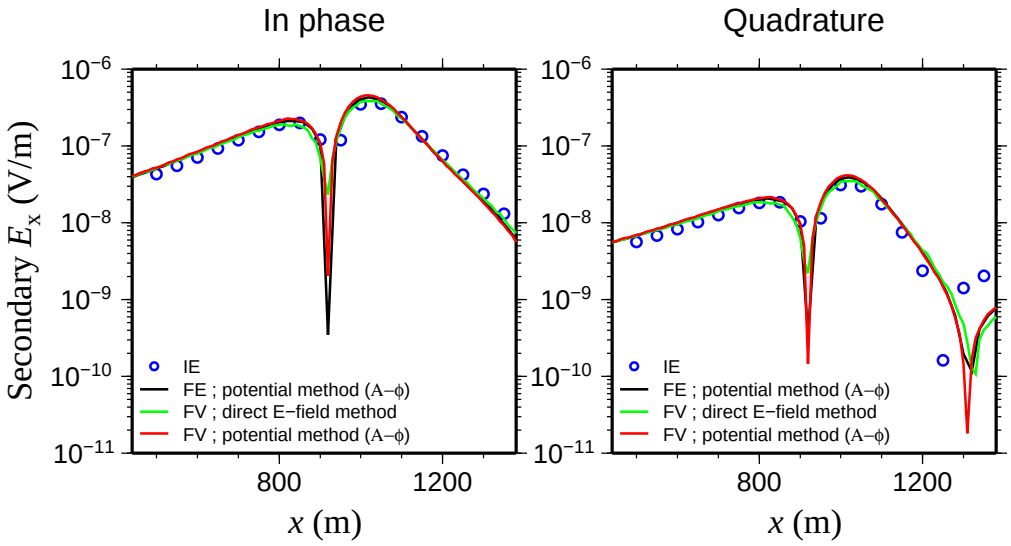


Figure 7.18: The in-phase and quadrature parts of the scattered electric field solutions for the second example. Solutions for the direct EM-field method and for the potential method are shown by green and red lines, respectively. Finite-element solutions and integral-equation solutions are depicted by black lines and blue circles, respectively. The finite-element solutions belong to a code that uses a potential approach (Ansari and Farquharson, 2014).

Figure 7.17 shows the in-phase and quadrature parts of the $x$-component of the total electric field at the observation points when the anomalous region is present and for the homogeneous halfspace. The solutions are compared with the solutions from an integral-equation code (Farquharson and Oldenburg, 2002). There is a good match between the two numerical solutions. Figure 7.18 shows the in-phase and quadrature parts of the scattered electric field along the profile which show good agreements with the integral-equation solutions. The discrepancy that is seen at the far ends of the profile is interpreted as errors in the integral-equation solutions. This is most likely due to the large sizes of the blocks that were used for discretizing the anomalous region in this method. For this example, the scattered field is defined as the total field with anomalous region minus the total field for the homogeneous halfspace. The vector representation of the solution is used to observe the pattern of the total electric field at

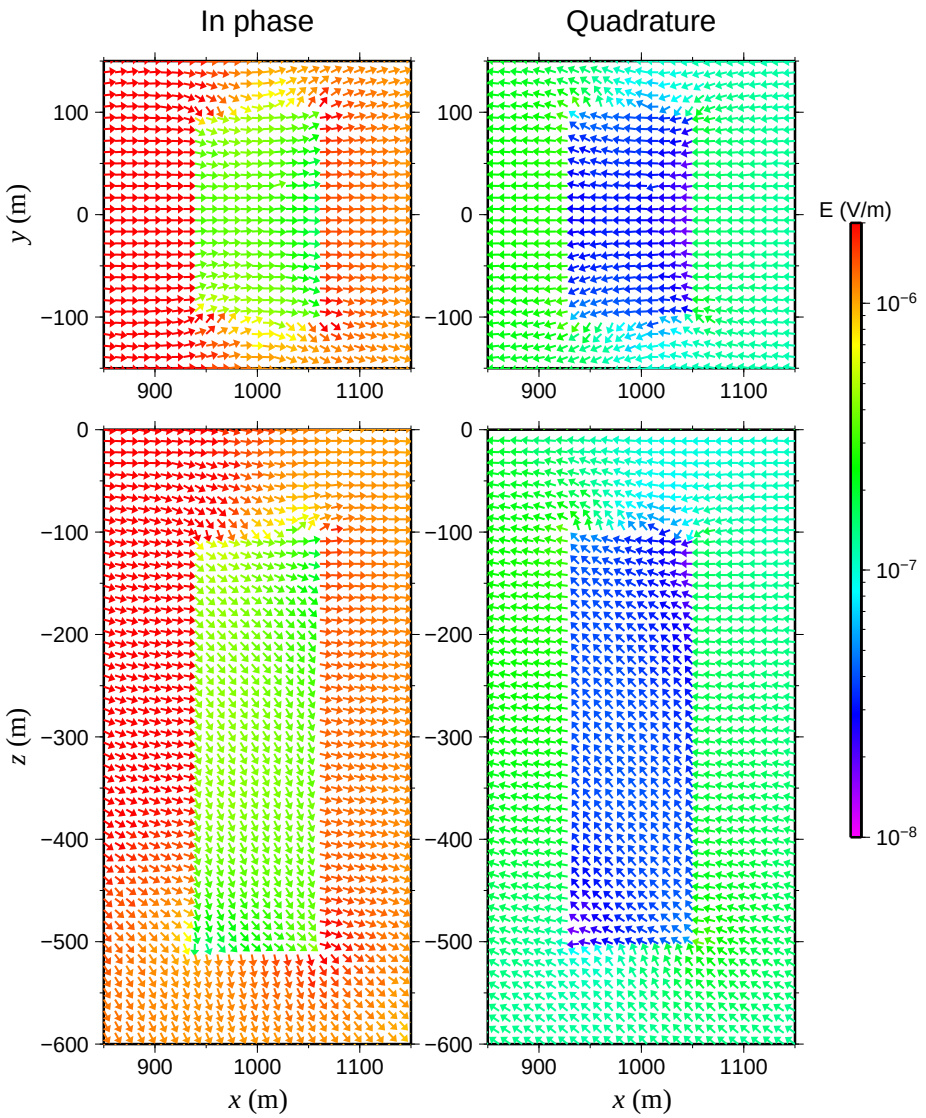


Figure 7.19: The total electric field for the second example at a horizontal section at the depth of 200 m (top panels) and at a vertical section (bottom panels) passing through the anomalous region.

sections through the anomalous region. Figure 7.19 shows these horizontal and vertical sections. Figure 7.20 verifies the continuity (discontinuity) of the normal (tangential) component of current density (electric field) and the tangential (normal) component of electric field (current density), respectively. In this figure, the observations are the $x$-component of the electric field and the current density along profiles that pass

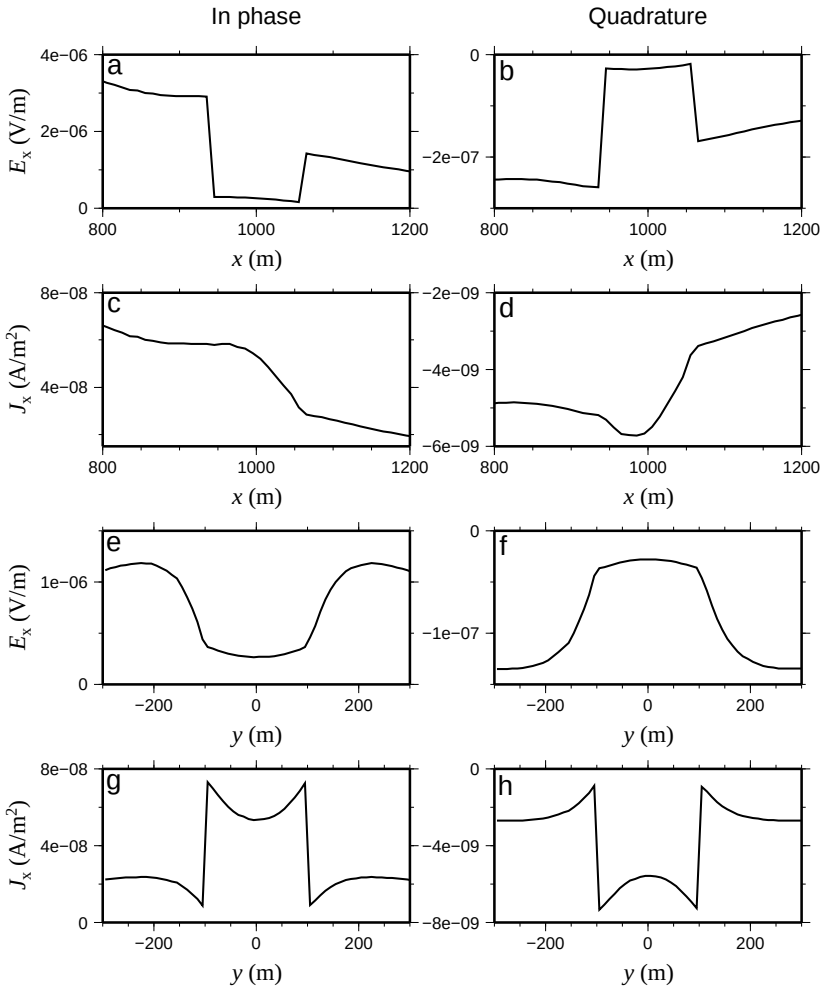


Figure 7.20: Panels (a) and (b) show the $x$-component of the electric field, and (c) and (d) show the $x$-component of the current density along the profile $y = 0$ m, $z = -200$ m, and $x = 800$ to 1200 m for the second example. Panels (e) and (f) show the $x$-component of the electric field, and (g) and (h) show the $x$-component of the current density along the profile $x = 1000$ m, $z = -200$ m, and $y = -300$ to 300 m.

through the anomalous region. One of the profiles extends from $(800, 0, -200)$ m to $(1200, 0, -200)$ m, parallel to the $x$-axis, and the other one is from $(1000, -300, -200)$ m to $(1000, 300, -200)$ m, parallel to the $y$-axis.

### 7.5.4 Accuracy and resource usage

For the second example, experiments have been conducted to better understand the effects of grid quality and grid refinements on the accuracy and efficiency of the finite-volume scheme. Three criteria are examined: (1) the effect of refinement at the observation points; (2) refinement at the line source, and (3) the effect of grid quality improvement (maximum tetrahedra radius-edge ratio). The effect of refinement at the anomalous region was also studied but this kind of refinement did not result in any meaningful improvement in accuracy for this example (even for a higher conductivity contrast of $10^6$). Therefore, the results for this refinement are not presented here. To obtain the error estimate due to refinement at the observation points it was needed to insert tetrahedra as large as 50 m at each observation point. For this reason, only 21 observation points were used which were spaced 50 m apart along the observation profile. For all the experiments, the same conductivities and frequency as described in the previous section were used. In the absence of analytic solutions the solution due to a very fine grid was chosen as the reference solution needed to calculate the errors. In this fine grid, the line source was divided into 20 segments, the tetrahedra inserted at each observation location had the edge size of 0.5 m and the maximum tetrahedra radius-edge ratio was 1.12. Figure 7.21 shows, for the three criteria mentioned above, cumulative errors versus the changing parameters. Here, cumulative error is the square root of the sum of the squares of the errors. Also, the changing parameter in Figure 7.21 (b) ("Source segments size") is the size of each of the segments that form the line source. For the first and second criteria, the radius-edge ratio that was used was always 1.12. For the second and third criteria, the cell size at the observation points was always 0.5 m, and for the first and third criteria the source segments size was 5 m. Figure 7.22 shows the corresponding total electric fields and errors for each experiment and corresponding detailed information is given in Tables 7.1, 7.2 and

7.3. In order to examine the effect of interpolation on accuracy at the observation points, Figure 7.21 (a) gives two sets of cumulative errors for the two cases when there is no interpolation at the observation points and when there is interpolation. Two sets of very similar grids were used for these two cases. In the grids that were used for the case when there is no interpolation, the tetrahedra that were inserted for the observation points were slightly shifted such that the observation points coincide with those edges of the tetrahedra that were aligned with the $x$ axis. For the other set of grids, the observation points were located inside the tetrahedra. In plots (b) and (c), no interpolation is involved.

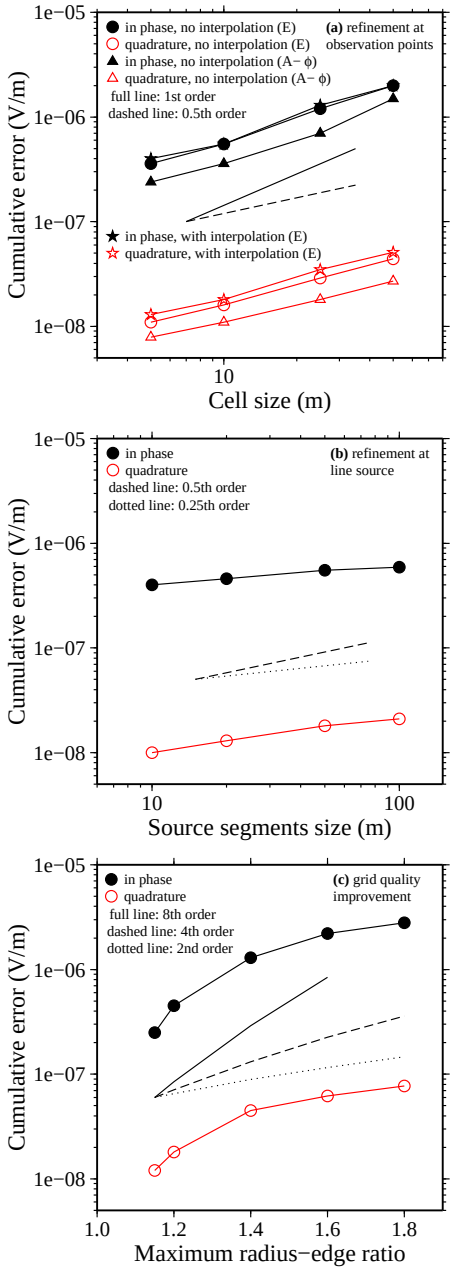


Figure 7.21: The results of accuracy studies for the second example which show cumulative errors versus the changing parameters. These parameter are the cell size at the observation points (a), the size of the segments that form the line source (b), and the radius-edge ratio used for generating the tetrahedral grid (c). Different trends are shown by the dotted, dashed and full lines inside each plot. These lines enable the comparison of the orders of accuracy for the various data-sets. The results in panels (b) and (c) belong to the direct EM-field method, without interpolation at the observation points, and the results in panel (a) correspond to the direct method, with and without interpolation, and to the potential method, without interpolation.

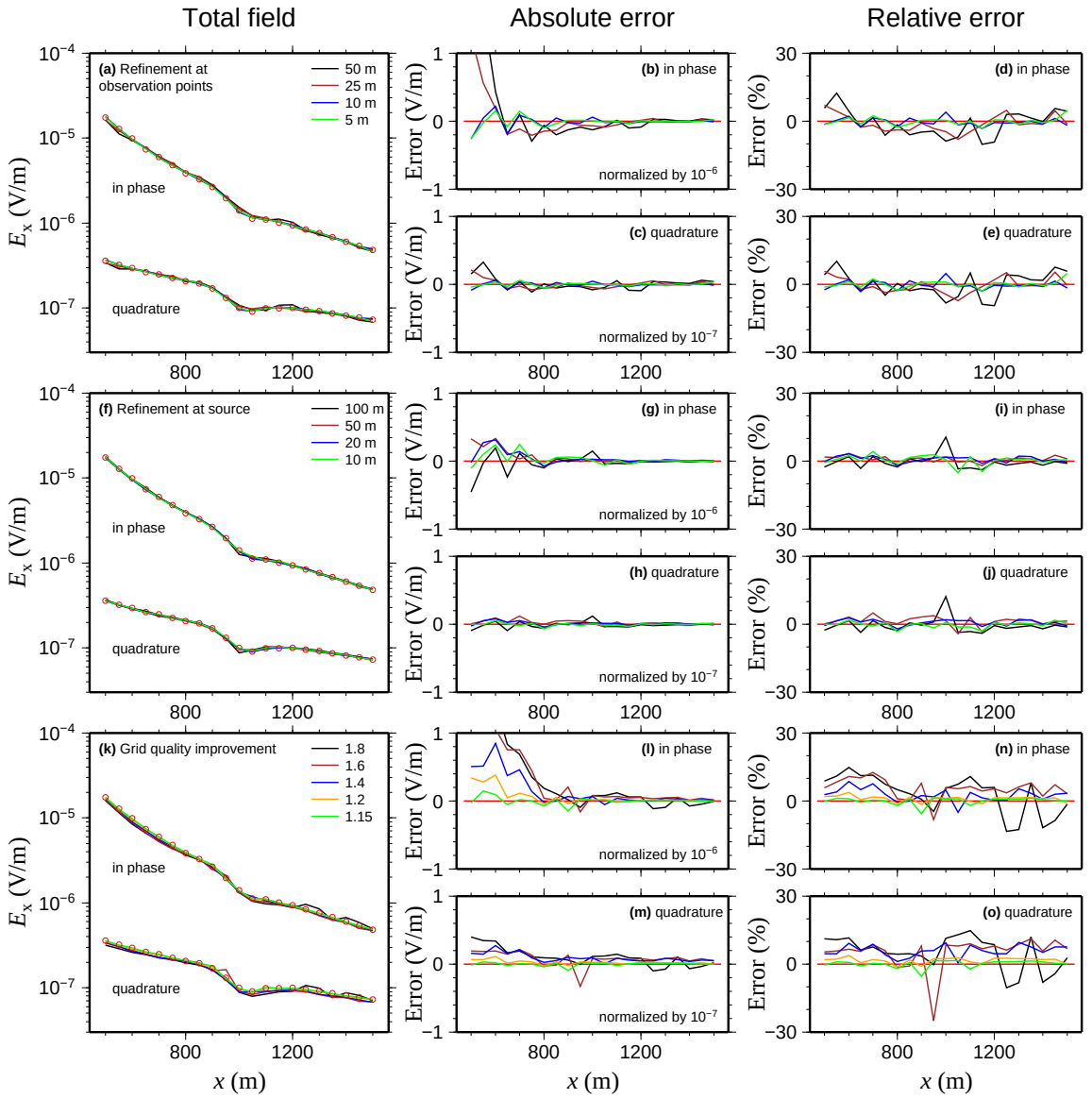


Figure 7.22: Total electric field (left panels) and the corresponding errors (middle and right panels) for the accuracy studies conducted for the second example. The red circles show the reference solutions which are solutions for a very fine grid. Panels (b), (c), (d) and (e) are the errors for the total fields in panel (a); panels (g), (h), (i) and (j) correspond to panel (f); panels (l), (m), (n) and (o) correspond to (k). In the middle panels (absolute errors) the in-phase and quadrature parts are normalized by $10^{-6}$ and $10^{-7}$, respectively. In the right panels, the relative error is the ratio of the absolute error to the true value expressed as percent.

Table 7.1: This table corresponds to Figure 7.21 (a). For the four cell sizes, it gives the number of tetrahedral (tet.) and Voronoï (Vor.) cells and edges, and the computation resources required for solving the problems. For these problems, the source segments size was 5 m and the radius-edge ratio of the grids was 1.12.

| Cell size (m) | No. of tet. cells | No. of Vor. cells | No. of tet. edges | Computation time (s) | Memory (Gbytes) | Error (V/m) in-phase | Error (V/m) quadrature |
|---|---|---|---|---|---|---|---|
| 50.0 | 109,135 | 17,750 | 127,479 | 32 | 3.0 | $2.0E$-6 | $4.4E$-8 |
| 25.0 | 163,709 | 26,549 | 191,032 | 59 | 5.0 | $1.2E$-6 | $2.9E$-8 |
| 10.0 | 200,611 | 32,408 | 233,664 | 82 | 6.7 | $5.5E$-7 | $1.6E$-8 |
| 5.0 | 192,084 | 30,992 | 223,667 | 77 | 6.3 | $3.6E$-7 | $1.1E$-8 |



Table 7.2: This table corresponds to Figure 7.21 (b). For the four segment sizes, it gives the number of tetrahedral (tet.) and Voronoï (Vor.) cells and edges, and the computation resources required for solving the problems. For these problems, the cell size at the observation points was 0.5 m and the radius-edge ratio of the grids was 1.12.

| Segments size (m) | No. of tet. cells | No. of Vor. cells | No. of tet. edges | Computation time (s) | Memory (Gbytes) | Error (V/m) in-phase | Error (V/m) quadrature |
|---|---|---|---|---|---|---|---|
| 100.0 | 497,336 | 79,861 | 577,869 | 254 | 18.1 | $5.9E$-7 | $2.1E$-8 |
| 50.0 | 581,095 | 93,245 | 674,994 | 539 | 22.3 | $5.5E$-7 | $1.8E$-8 |
| 20.0 | 605,131 | 97,077 | 702,903 | 604 | 23.2 | $4.6E$-7 | $1.3E$-8 |
| 10.0 | 546,701 | 87,722 | 635,042 | 276 | 20.3 | $4.0E$-7 | $1.0E$-8 |

Table 7.3: This table corresponds to Figure 7.21 (c). For the five radius-edge ratios, it gives the number of tetrahedral (tet.) and Voronoï (Vor.) cells and edges and the computation resources required for solving the problems. For these problems, the cell size at the observation points was 0.5 m and the source segments size was 5 m.

| Radius-Edge ratio | No. of tet. cells | No. of Vor. cells | No. of tet. edges | Computation time (s) | Memory (Gbytes) | Error (V/m) in-phase | Error (V/m) quadrature |
|---|---|---|---|---|---|---|---|
| 1.8 | 26,961 | 4,504 | 31,541 | 3 | 0.3 | 2.8$E$-6 | 7.7$E$-8 |
| 1.6 | 36,441 | 6,018 | 42,552 | 5 | 0.4 | 2.2$E$-6 | 6.2$E$-8 |
| 1.4 | 59,383 | 9,694 | 69,227 | 9 | 0.8 | 1.3$E$-6 | 4.5$E$-8 |
| 1.2 | 168,474 | 27,128 | 195,875 | 41 | 3.8 | 4.5$E$-7 | 1.8$E$-8 |
| 1.15 | 303,125 | 48,660 | 352,201 | 105 | 8.9 | 2.5$E$-7 | 1.2$E$-8 |

Careful examination of the accuracy graphs in Figure 7.21 reveals the relative importance of the three criteria mentioned above. It is very important to know how much refinement is necessary and at what locations, and also what radius-edge ratio should be chosen. Having too much refinement and very low radius-edge ratios might not only increase the problem size beyond the memory limit, but it might also adversely affect the accuracy of the solutions by increasing the non-uniformity of the grid. Figure 7.21 (a) and the corresponding graphs in Figure 7.22 show that refinement at the observation locations is absolutely necessary. The solutions are found inside the tetrahedra by interpolation and, therefore, the closer the location of the direct solutions at the tetrahedral edges to the observation point the more accurate the interpolation results will be. The cumulative errors for the two cases with and without interpolation show similar orders of accuracies (between orders 0.5 and 1). However, the results for the case without interpolation shows lower errors. This error difference can be attributed to the interpolation at the observation points. However, this difference is small which shows the effectiveness of the linear interpolation that is used. In contrast, the accuracy results in Figure 7.21 (b) show that grid refinement at the source is not as critical. This graph shows that there is little improvement in accuracy from segment size 100 to 10 m. Finally, Figure 7.21 (c) shows the utmost importance of the grid quality (in fact, the order of accuracy increases with decreasing radius-edge ratio). However, Table 7.3 suggests that grid quality also has the main effect on the number of the cells and, hence, the size of the problem.

### 7.5.5 Example 3: the Ovoid

The third example presented here is for a realistic model with complex geometry and topography (Figure 7.23). This model is of the Ovoid massive sulfide ore body located at Voisey's Bay, Labrador, Canada (the same model was used for the forward

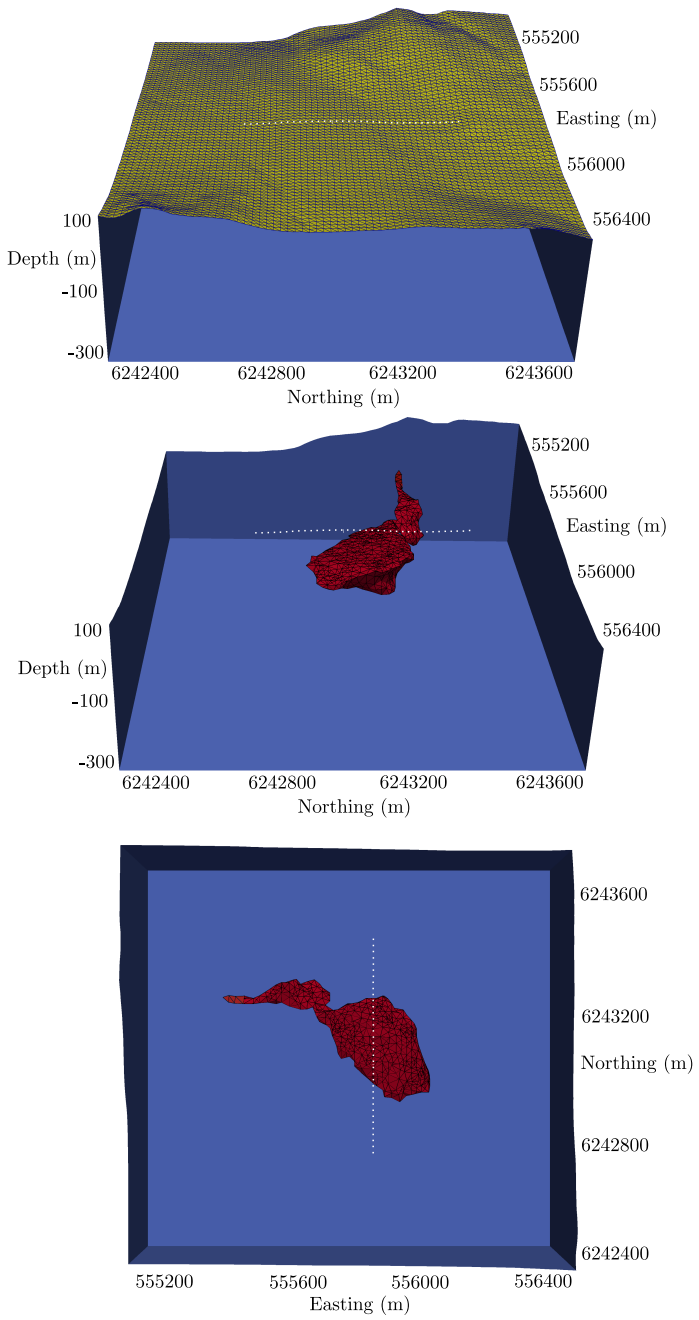


Figure 7.23: The model used in the third example. Top figure shows the topography of the region and the middle and bottom figures show the sulphide body by removing the topography. The white dots show the observation locations. In UTM coordinates, the points have Easting of 555837 m and their Northing is from 6242800 to 6243500 m.

modelling of gravity data in Section 5.4). The ore body is flat-lying, composed of 70% massive sulphide, and is located under approximately 20 m of overburden (Balch, 2000). Only the conductive ore body is included in the model here. The data from an HEM survey of the region has been simulated and the results are compared with the real survey data (Garrie, 1995). In the HEM surveys, the transmitter and receiver coils are mounted inside a bird that is towed below the helicopter 30 m above ground. As for the first example, the coils are coplanar and horizontal. The transmitter-receiver separation was 8 m and the operating frequency was 900 Hz. 36 transmitter-receiver pairs were located along a North-South profile passing over the body and at 30 m above the topography. The conductivities of the body and of the background were chosen by trial-and-error in order to match the real data. These values were 100 and 0.001 S/m, respectively. (This trial-and-error is similar to an inversion for finding unknown conductivities. The accuracy of the presented scheme has been verified by the previous examples. The aim of this example was to show that the unstructured scheme can be effectively used for simulating real data when incorporated in an inversion.) The grid that was used was composed of $190,121$ tetrahedra, $31,462$ Voronoï cells, $223,650$ Delaunay edges, and the size of the inserted tetrahedra for the sources and receivers was 1 m. Figure 7.24 shows vertical sections passing through the tetrahedral and Voronoï grids along the observation profile. The in-phase and quadrature parts of the numerical and real data are shown in Figure 7.25. The data are values of the secondary magnetic field expressed in ppm.

## 7.6 Conclusions

Unstructured grids offer features that can help improve the solution of total field electromagnetic problems. These grids allow local refinements that are required at

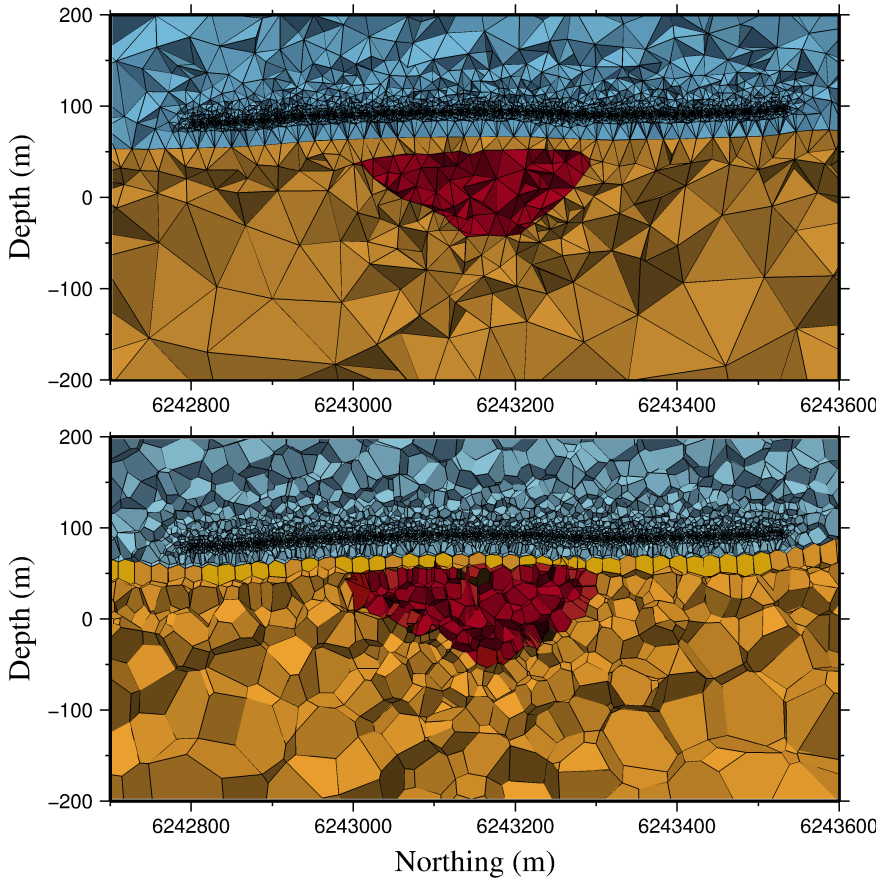


Figure 7.24: Top and bottom panels show the tetrahedral and Voronoï grids, respectively, that were used for solving the problem in the third example. Grids are refined at the transmitter and receiver pairs that are located 30 m above ground. The anomalous region (in red color) is a section of the Ovoid.

sources and at observations points. They also allow the efficient modelling of geological interfaces. The finite-volume method has been used to develop a staggered scheme which uses dual Delaunay-Voronoï grids. This scheme can be seen as an unstructured version of the well-known Yee's scheme. The Helmholtz equation is solved in the frequency domain to find the tangential component of the electric field along the Delaunay edges. Subsequently, edge vector interpolation functions are used for interpolation inside the tetrahedra.

Two examples have been presented to assess the applicability of the scheme

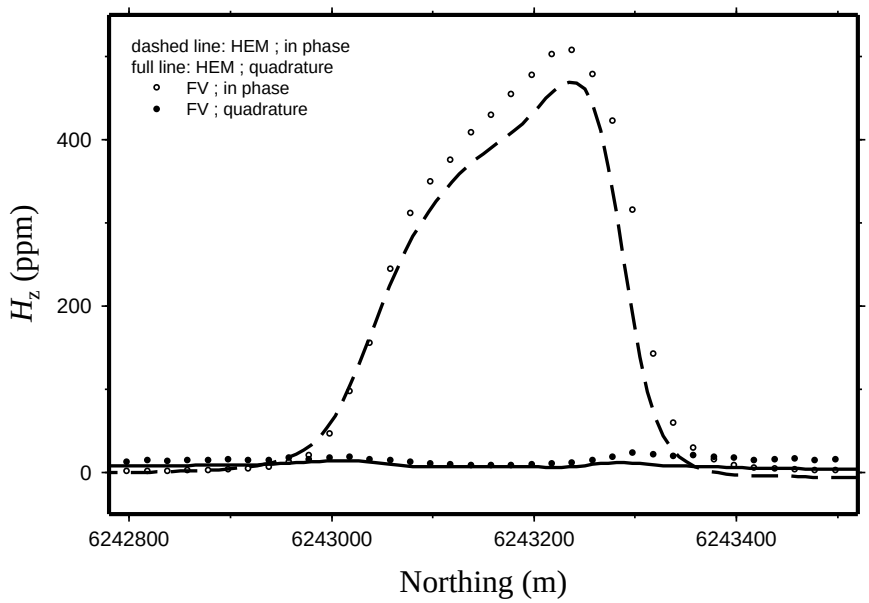


Figure 7.25: The numerical data from the third example (circles) compared with the real HEM data from the region (lines). The data are the $z$-component of the scattered magnetic field at the receivers attributed to the midpoint of transmitter-receiver pairs, and expressed as ppm.

for modelling two different scenarios: one for magnetic dipole source-receiver pairs with high frequencies and a large conductivity contrast, and the other one for a long grounded line source with a low frequency and a small contrast. The scheme is verified by the comparison of the solutions with the numerical results from integral-equation and finite-element methods, and with the physical scale modelling measurements. Also, accuracy studies have been conducted for the model in the second example. The results of this study show the relatively higher importance of refinement at the observation points and also the importance of the general quality of the grid compared to the refinement at the source. Refinement of the grid at the boundary between regions of different conductivities is of relatively lower importance compared to the other criteria. An example with a realistic model is also included to demonstrate the ability of the presented unstructured scheme in modelling EM data due to complex

geometry and in the presence of topographical features. The good agreement between the numerical results and the reference solutions in the given examples suggest the suitability of the presented modelling approach as a forward modelling engine within inversion procedures.

For the solution of the linear system of equations produced by the presented finite-volume approach the sparse direct solver MUMPS was used. Although iterative solvers are considerably less expensive than direct solvers in terms of computation time and especially memory, their performance is highly dependent on the conditioning of a problem. The finite-volume scheme investigated in this chapter was based on the direct discretization of the EM-field formulation of Maxwell's equations. This discretization leads to near-singular systems (Haber et al., 2000) and conventional iterative solvers have serious difficulties solving these systems. Also, the high degree of non-uniformity of the cells arising from the unstructured nature of the grids further deteriorates the conditioning of the problem. The examples presented here could not be solved easily using standard iterative solvers. Therefore, a direct solver was chosen, which did indeed prove capable of solving the systems. It is, nevertheless, expected that the techniques that have been used for the enhancement of finite-volume and finite-element schemes on rectilinear grids, such as the divergence correction (see, e.g., Smith, 1996; Streich et al., 2010; Farquharson and Miensopust, 2011) or using the alternative potential formulation of Maxwell's equations (Haber et al., 2000), will lead to improved conditioning and stability of the problem, and hence efficiency of the solution by iterative solvers on unstructured grids. This latter case is considered in Chapter 9.

# Chapter 8

# Finite-volume modelling of MT data using the direct EM-field formulation

## 8.1 Introduction

The magnetotelluric method is an EM technique which uses naturally occurring signals for revealing the underground conductivity structure of the earth. As in this method there is no control over the sources, the measured fields cannot be interpreted directly. The ratio between the measured fields, however, such as the MT impedance tensor and the magnetic transfer functions, contain information about the subsurface conductivity distribution (Tikhonov, 1950; Cagniard, 1953). These new quantities are used, themselves, to calculate new parameters such as the apparent resistivity and the impedance phase which bear physical meanings and can be interpreted. In practice, the orthogonal components of the electric and magnetic fields are measured on the surface of the earth. The measurements are performed for certain frequencies and

the interpreted parameters are attributed to the skin depths corresponding to those frequencies. Although some primary results can be deduced from the MT parameters, a full interpretation of the data requires sophisticated inversion procedures.

The common numerical methods have been used for the simulation of MT data. These include the integral-equation method (e.g., Ting and Hohmann, 1981; Wannamaker et al., 1984; Wannamaker, 1991), the finite-difference method (e.g., Smith and Booker, 1991; Newman and Alumbaugh, 2000; Siripunvaraporn et al., 2002), the finite-volume method (e.g., Madden and Mackie, 1989; Mackie et al., 1993; Haber et al., 2000), and the finite-element method (e.g., Mogi, 1996; Mitsuhata and Uchida, 2004; Farquharson and Miensopust, 2011). For implementing unstructured grids, however, only the finite-element has been used (e.g., Key and Weiss, 2006; Liu et al., 2008; Franke-Börner, 2013) and, as for the CSEM case, the finite-volume method has not received attention.

This chapter deals with the finite-volume modelling of MT data using the unstructured staggered grids described and used in the previous chapter. As for the CSEM problems a direct sparse solver (MUMPS) is used and, therefore, the problem of slow convergence at low frequencies and spurious modes that arise with iterative solutions of the 3-D MT problems are avoided. In the following sections, first, the source of the MT signals is described. Then, the governing equations and the boundary condition of the MT problem are presented. Afterwards, the MT responses are introduced and, finally, two benchmark examples are presented for which the results are compared with those from the literature.

## 8.2 The source of MT signals

Natural electromagnetic signals of reference to geophysics come from various processes and from sources ranging from the core of the earth to the sun. Within the frequency range of interest in the magnetotelluric method (which is typically 0.001-$10^4$ Hz) only two source regions are important. These are the atmosphere and the magnetosphere. Electrical storms in the lower atmosphere are the dominant cause of the fields between 1 Hz and 10 kHz, whereas below 1 Hz the fields originate primarily in hydromagnetic waves in the magnetosphere. In both cases, the EM fields at the surface of the earth behave like plane waves, with most of their energy reflected but with a small amount propagating vertically downward into the earth (Vozoff, 1991).

## 8.3 The MT problem

Since in the MT problem the source is taken to be a plane wave which is normally incident upon the earth, there is no source inside the numerical domain and, therefore, source-free Maxwell's equations govern the problem

$$\nabla \times \mathbf{E} = -i\omega\mu_0\mathbf{H} \tag{8.1}$$

$$\nabla \times \mathbf{H} = \sigma\,\mathbf{E}, \tag{8.2}$$

where the quantities are the same as those in equations 7.1 and 7.2. Maxwell's equations can be combined in order to eliminate the magnetic field, $\mathbf{H}$, and obtain the Helmholtz equation for electric field

$$\nabla \times \nabla \times \mathbf{E} + i\omega\mu_0\sigma\mathbf{E} = 0, \tag{8.3}$$

which is, again, the same as the relation 7.3 except that there is no source term included. The result of the finite-volume discretization of this relation is exactly the same as that of relation 7.3 with, of course, the discretized source terms excluded. The source which is a plane wave is introduced to the numerical domain through the boundary conditions.

## 8.4 Boundary conditions

In principle, the boundary condition for a general three-dimensional MT problem is 2-D. However, if the boundaries of the numerical domain are far enough away from the inhomogeneities of the model, an inhomogeneous Dirichlet boundary condition can be approximated by a boundary condition based on a 1-D model (homogeneous or layered halfspace) for simplicity. For the two examples presented in this chapter, the analytical expressions given by Weaver (1994) for a homogeneous halfspace are used for computing this boundary condition. For an MT source with polarization along the $x$ axis (a plane sheet of current), the following expressions give the $x$-component of the electric field at the height/depth of $z$

$$E_x = 2\,i\,\omega\,\mu_0 f\,(z)\,, \tag{8.4}$$

where

$$f\,(z) = \frac{1}{\alpha\sqrt{i}} \begin{cases} 1 - z\alpha\sqrt{i} & 0 < z < h \\ e^{-z\alpha\sqrt{i}} & z < 0 \end{cases} \tag{8.5}$$

In these relations, $h$ is the thickness of the air layer, $\omega$ is the angular frequency, $i$ is the imaginary unit and $\mu_0$ is the permeability of the free space. Also, $\alpha = \sqrt{\omega\mu_0\,\sigma}$ where $\sigma$ is the conductivity of the homogeneous halfspace. Here, the air-earth interface is at $z = 0$ and it can be seen that there are two separate expressions for the air and the

earth region. The same relations can be used for other source polarization directions. In the next section, it is explained that we also need a $y$-directed source polarization for calculating the elements of the impedance tensor.

In practice, using the relations above, $E_x$ ($E_y$) is found for the height of the midpoint of the desired boundary edge and then the projection of this field along the orientation of the edge is calculated. Therefore, $E_x$ ($E_y$) is a constant value for the edges located on the top and at the bottom of the domain, it is decreasing on the two vertical sides that are parallel to the $x$- ($y$-) axis, and it is zero on the two vertical sides that are perpendicular to the $x$- ($y$-) axis. ($E_z$ is zero for all edges.) The projection of these electric fields along the boundary edges are the only nonzero values on the right-hand-side of the matrix equation 7.11.

## 8.5 The MT responses

As mentioned in the introduction to this chapter, in the MT method it is impedance which yields information about the subsurface conductivity. This quantity gives the relation between the different components of the electric and magnetic fields at an observation station and, therefore, is a tensor. For the electric and magnetic fields observed along the $x$ and $y$ directions, this relation can be written as

$$\begin{pmatrix} E_x \\ E_y \end{pmatrix} = \begin{pmatrix} Z_{xx} & Z_{xy} \\ Z_{yx} & Z_{yy} \end{pmatrix} \begin{pmatrix} H_x \\ H_y \end{pmatrix}, \tag{8.6}$$

where $E$, $H$ and $Z$ are the electric and magnetic fields and the impedances, respectively.

In a 1-D earth, no electric field is induced parallel to the inducing magnetic field.

Therefore

$$\frac{E_x}{H_x} = \frac{E_y}{H_y} = Z_{xx} = Z_{yy} = 0. \tag{8.7}$$

Also, as resistivity only varies with depth, i.e., in the $z$ direction, the expansion of Maxwell's equations shows that $Z_{xy} = -Z_{yx}$. In a 2-D case, if the measurements are conducted along the geological strike and perpendicular to it, the diagonal elements will be zero but the off-diagonal elements are independent of each other. In real field data, where the true strike is unknown, the diagonal elements are not zero, but they are equal with opposite signs:

$$Z_{xx} = -Z_{yy} \quad ; \quad Z_{xy} \neq Z_{yx} \tag{8.8}$$

In a general 3-D earth, all the elements of the impedance tensor are independent:

$$Z_{xx} \neq Z_{yy} \quad ; \quad Z_{xy} \neq Z_{yx} \tag{8.9}$$

For finding the four independent impedance elements in the numerical modelling four equations are needed. Therefore, it is common to consider two source polarizations along the $x$ and $y$ directions which results in the following matrix equation

$$\begin{pmatrix} E_{x1} & E_{x2} \\ E_{y1} & E_{y2} \end{pmatrix} = \begin{pmatrix} Z_{xx} & Z_{xy} \\ Z_{yx} & Z_{yy} \end{pmatrix} \begin{pmatrix} H_{x1} & H_{x2} \\ H_{y1} & H_{y2} \end{pmatrix}, \tag{8.10}$$

where the indices 1 and 2 correspond to the first and second polarizations. This

system of equations is readily solved for the unknown impedances as

$$\begin{aligned} Z_{xx} &= \left(E_{x1}H_{y2} - E_{x2}H_{y1}\right)/D \\ Z_{xy} &= \left(E_{x2}H_{x1} - E_{x1}H_{x2}\right)/D \\ Z_{yx} &= \left(E_{y1}H_{y2} - E_{y2}H_{y1}\right)/D \\ Z_{yy} &= \left(E_{y2}H_{x1} - E_{y1}H_{x2}\right)/D, \end{aligned} \tag{8.11}$$

where $D$ is the determinant of the matrix $\mathbf{H}$ (which contains the $H$ elements).

The most important parameters that are derived from the MT impedance are apparent resistivity and impedance phase. For each impedance element there is an apparent resistivity, $\rho_a$, and a phase, $\Phi$, calculated by

$$\rho_{a_{ij}} = \frac{1}{\omega\mu_0}\left(\Re\left(Z_{ij}\right)^2 + \Im\left(Z_{ij}\right)^2\right) \tag{8.12}$$

and

$$\Phi_{ij} = tan^{-1}\frac{\Im\left(Z_{ij}\right)}{\Re\left(Z_{ij}\right)}, \tag{8.13}$$

where $i, j = x, y$. The impedance phase shows the difference between the phases of $E$ and $H$. This value is 45 degrees everywhere in a homogeneous halfspace. Impedance phase and apparent resistivity are the two parameters that are computed for the models in the next section.

## 8.6 Examples

### 8.6.1 Introduction

For verifying the finite-volume scheme for the MT method, two examples have been used and the solutions are compared with those from the literature. The examples are

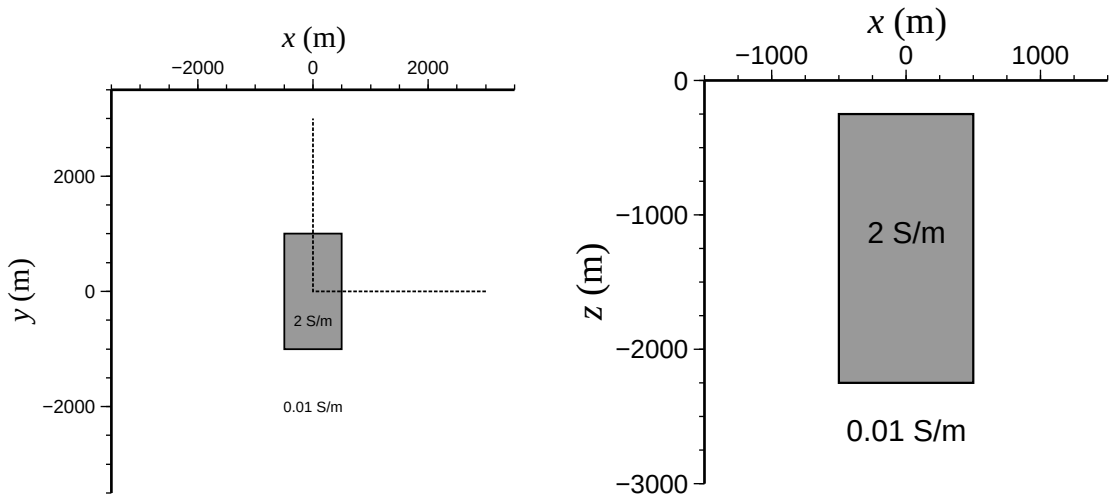


Figure 8.1: The left and right panels show, respectively, the plan and side views of the 3D-1A model used in the first example. The anomalous block is shown in gray and the observation profiles are shown as dashed-lines.

from the COMMEMI project reported in Zhdanov et al. (1997). There are two models called 3D-1A and 3D-2A. For the first example, the values of apparent resistivity have been compared with the results given in Zhdanov et al. (1997), and for the second example the results for apparent resistivity and phase are compared with the IE solutions given by Wannamaker (1991).

### 8.6.2 Example 1: 3D-1A model

Figure 8.1 shows the first model which comprises an anomalous block in a homogeneous halfspace. In this model, a conductive block with dimensions of $1 \times 2 \times 2$ km in the $x$-, $y$- and $z$-directions, respectively, is buried in a halfspace such that the centre of the top of the block is at $(0, 0, -250)$ m. There were two observation profiles at the earth-air interface along the $x$-axis from $(0, 0, 0)$ to $(3, 0, 0)$ km, and along the $y$-axis from $(0, 0, 0)$ to $(0, 3, 0)$ km. The block and the halfspace had conductivities of 2 and 0.01 S/m, respectively. The same frequencies as used in Zhdanov et al. (1997) were

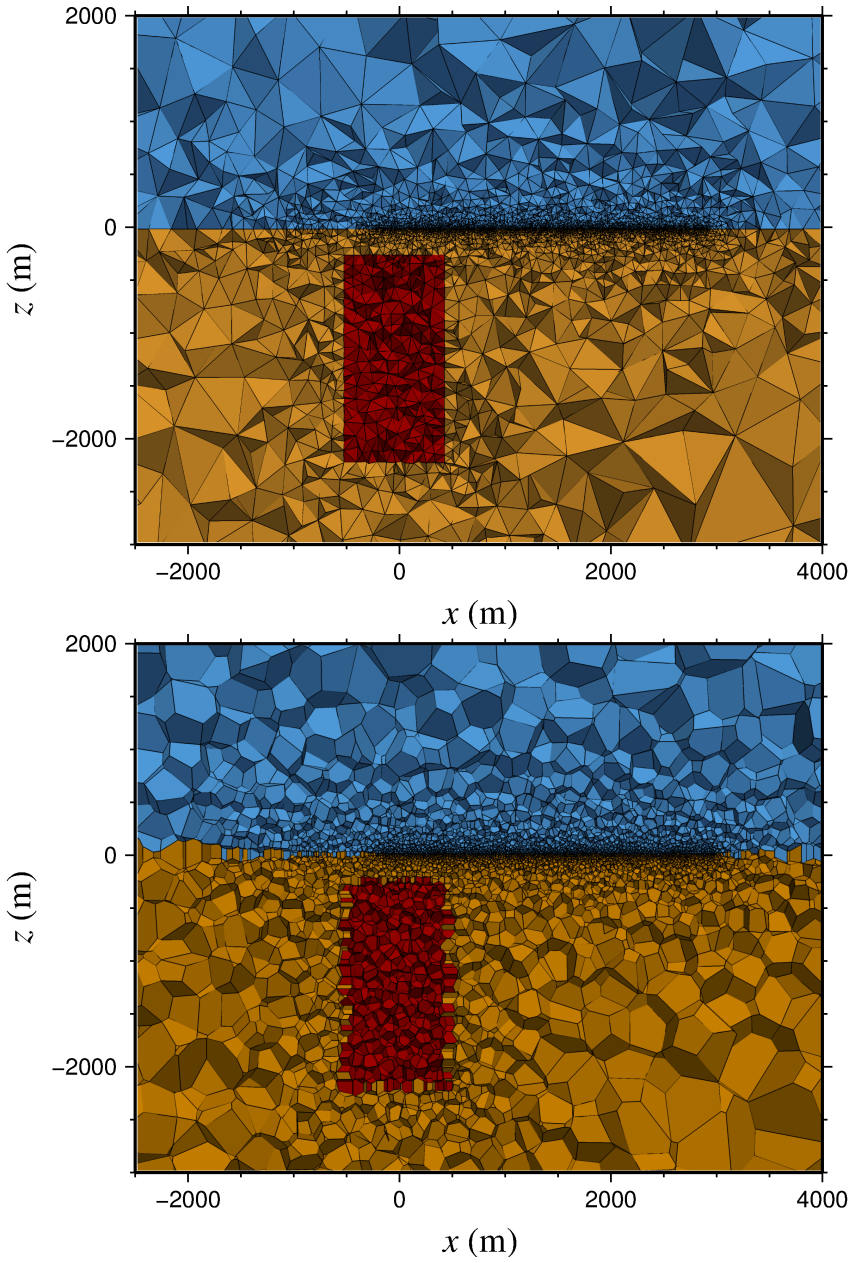


Figure 8.2: Top and bottom figures show, respectively, vertical sections at the $y = 0$ m plane through the tetrahedral and Voronoï grids used for solving the problem in the first MT example. Grids are highly refined at the observation points and moderately refined at the anomalous region (in red). The Voronoï faces that cross the interfaces are arbitrarily colored.

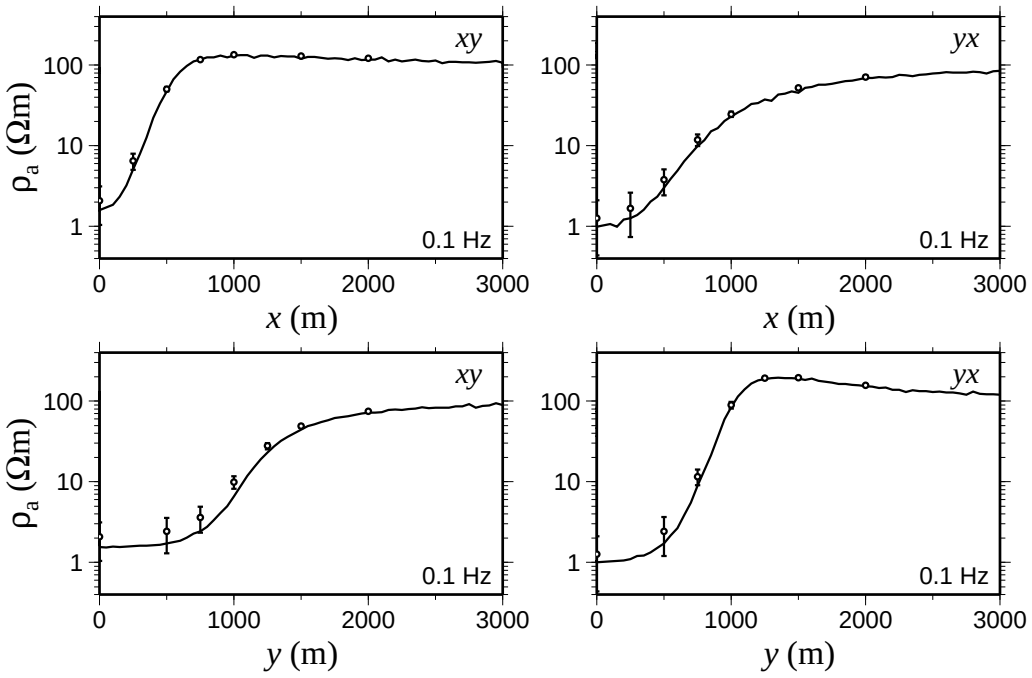


Figure 8.3: These figures show for the first MT example (the 3D-1A model) the apparent resistivities corresponding to the off-diagonal impedance tensor elements (i.e., the $xy$ and $yx$ elements). The results are for the frequency of 0.1 Hz. The top and bottom panels show the results for the profiles along the $x$ and $y$ axes, respectively. The finite-volume solutions are shown as lines and the results from Zhdanov et al. (1997) are shown as circles with error bars.

used: 0.1 and 10 Hz. The entire computational domain had dimensions of $40 \times 40 \times 40$ km which was comprised of $388,739$ and $62,648$ tetrahedral and Voronoï cells, respectively, and $452,497$ Delaunay edges. Vertical sections of the tetrahedral and Voronoï grids are shown in Figure 8.2. The observation points were spaced 50 m apart along the observation profiles and for each observation point a tetrahedron with the edge size of 10 m was inserted inside the grid. The conductive block was refined, moderately, by setting the maximum volume of the tetrahedra inside this block equal to $500,000$ m$^3$. The total computation time and memory usage for solving this problem using the MUMPS direct solver were 175 s and 13.7 Gbytes, respectively (on an Apple Mac Pro computer; 2.26 GHz Quad-Core Intel Xeon processor).

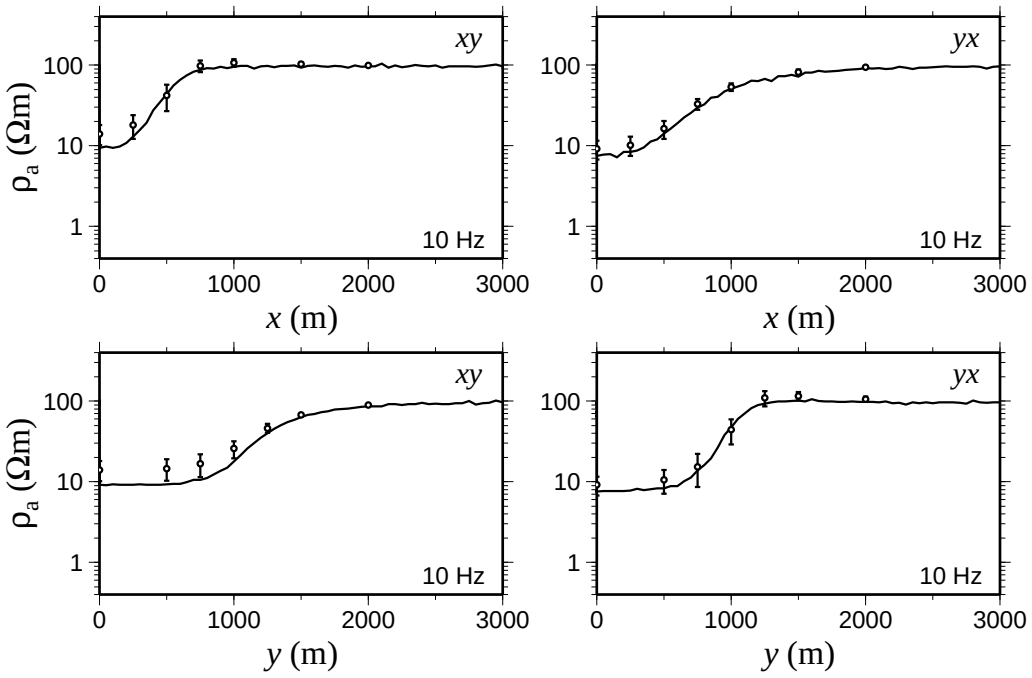


Figure 8.4: These figures show for the first MT example (the 3D-1A model) the apparent resistivities corresponding to the off-diagonal impedance tensor elements (i.e., the $xy$ and $yx$ elements). The results are for the frequency of 10 Hz. The top and bottom panels show the results for the profiles along the $x$ and $y$ axes, respectively. The finite-volume solutions are shown as lines and the results from Zhdanov et al. (1997) are shown as circles with error bars.

Figures 8.3 and 8.4 show the apparent resistivities for the off-diagonal impedance tensor elements (i.e., the $xy$ and $yx$ elements) for frequencies 0.1 and 10 Hz, respectively (because the observation profiles were along the coordinate axes that are in the planes of vertical symmetry of the block, the diagonal elements are zero; Zhdanov et al., 1997). The results are shown for both of the observation profiles described above. The finite-volume solutions are compared with the results from Zhdanov et al. (1997). The reference solutions are the average values and the standard deviations of several data-sets generated by several research groups that had been invited to participate in the COMMEMI project. The vector representation of the electric field at horizontal and vertical sections is shown for the two frequencies in Figures 8.5 and 8.6.

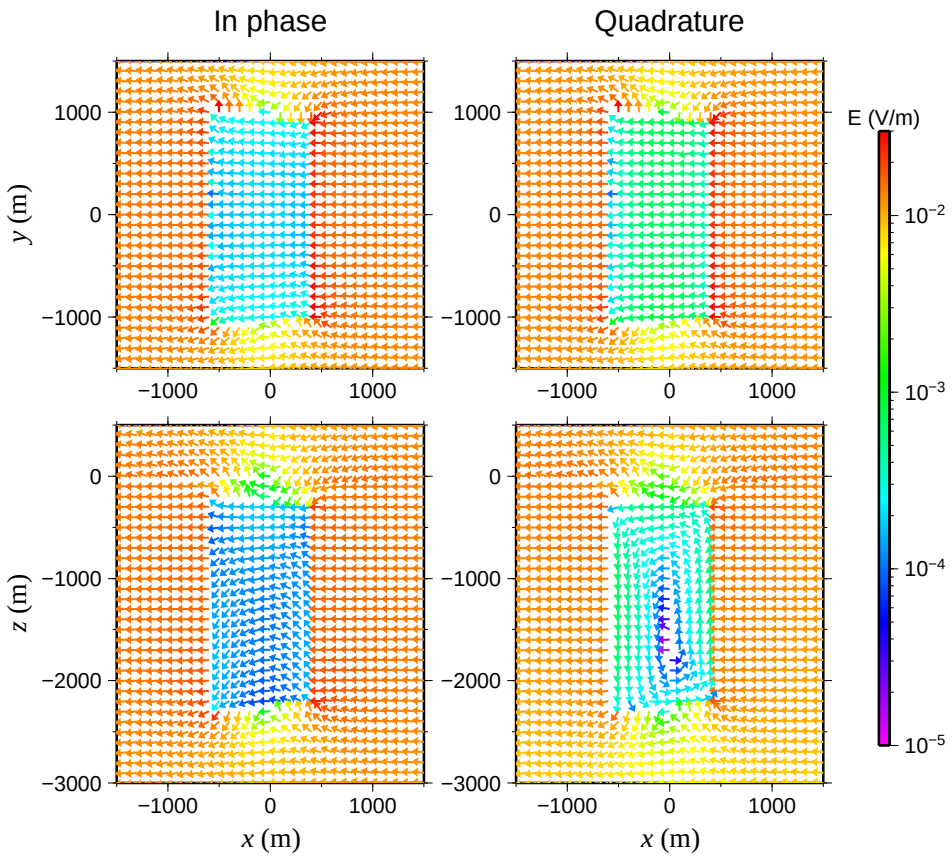


Figure 8.5: The total electric field for the first MT example (the 3D-1A model) and for the frequency of 0.1 Hz at a horizontal section at the depth of −275 m (top panels) and at a vertical section at $y = 0$ m (bottom panels) passing through the anomalous region.

The vertical section is the $y = 0$ m plane, and the horizontal section is the $z = -275$ m plane. For these sections, the MT source polarization was along the $x$ axis.

### 8.6.3 Example 2: 3D-2A model

The second example is more complicated. It comprises a three-layer earth with conductivities of 0.1, 0.01 and 10 S/m from top to bottom. The top and middle layers have thicknesses of 10 and 20 km, respectively, and the third layer has an infinite depth (see Figure 8.7). Two adjacent rectangular prisms, with conductivities of 1 and

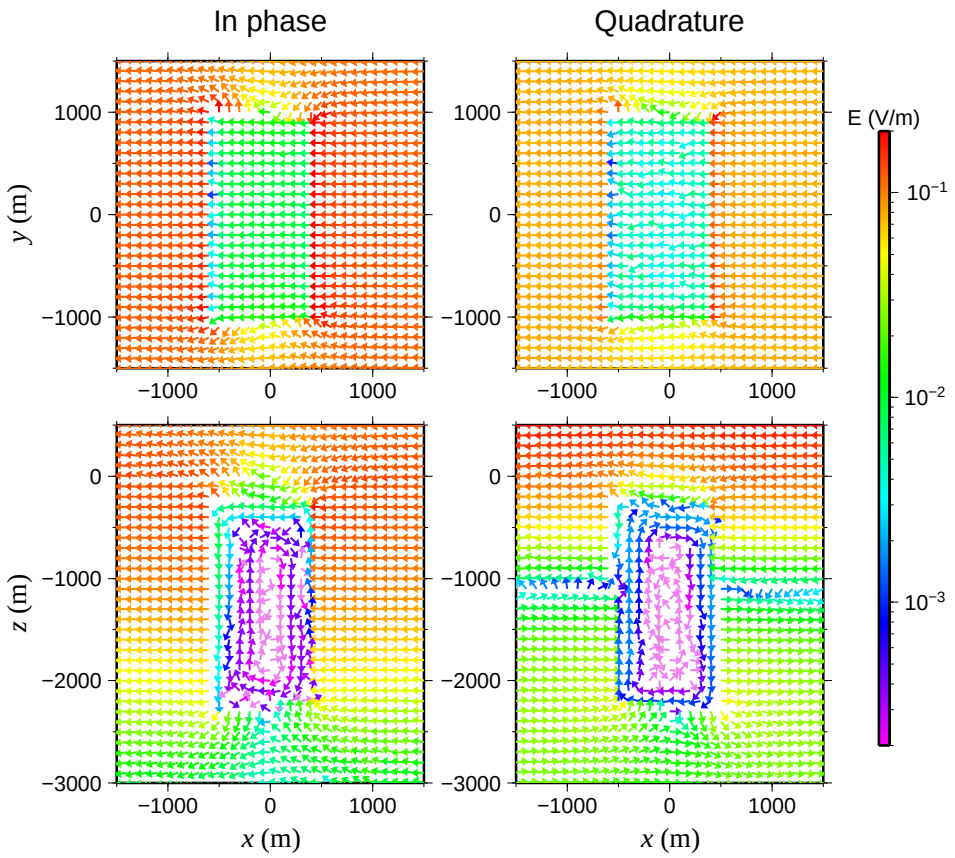


Figure 8.6: The total electric field for the first MT example (the 3D-1A model) and for the frequency of 10 Hz at a horizontal section at the depth of −275 m (top panels) and at a vertical section at $y = 0$ m (bottom panels) passing through the anomalous region.

0.01 S/m are located inside the first layer. They have the same thickness as this layer and their horizontal extents are 20 and 40 km in the $x$ and $y$ directions, respectively. The centres of the top of the conductive and resistive blocks are at $(-10, 0, 0)$ and $(10, 0, 0)$ km, respectively. There is a single observation profile at the earth-air interface from $(-60, 0, 0)$ to $(60, 0, 0)$ km. Solutions for this model are obtained for three frequencies: 0.1, 0.01 and 0.001 Hz. The entire computational domain had dimensions of $400 \times 400 \times 400$ km which was comprised of $348,664$ and $57,906$ tetrahedral and Voronoï cells, respectively, and $410,981$ Delaunay edges. Vertical sections of the

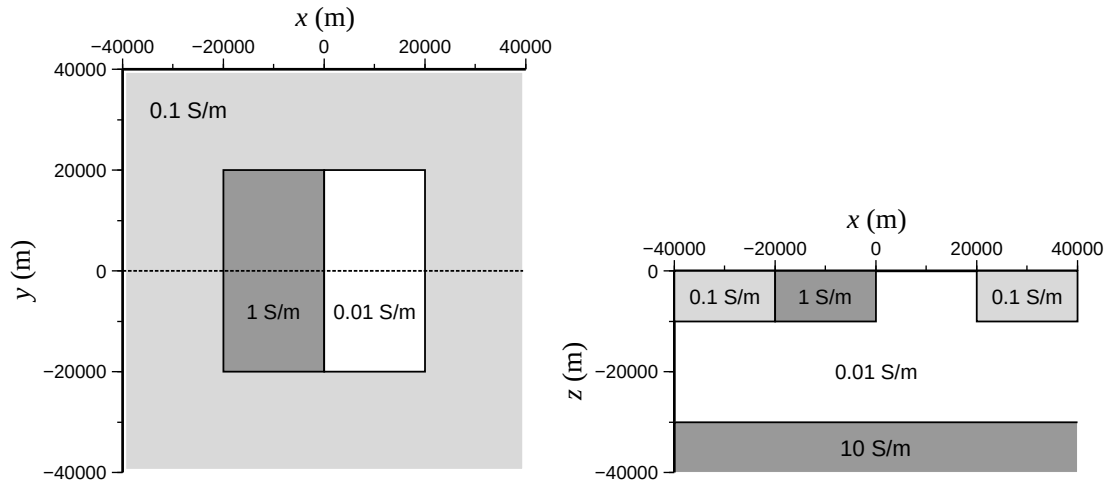


Figure 8.7: The left and right panels show, respectively, the plan and side views of the 3D-2A model used in the second example. There are three layers with distinct conductivities. Also, there are two blocks inside the first layer with one of them having the same conductivity as the second layer. The observation profile is shown by a dashed-line.

tetrahedral and Voronoï grids are shown in Figure 8.8. The observation points were spaced 500 m apart along the observation profile and for each observation point a tetrahedron with the edge size of 100 m was inserted inside the grid. The total computation time and memory usage for solving this problem using the MUMPS direct solver were 132 s and 12.1 Gbytes, respectively.

The off-diagonal components of apparent resistivity and phase tensors are calculated and compared with the integral-equation solutions reported by Wannamaker (1991). The solutions for frequencies 0.001, 0.01 and 0.1 Hz are shown in Figures 8.9, 8.10 and 8.11, respectively. There is good agreement between the two numerical solutions, particularly for the lower frequencies. For the $x$-directed source polarization, Figure 8.12 shows the electric field at a horizontal section at $z = -250$ m for the three frequencies.

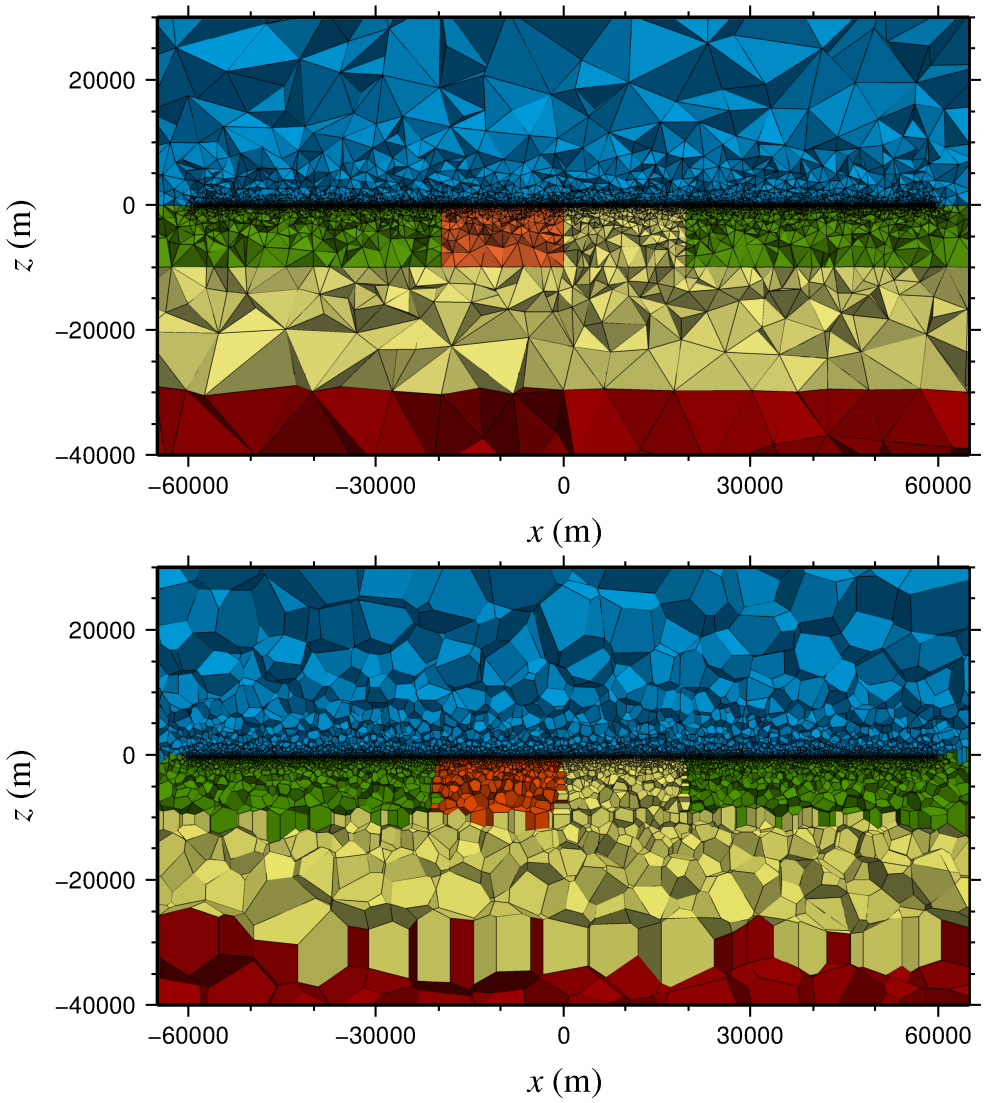


Figure 8.8: Top and bottom panels show, respectively, vertical sections at the $y = 0$ m plane through the tetrahedral and Voronoï grids used for solving the problem in the second MT example. Grids are only refined at the observation points. The Voronoï faces that cross the interfaces are arbitrarily colored.

## 8.7 Conclusions

This chapter dealt with the modelling of MT data using the finite-volume method on staggered tetrahedral-Voronoï grids. The FV scheme that was used for the modelling of CSEM data in the previous chapter was modified for a different boundary condition.

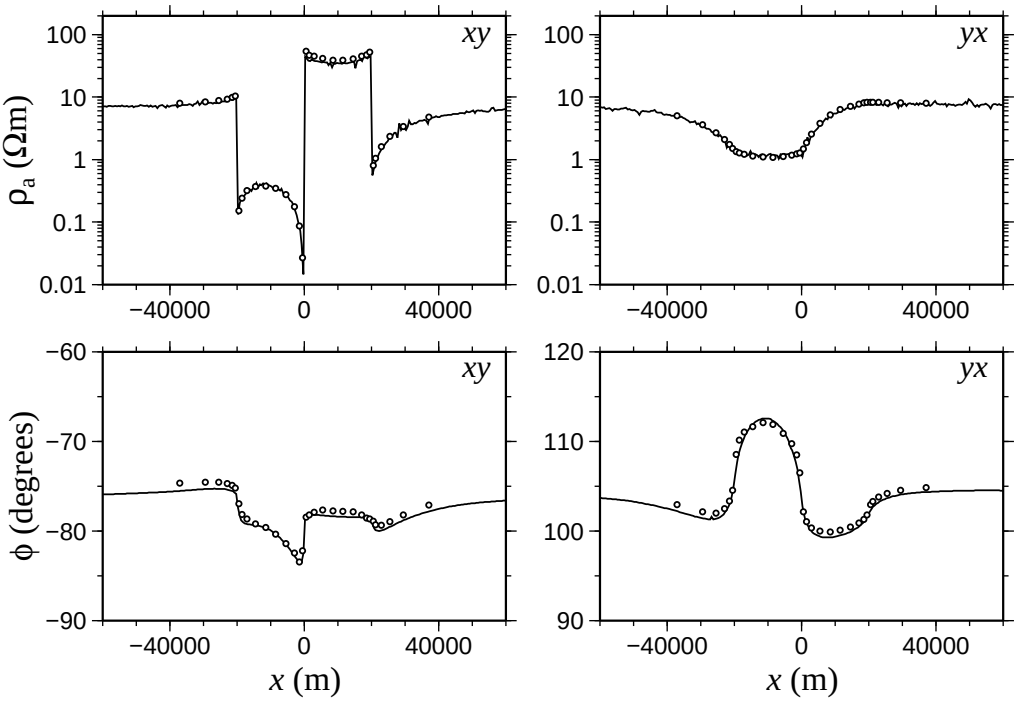


Figure 8.9: These figures show for the second MT example (the 3D-2A model) the apparent resistivities (top panels) and phases (bottom panels) corresponding to the off-diagonal impedance tensor elements (i.e., the $xy$ and $yx$ elements). The results are for the frequency of 0.001 Hz. The finite-volume solutions are shown as lines and the results from Wannamaker (1991) are shown as circles.

Specifically, the homogeneous Dirichlet boundary condition, which was used for the CSEM method, was replaced with an inhomogeneous Dirichlet condition for the MT method. Analytical expressions for the MT fields due to a homogeneous halfspace and 1-D earth were used for calculating the boundary values. This boundary condition assumes a plane wave which is normally incident to the earth-air interface.

For verifying the MT scheme, two benchmark examples from the COMMEMI project were used. The first model was an anomalous block in a homogeneous halfspace (3D-1A). For this example, the apparent resistivity along two profiles was compared with the average of several data-sets from the COMMEMI project. In the second example (3D-2A), the finite-volume solutions for apparent resistivity and phase were

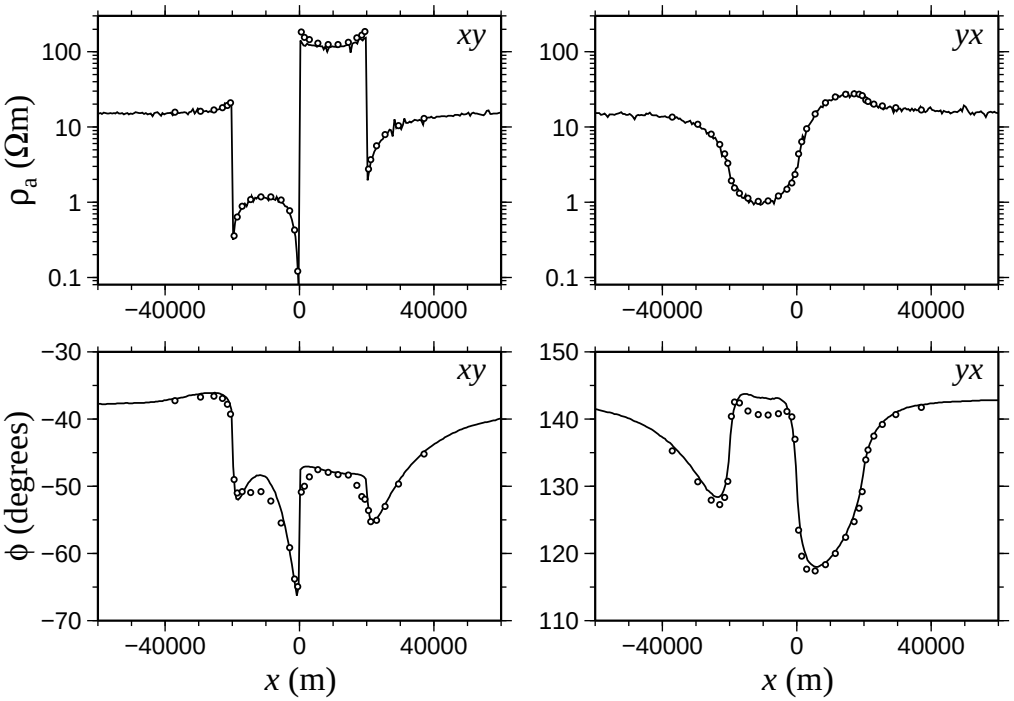


Figure 8.10: These figures show for the second MT example (the 3D-2A model) the apparent resistivities (top panels) and phases (bottom panels) corresponding to the off-diagonal impedance tensor elements (i.e., the $xy$ and $yx$ elements). The results are for the frequency of 0.01 Hz. The finite-volume solutions are shown as lines and the results from Wannamaker (1991) are shown as circles.

compared with IE solutions from the literature. There was a good agreement between the finite-volume results and the reference solutions which showed the efficiency of the finite-volume MT scheme.

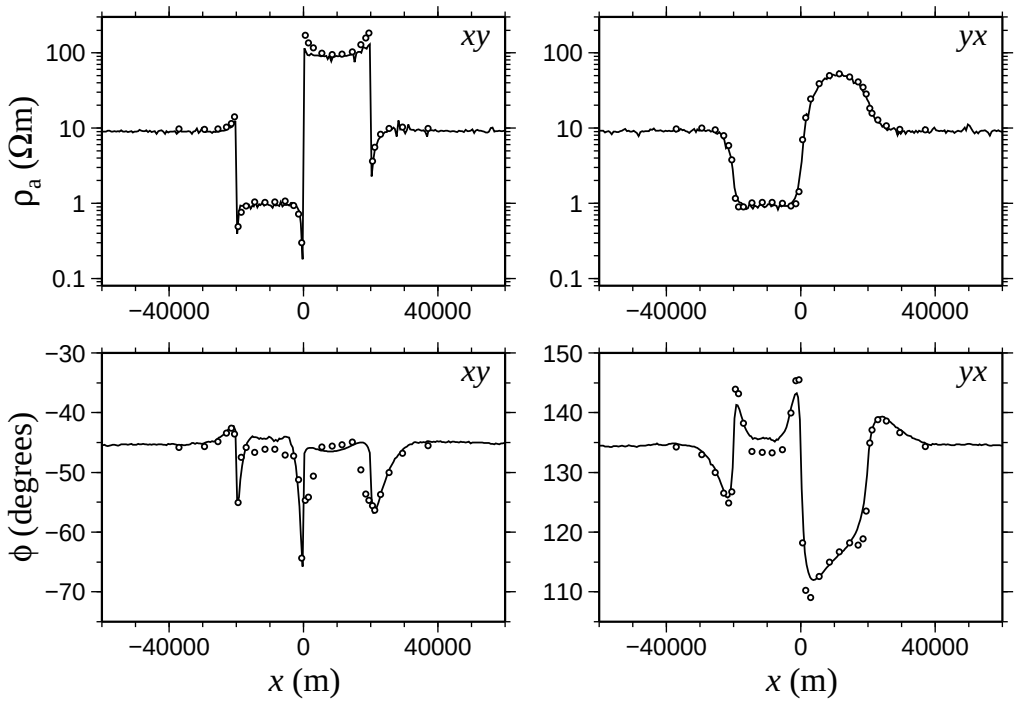


Figure 8.11: These figures show for the second MT example (the 3D-2A model) the apparent resistivities (top panels) and phases (bottom panels) corresponding to the off-diagonal impedance tensor elements (i.e., the $xy$ and $yx$ elements). The results are for the frequency of 0.1 Hz. The finite-volume solutions are shown as lines and the results from Wannamaker (1991) are shown as circles.

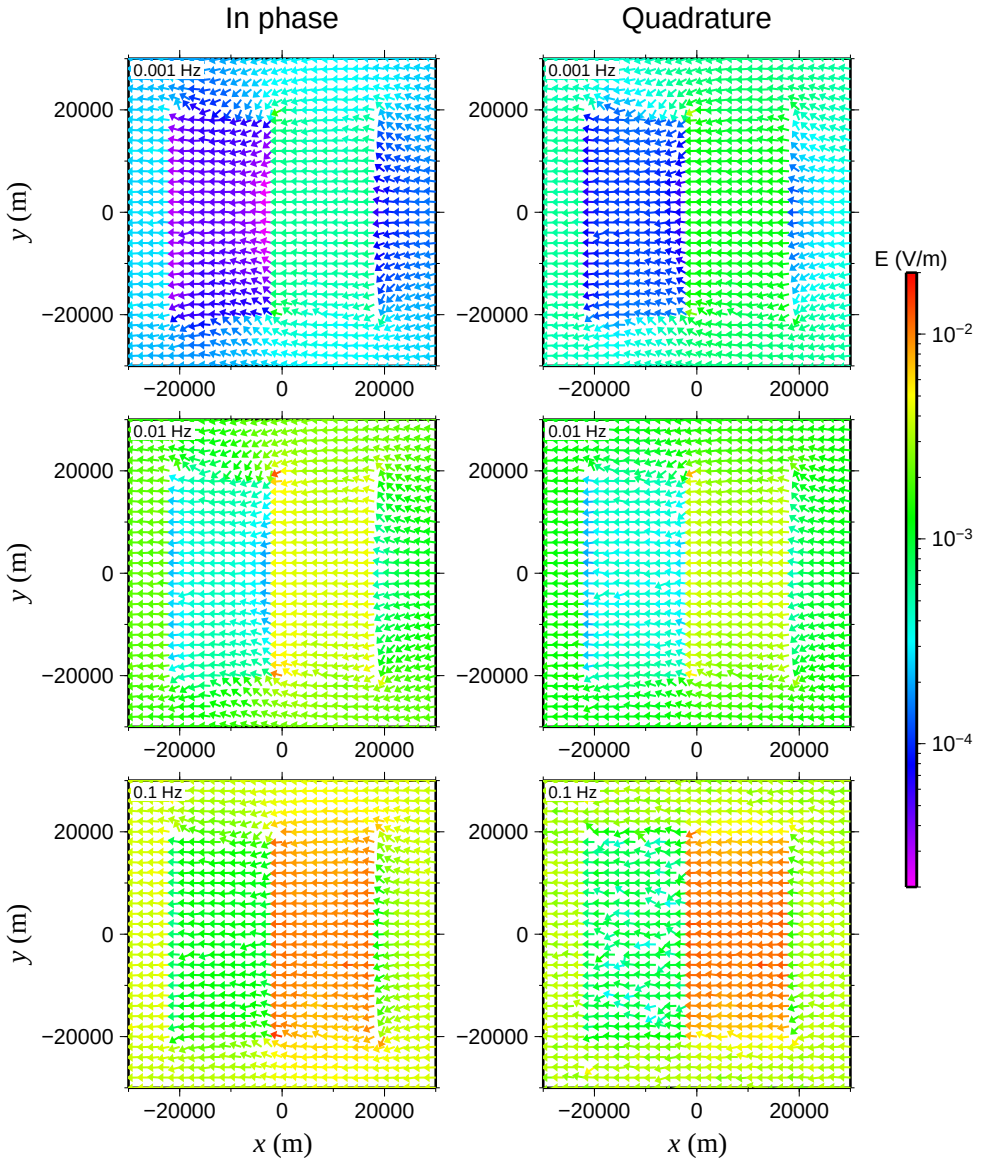


Figure 8.12: The total electric field for the second MT example (the 3D-2A model) and for the three frequencies of 0.001, 0.01 and 0.1 Hz at a horizontal section at the depth of −250 m. The section passes through the first layer and the two blocks that are embedded inside it.

# Chapter 9

# Finite-volume modelling of CSEM data using the potential formulation

## 9.1 Introduction

In the last two chapters, the direct EM-field formulation of Maxwell's equations was discretized and solved for the CSEM and MT cases. In this chapter, the alternative formulation of Maxwell's equations, namely, the EM potential formulation, is discretized and solved using the finite-volume method. The same type of grids as used in the previous chapters is used, i.e., staggered tetrahedral-Voronoï grid. As will be explained in the following paragraphs, the main feature offered by this potential approach is the improved conditioning of the resulting problem compared to the direct approach.

In the potential method, the electric and magnetic fields are replaced with their representations in terms of magnetic vector and electric scalar potentials. Therefore,

in this method the unknowns of the problem are these potentials. Since these potentials coexist in the grid, the number of unknowns in the problems arising from this approach is larger than in the counterpart problems from the direct method, and hence, the resulting system of equations is also larger. However, this new system is better conditioned than the system in the direct method and can be more easily solved using iterative solvers. Also, the problem in the potential approach can be gauged in order to prevent the presence of spurious modes in the numerical solutions which results in the stability of the solutions at low frequencies. This gauging enforces uniqueness on scalar and vector potentials which enables studying the physics of inductive and galvanic components of numerical solutions.

The earliest applications of the potential approach in the geophysics literature appear in the integral-equation studies by Lajoie and West (1976) and Walker and West (1991). In the finite-element domain, Badea et al. (2001) present a time-harmonic nodal-based method on tetrahedral grids for isotropic media which is expanded by Puzyrev et al. (2013) to anisotropic media. Mitsuhata and Uchida (2004) decompose the magnetic field into vector and scalar potentials on rectilinear grids and use nodal and edge-based basis functions. Ansari and Farquharson (2014) decompose the electric field into these potentials and use the nodal and edge-based basis functions on tetrahedral grids. In the finite-difference domain, LaBrecque (1999) and Druskin et al. (1999) use, respectively, the standard central finite-difference grids and staggered grids for isotropic media in the frequency domain. Newman and Alumbaugh (2002) also use the finite-difference method on staggered grids for simulating induction log responses and for transverse anisotropy. Hou et al. (2006) use a similar approach to LaBrecque (1999) for borehole measurements and for anisotropic media. Haber et al. (2000) and Haber (2002) use the finite-volume method and develop, respectively, frequency-domain and time-domain methods for isotropic media using staggered grids. Novo

et al. (2007) extends the frequency-domain finite-volume method for cylindrical grids and for anisotropic media. Recently, Weiss (2013) uses the finite-volume method on staggered rectilinear grids for the Lorenz-gauged formulation and anisotropic media, and Weiss (2014) uses a similar finite-difference approach for overset grids. The finite-volume scheme developed here can be seen as a generalization of the method presented by Haber et al. (2000) for unstructured tetrahedral grids.

Ill-posedness is the main drawback of the problems that arise from the discretization of the direct EM-field formulation of Maxwell's equations. There is almost always an air region present in the numerical domain. The vanishing conductivity in this region eliminates the second term in equation 7.3 which results in the singularity of the problem. Also, these problems are not strongly elliptic (the solution is not smooth) even inside the ground where conductivity is nonzero (Aruliah et al., 2001). The problems that arise from the potential formulation of Maxwell's equation do not suffer from these issues. In these problems, the system of equations is weakly coupled and it is strongly elliptic. Therefore, unlike the direct EM-field method, potential schemes can be efficiently solved using standard iterative solvers.

Discretization of Maxwell's equations (either the direct or potential formulations) can result in the loss of continuity of the numerical solution for low frequencies. This lack of continuity causes discrepancy between the eigenvectors of the discretized solution and the continuous solution (Schroeder and Wolff, 1994) a problem which is called spurious modes. This discrepancy results in error in the numerical solution. Wong and Cendes (1988) attribute this error to the incorrect approximation of the null-space of the curl operator (see LaBrecque, 1999, for more details). This problem can be overcome in the potential method by applying a gauge correction (specifying the divergence of magnetic vector potential). Coulomb gauge and Lorentz gauge are the common choices which provide the same accuracy (Morisue, 1993). In this study,

Coulomb gauge is considered for improving the solutions at low frequencies. This gauge has been extensively used in the potential approach (e.g., Biro and Preis, 1989; LaBrecque, 1999; Haber et al., 2000; Badea et al., 2001; Newman and Alumbaugh, 2002; Mitsuhata and Uchida, 2004).

One of the consequences of the application of gauge corrections is the enforcement of uniqueness on scalar and vector potentials. In the potential method, the problem is solved for scalar and vector potentials and then electric and magnetic fields are constructed from these potentials using relations 6.20 and 6.18. While the constructed electric and magnetic fields are always unique, it is well-known that potentials are not (Biro and Preis, 1989): according to relation 6.18, we can add any curl-free component to the magnetic potential without changing the magnetic field. The curl of the vector potential is already given by relation 6.18. The Coulomb gauge adds an additional constraint by specifying the divergence of this potential ($\nabla \cdot \mathbf{A} = 0$). With its curl and divergence specified, the vector potential is uniquely defined. As the electric field is also unique, relation 6.20 suggests that the gradient of the scalar potential should be unique as well.

The uniqueness of potentials allows studying the physics of inductive and galvanic effects and their relative contribution to the fields that are observed. The two terms in equation 6.20 which contain vector and scalar potentials correspond, respectively, to the inductive and galvanic parts of the electric field. Galvanic and inductive phenomena correspond, respectively, to galvanic currents and eddy currents. The origin of galvanic currents in a conductive host medium is either the regional induction in this host, by a magnetic source, or the flow of electric charge which is injected inside the ground by a grounded electric source. Inductive current, in contrast, is the vortex eddy current in the anomalous region which is due to a changing magnetic field in this region (West and Macnae, 1987).

The next section deals with a staggered discretization of the potential formulation of Maxwell's equations using tetrahedral and Voronoï grids. In the following sections, the presented scheme is verified using the same examples as were used in Chapter 7. Solutions for the inductive and galvanic parts are also studied for these examples. Additionally, an accuracy study is conducted in order to make a comparison between the CSEM scheme presented in this chapter and the scheme presented in Chapter 7. The two schemes are also compared in terms of required computation resources for both direct and iterative solvers.

## 9.2 The CSEM problem

In Section 6.4 it was shown that electric and magnetic fields can be written in terms of potentials:

$$\mathbf{E} = -i\omega\mathbf{A} - \nabla\phi \tag{9.1}$$

$$\nabla \times \mathbf{A} = \mu_0\mathbf{H} \tag{9.2}$$

where $\mathbf{A}$ is the magnetic vector potential and $\phi$ is the electric scalar potential. Using these relations, the Helmholtz equation for electric field (relation 7.3) can be rewritten as

$$\nabla \times \nabla \times \mathbf{A} + i\omega\mu_0\sigma\mathbf{A} + \sigma\mu_0\nabla\phi = \mu_0\mathbf{J}_p + \mu_0\nabla \times \mathbf{M}_p. \tag{9.3}$$

As mentioned in the previous section, the null-space of the curl operator can result in spurious modes at low frequencies. This null-space can be eliminated by considering a Coulomb gauge and adding $-\nabla(\nabla \cdot \mathbf{A})$ to the left-hand-side of this equation:

$$\nabla \times \nabla \times \mathbf{A} - \nabla(\nabla \cdot \mathbf{A}) + i\omega\mu_0\sigma\mathbf{A} + \sigma\mu_0\nabla\phi = \mu_0\mathbf{J}_p + \mu_0\nabla \times \mathbf{M}_p. \tag{9.4}$$

Assuming the Coulomb gauge ($\nabla \cdot \mathbf{A} = 0$) is satisfied, the added term vanishes and equation 9.3 remains unchanged. However, using the vector identity 2.11 this relation can be written as

$$-\nabla^2 \mathbf{A} + i\omega\mu_0\sigma\mathbf{A} + \sigma\mu_0\nabla\phi = \mu_0\mathbf{J}_p + \mu_0\nabla \times \mathbf{M}_p, \tag{9.5}$$

which shows that the curl-curl operator in equation 9.3 is replaced by a Laplacian operator, and it is well known that the discretized form of the Laplacian operator is very stable numerically (Badea et al., 2001).

Similar to the direct EM-field method, the Helmholtz equation above can be written for each tetrahedral edge in the grid. However, in this potential approach the number of unknowns equals the number of tetrahedral edges plus the number of tetrahedral nodes. Therefore, we need an additional equation which can be written for each node of the grid and that can be solved with the Helmholtz equation. This equation is derived by taking the divergence of the Ampère's law (relation 6.3) which results in the equation of conservation of charge:

$$-\nabla \cdot \sigma\mathbf{E} = \nabla \cdot \mathbf{J}_p. \tag{9.6}$$

Replacing $\mathbf{E}$ with potentials gives

$$i\omega\nabla \cdot \sigma\mathbf{A} + \nabla \cdot \sigma\nabla\phi = \nabla \cdot \mathbf{J}_p. \tag{9.7}$$

The Coulomb gauge can be applied by appropriate boundary conditions. If we take the divergence of equation 9.4 and use relation 9.6 we have

$$\nabla^2 (\nabla \cdot \mathbf{A}) = 0, \tag{9.8}$$

which means that $\nabla \cdot \mathbf{A}$ is a harmonic function (see Section 2.3). Harmonic functions over a region only have maxima or minima on the boundary of that region. Therefore, if $\nabla \cdot \mathbf{A}$ vanishes on the boundary of the domain, it will also vanish inside the region and the Coulomb gauge is satisfied. It can be easily shown that if $\mathbf{A}$ vanishes on a boundary that is located at infinity its divergence also vanishes on this boundary. Therefore, here, equations 9.5 (or 9.4) and 9.7 are solved with a homogeneous Dirichlet boundary condition for the vector and scalar potentials. (The solution of the ungauged problem, i.e., equations 9.3 and 9.7, is also investigated.)

## 9.3 Discretization of the problem

For the discretization of the first governing equation derived in the previous section (relation 9.4) it is more convenient to write this equation in terms of the following three relations

$$\nabla \times \mathbf{H} - \mu_0^{-1} \nabla \psi + i\omega\sigma\mathbf{A} + \sigma\nabla\phi = \mathbf{J}_p + \nabla \times \mathbf{M}_p \tag{9.9}$$

$$\mu_0 \mathbf{H} = \nabla \times \mathbf{A} \tag{9.10}$$

$$\psi = \nabla \cdot \mathbf{A}. \tag{9.11}$$

For the staggered discretization that is considered here, the newly defined parameter $\psi$ and the scalar potential $\phi$ are defined at tetrahedral nodes (centres of Voronoï cells). The vector potential $\mathbf{A}$, $\nabla\psi$ and $\nabla\phi$ are defined at tetrahedral edges, i.e., at the same location as the former $\mathbf{E}$. However, according to relation 6.20, $\mathbf{A}$ and $\mathbf{E}$ have opposite directions. The finite-volume discretization of the above relations follows by integrating equations 9.9 and 9.10, respectively, over Voronoï and tetrahedral faces, and by integrating equation 9.11 and the equation of conservation of charge (equation

9.7) over Voronoï cells. (Details are provided in the following paragraphs.) Subsequently, $\mathbf{H}$ and $\psi$ in equation 9.9 are eliminated by the expressions derived for these parameters from, respectively, equations 9.10 and 9.11.

The integration of equation 9.9 over a Voronoï face and using Stokes' theorem results in

$$\oint_{\partial S^V} \mathbf{H} \cdot d\mathbf{l}^V - \mu_0^{-1} \iint_{S^V} \nabla\psi \cdot d\mathbf{S}^V + i\omega\sigma \iint_{S^V} \mathbf{A} \cdot d\mathbf{S}^V + \sigma \iint_{S^V} \nabla\phi \cdot d\mathbf{S}^V = \iint_{S^V} \mathbf{J}_p \cdot d\mathbf{S}^V + \oint_{\partial S^V} \mathbf{M}_p \cdot d\mathbf{l}^V, \quad (9.12)$$

where the parameters and quantities are the same as those described for equation 7.7. The same approach as was used for the discretization of relations 7.6 and 7.7 can be used here for discretizing this relation: the normal components of $\mathbf{A}$, $\nabla\phi$ and $\nabla\psi$ over the Voronoï face ($S^V$) and the tangential component of $\mathbf{H}$ along the Voronoï edges ($\partial S^V$) are replaced by their averages such that the results of the integrations in the equation above equal their respective terms in the following relation. By considering the $m$th Delaunay edge and orthogonal to it the $m$th Voronoï face, and with $W$ indicating the number of Voronoï edges that surround this face, equation 9.12 is discretized as

$$\sum_{k=1}^{W_m^V} H_{m,k}\, l_{m,k}^V - \frac{S_m^V}{\mu_0} \left(\psi_{2m} - \psi_{1m}\right)/l_m^D + i\omega\, \sigma_m A_m S_m^V + \sigma_m S_m^V \left(\phi_{2m} - \phi_{1m}\right)/l_m^D = \sum_{k=1}^{W_m^V} \frac{M_{p_{m,k}}}{S_{m,k}^D} + J_{p_m}, \quad (9.13)$$

where the average values of $\nabla\phi$ and $\nabla\psi$ are approximated by a differencing scheme, $H$ and $A$ are average values for $\mathbf{H}$ and $\mathbf{A}$ in relation 9.12, respectively, and for deriving the source terms on the right-hand side the definitions given in relation 7.5 are used.

$S$ and $l$ give face area and edge lengths, respectively, and the direction of $A$ is from $(\psi_1, \phi_1)$ to $(\psi_2, \phi_2)$.

In order to derive an expression in terms of $H$, we integrate equation 9.10 over tetrahedral (Delaunay) faces and apply Stokes's theorem:

$$\oint_{\partial S^D} \mathbf{A} \cdot d\mathbf{l}^D = \mu_0 \iint_{S^D} \mathbf{H} \cdot d\mathbf{S}^D. \tag{9.14}$$

By replacing $\mathbf{H}$ and $\mathbf{A}$ by their averages, respectively, over the $j$th tetrahedral face and along the edges of this face this relation is discretized as

$$\sum_{q=1}^{W_j^D} A_{j,q}\, l_{j,q}^D = \mu_0\, H_j S_j^D. \tag{9.15}$$

The term $\psi$, which is defined as the divergence of the vector potential, is defined at the centre of the Voronoï cells (see Figure 9.1). To derive an expression for this parameter, relation 9.11 is integrated over a Voronoï cell and the divergence theorem used:

$$\iiint_{V^V} \psi \, dV = \oiint_{S^V} \mathbf{A} \, d\mathbf{S}^V. \tag{9.16}$$

This relation can be discretized for the $n$th Voronoï cell by using the average values of $\psi$ and $\mathbf{A}$ over the volume of this cell and over its Voronoï faces, respectively:

$$\psi_n V_n^V = \sum_{u=1}^{P_n^V} A_{n,u}\, S_{n,u}^V, \tag{9.17}$$

where $V$ is the volume of this cell and $P$ gives the number of faces of this Voronoï cell.

By deriving expressions for $H$ and $\psi$ from relations 9.15 and 9.17, respectively, and substituting in 9.13 the discretized form of the first governing equation (relation

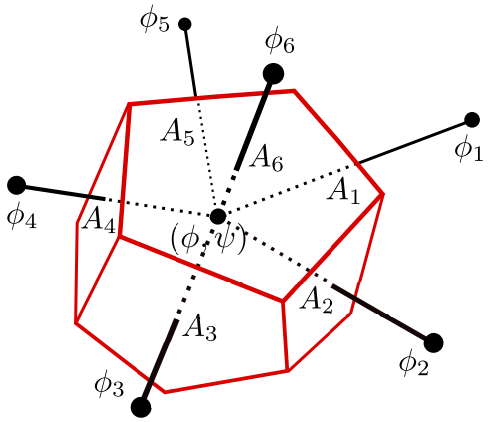


Figure 9.1: An example for a Voronoï cell and the location of different parameters used for the discretization of governing equations for the EM potential method. $\psi$ and $\phi$ (divergence of $A$ and the scalar potential) are collocated at the centre of Voronoï cells (at tetrahedral nodes) and $A$ (vector potential) is defined along tetrahedral edges. The $\phi$ values that belong to the neighbouring Voronoï cells are also shown (numbered 1 to 6).

9.4) is derived:

$$\sum_{k=1}^{W_m^V}\left(\left(\sum_{q=1}^{W_{m,k}^D} A_{m,k,q}\, l_{m,k,q}^D\right)\frac{l_{m,k}^V}{\mu_0 S_{m,k}^D}\right) - \frac{S_m^V}{\mu_0\, l_m^D}\left(\left[\frac{1}{V^V}\sum_{u=1}^{P^V} A_u S_u^V\right]_{2_m} - \left[\frac{1}{V^V}\sum_{u=1}^{P^V} A_u S_u^V\right]_{1_m}\right)$$
$$+ i\omega\,\sigma_m A_m S_m^V + \sigma_m S_m^V\left(\phi_{2_m} - \phi_{1_m}\right)/l_m^D = \sum_{k=1}^{W_m^V}\frac{M_{p_{m,k}}}{S_{m,k}^D} + J_{p_m}. \tag{9.18}$$

Note that terms with index $j$ in relation 9.15 possess index $(m,k)$ in the equation above, and terms with index $n$ in relation 9.17 possess either index $2_m$ or $1_m$ in the relation above. Similar to equation 7.10, the relation above is written for all the $N$ tetrahedral edges in the mesh ($m = 1, 2, 3, \cdots, N$). The unknown vector potentials ($A$) associated with the first term in the relation above correspond to the edges that are used for approximating the curl-curl operator for the edge $m$ while the unknowns in the second term correspond to the faces of each of the two Voronoï cells that

correspond to the endpoints of this tetrahedral edge (see Figure 9.2). Also, as for equation 7.10, terms $l^D_{m,k,q}$ in the relation above possess sizes equal to the lengths of the corresponding tetrahedral edges and a positive or negative sign which is determined by their mutual orientation with the Voronoï edges ($l^V_{m,k}$ terms). $S^V_u$ also have sizes equal to the areas of the corresponding Voronoï faces and a positive or negative sign according to the inward or outward direction of the tetrahedral edges (with respect to the related Voronoï cell) that correspond to these faces. Equation 9.18 represents the gauged problem. For the ungauged problem, the second term in this relation which corresponds to the added term for the Coulomb gauge, i.e., the second term in relation 9.9, is ignored:

$$\sum_{k=1}^{W^V_m} \left( \left( \sum_{q=1}^{W^D_{m,k}} A_{m,k,q}\, l^D_{m,k,q} \right) \frac{l^V_{m,k}}{\mu_0 S^D_{m,k}} \right) + \, i\omega\, \sigma_m A_m S^V_m + \sigma_m S^V_m \left(\phi_{2_m} - \phi_{1_m}\right) / l^D_m = \sum_{k=1}^{W^V_m} \frac{M_{p_{m,k}}}{S^D_{m,k}} + J_{p_m}. \quad (9.19)$$

This relation is the discretized form of equation 9.3.

For the discretization of the second governing equation (conservation of charge, relation 9.7) it is integrated over Voronoï cells (as was done for relation 9.11) and the divergence theorem used:

$$i\omega \oiint_{S^V} \sigma \mathbf{A} \cdot d\mathbf{S}^V + \oiint_{S^V} \sigma \nabla\phi \cdot d\mathbf{S}^V = \oiint_{S^V} \mathbf{J}_p \cdot d\mathbf{S}^V. \quad (9.20)$$

Similar to the finite-volume approaches already employed, for the Voronoï cell $n$, we replace terms $A$ and $\nabla\phi$ with their averages over the faces to obtain

$$i\omega \sum_{u=1}^{P^V_n} \sigma_{n,u}\, A_{n,u}\, S^V_{n,u} + \sum_{u=1}^{P^V_n} \sigma_{n,u}\, S^V_{n,u} \left(\phi_{2_{n,u}} - \phi_{1_{n,u}}\right) / l^D_{n,u} = \sum_{u=1}^{P^V_n} J_{p_{n,u}}, \quad (9.21)$$

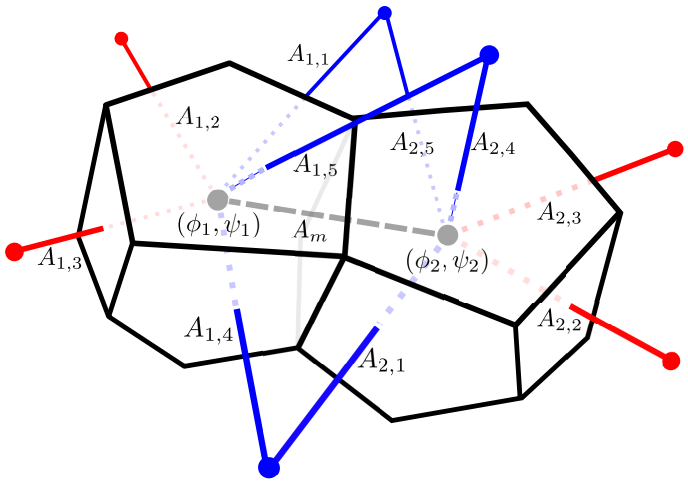


Figure 9.2: An example which shows the unknown vector and scalar potentials engaged in approximating the first governing equation (relation 9.18) for a tetrahedral edge (or Voronoï face). This edge is shown by a dashed line and the unknown potential at this edge is $A_m$. The edges that are used for approximating the curl-curl operator (the first term in relation 9.18) are shown in blue. All the edges (red and blue) are used by the second term of this relation for approximating $\nabla\psi$ which is added for Coulomb gauge correction (in other words, all the edges are used for approximating the Laplacian operator in relation 9.5). For the sake of clarity, not all the tetrahedral edges are shown in this figure.

where, again, $\nabla\phi$ is approximated using a differencing scheme. In the relation above, $\phi_1$ is an average value of this quantity over the Voronoï cell $n$, and $\phi_2$ values are averages for its neighbouring Voronoï cells (see Figure 9.1). Also, the $S$ terms possess sizes equal to the areas of the corresponding Voronoï faces and a positive or negative sign according to the inward or outward direction of the related tetrahedral edges. Conductivity values ($\sigma$) which correspond to Voronoï faces are, as in the previous schemes, area-weighted averages of the conductivities of the tetrahedra that share the tetrahedral edges that correspond to these Voronoï faces (see Figure 7.3).

## 9.4 Solution of the problem

The discretized form of the governing equations, i.e., relations 9.18 and 9.21, can be written, respectively, for all the $N$ tetrahedral edges (or Voronoï faces) and $M$ tetrahedral nodes (or Voronoï cells) in the grid. The system of equations that is formed is solved for unknown vector and scalar potentials that are defined, respectively, at the tetrahedral edges and nodes. In order to obtain a real-valued system, the potentials are decomposed into their real and imaginary components:

$$\begin{aligned} A &= A_{re} + iA_{im} \\ \phi &= \phi_{re} + i\phi_{im}. \end{aligned} \tag{9.22}$$

The resulting block matrix equation has the following form:

$$\begin{pmatrix} \mathbf{A}' & -\omega\mathbf{B}' & \mathbf{C}' & 0 \\ \omega\mathbf{B}' & \mathbf{A}' & 0 & -\mathbf{C}' \\ 0 & -\omega\mathbf{D}' & \mathbf{E}' & 0 \\ \omega\mathbf{D}' & 0 & 0 & \mathbf{E}' \end{pmatrix} \begin{pmatrix} \mathbf{A}_{re} \\ \mathbf{A}_{im} \\ \Phi_{re} \\ \Phi_{im} \end{pmatrix} = \begin{pmatrix} \mathbf{S}_1 \\ 0 \\ \mathbf{S}_2 \\ 0 \end{pmatrix}. \tag{9.23}$$

The components of matrices $\mathbf{A}'$ and $\mathbf{E}'$ are functions of the sizes of the tetrahedral and Voronoï faces and edges, $\mathbf{B}'$ is a diagonal matrix with nonzero components equal to $\sigma$, $\mathbf{C}'$ has two nonzero components inside each row equal to $\sigma/l^D$ and $-\sigma/l^D$, and the nonzero components of $\mathbf{D}'$ are $\sigma S^V$. $\mathbf{A}_{re}$, $\mathbf{A}_{im}$, $\Phi_{re}$ and $\Phi_{im}$ are arrays that contain the real and imaginary parts of the unknown vector and scalar potentials, and $\mathbf{S}_1$ and $\mathbf{S}_2$ are arrays that contain the source terms. The components of these arrays are the summation of the right-hand-sides of equations 9.18 and 9.21. An example for the coefficient matrix in the equation above is shown in Figure 7.4. It can be readily seen that the coefficient matrix is not symmetric (unlike the matrix for the direct method).

The system of equations above is solved here using the MUMPS sparse direct solver (Amestoy et al., 2006) and iterative solvers GMRES and BiCGStab from the SPARSKIT package (Saad, 1990). The primary solutions of the problem are the vector and scalar potentials. Electric and magnetic field values are calculated from these potentials using relations 6.20 and 6.18, respectively. Experiments show that the gauged and ungauged approaches result in very similar solutions in terms of electric and magnetic fields but the primary solutions from these two methods are completely different: while the gauged scheme results in reasonable solutions for the galvanic and inductive parts (as will be seen in the next section), the results from the ungauged scheme are completely arbitrary. (This is clearly due to the nonuniqueness of the potentials in the ungauged approach as discussed in Section 9.1). In the next section, examples from the previous chapters are used for verifying the presented potential schemes and for comparison with the direct method.

## 9.5 Examples

### 9.5.1 Introduction

The same models that were used for the verification of the CSEM scheme in Chapter 7 are used here for testing the presented EM potential scheme. The solutions from these models are also used for studying the inductive and galvanic effects. It is expected that the solutions for the inductive and galvanic parts can be explained by the type of EM source that is being used. As already stated, the potential scheme presented here can be solved by both iterative and direct solvers. Using the second example, a study has been conducted for comparing the efficiency of two standard iterative solvers. Also, the accuracy of the potential scheme is evaluated and compared with the accuracy of the direct method.

### 9.5.2 Example 1: magnetic dipole source

The model in this example is the same as the model used in the first example for the direct EM-field scheme (Section 7.5.2). For the solution of the problem the BiCGStab iterative solver with an ILUT preconditioner was used. $lfil = 3$ and $droptol = 0$ were used for preconditioning and the target tolerance for the residual norm was $10^{-15}$. (There may exist more efficient preconditioning approaches for solving the problems that are considered here but it was not an objective of this thesis to find the best preconditioning approach.)

The scattered magnetic field solutions for this model from the EM potential scheme and for the same frequencies as previously used for the direct scheme are shown in Figures 7.9 and 7.10 (the same grids are also used). Several data-sets are shown in these figures: the measurements performed for physical scale modelling, integral-equation solutions, finite-element solutions, and direct and potential finite-volume solutions. It can be seen in these figures that there is a good agreement between the numerical solutions while there is a discrepancy between these solutions and the actual measurements. This gap is believed to be due to errors in the experiments. Some of the possible sources of these errors are mentioned in Farquharson et al. (2006) which originally published these results. Also, some discrepancy is observed between the FE and FV solutions and the IE results. This gap is, most likely, due to the largeness of the blocks that are used for solving the IE problems.

Using the primary solutions for the scalar and vector potentials, the solutions for electric field and current density are decomposed into inductive and galvanic components. Solutions are found at a horizontal section that passes through the anomalous region at the depth of 25 mm for a single magnetic dipole source located right at the top-centre of the cube at the height of 2 cm above the brine surface (the same section and source location as used for the results shown in Figure 7.11). Results for electric

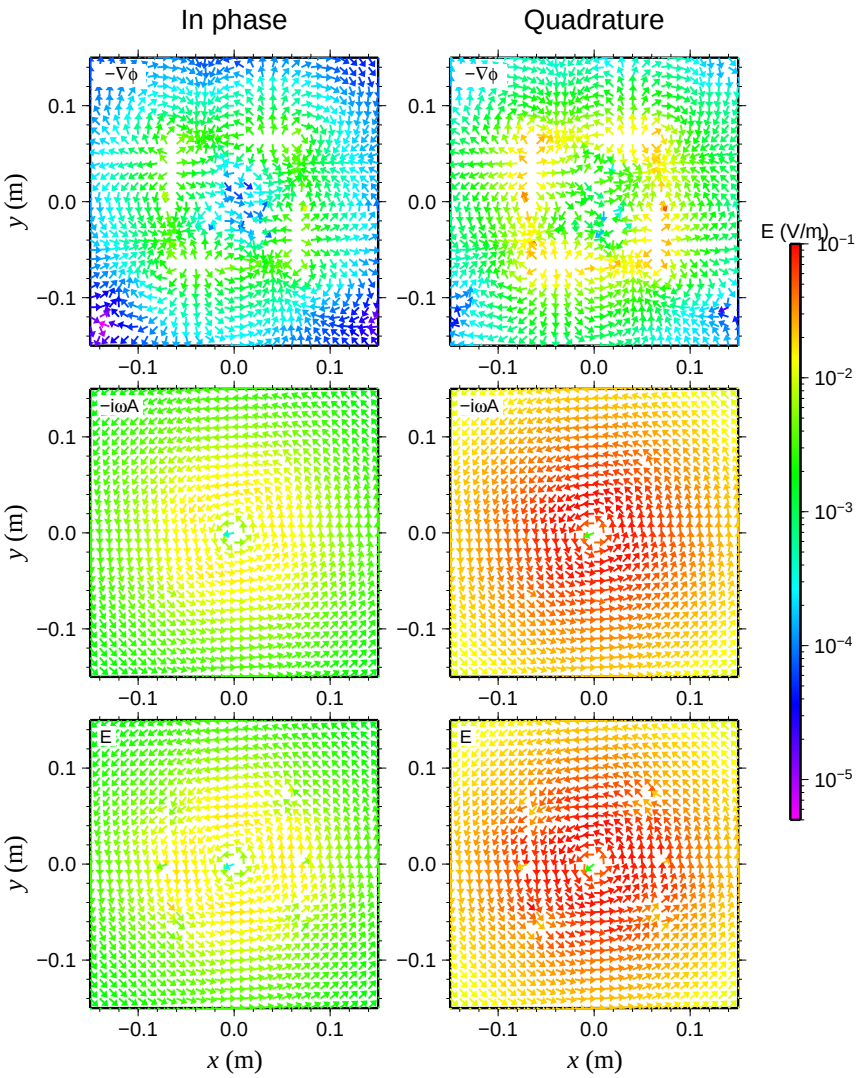


Figure 9.3: Total electric field and its inductive and galvanic parts (from the bottom to the top) for the frequency of 1 kHz at a horizontal section passing through the graphite cube at the depth of 25 mm (the first example for the potential method). For these sections, a single vertical magnetic dipole is located right at the top-centre of the cube at the height of 2 cm above the brine surface.

field and current density and for the frequency of 1 kHz are shown in Figures 9.3 and 9.4, respectively. The decomposition of the fields into inductive and galvanic parts is based on relation 6.20: the galvanic part is $-\nabla\phi$ ($-\sigma\nabla\phi$ for current density) while the inductive part equals $-i\omega A$ ($-i\omega\sigma A$ for current density). It can be readily seen

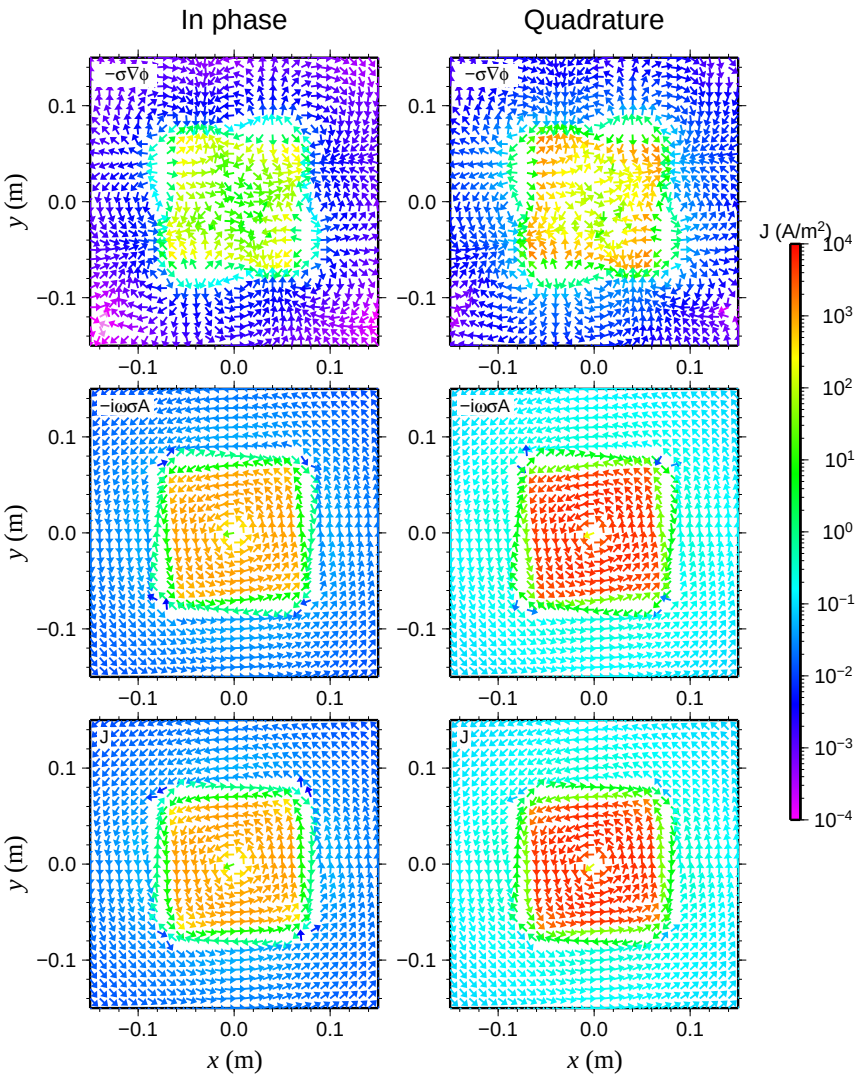


Figure 9.4: Total current density and its inductive and galvanic parts (from the bottom to the top) for the frequency of 1 kHz at a horizontal section passing through the graphite cube at the depth of 25 mm (the first example for the potential method). For these sections, a single vertical magnetic dipole is located right at the top-centre of the cube at the height of 2 cm above the brine surface.

that in both of the figures the total fields are dominated by the inductive parts and the galvanic parts are relatively small. This observation agrees well with the fact that the source that is used is an inductive source (magnetic dipole) which does not inject any charge inside the ground. The galvanic part is not perfectly zero, however, be-

cause there are always regionally induced currents present which can interact with the anomalous region. Additionally, Figures 9.3 and 9.4 show, respectively, the continuity and discontinuity of the tangential components of electric field and current density.

### 9.5.3 Example 2: grounded wire source

The model in this example is also the same as the model used in the second example for the direct EM-field scheme (Section 7.5.3). For the solution of the problem, BiCGStab used 0.8 Gbytes of RAM and 345 s to reach the residual norm of $10^{-12}$ after 2000 iterations (compare this with 4 Gbytes of RAM and 40 s for the direct method with MUMPS). The solutions for this model from the EM potential scheme and for the same frequency as previously used for the direct scheme are shown in Figures 9.5 (for total electric field) and 7.18 (for scattered electric field). While in the former the potential method FV solutions are compared against IE solutions, in the latter several data-sets are shown: IE solutions, FE solutions, and direct method and potential method FV solutions. It can be seen that there is a very good agreement between the FV and FE solutions while there is a discrepancy between these solutions and the IE results. As for the previous example, this gap is due to the large size of the blocks that were used for solving the IE problem.

For this example, also, the solutions for electric field and current density are decomposed into inductive and galvanic components (the same frequency and source are used). Solutions are found at a horizontal section that passes through the anomalous region at the depth of 200 m (the same section is used for the results shown in Figure 7.19). Results for electric field and current density are shown in Figures 9.6 and 9.7, respectively. It can be readily seen that, in contrast to the previous example, the total fields are dominated by the galvanic parts and that the inductive parts are small. This observation also agrees with the fact that the source that is used is a galvanic

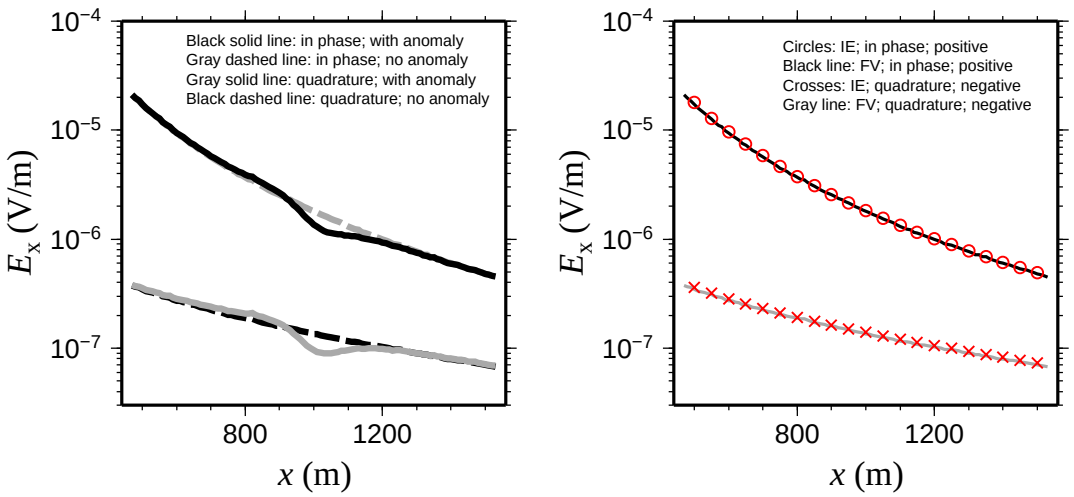


Figure 9.5: The in-phase and quadrature parts of the $x$-component of the total electric field at the observation points for the second example (for the potential scheme) when the anomalous region is present (left panel) and for the homogeneous halfspace (right panel). The solutions are compared with the solutions from an integral-equation code (Farquharson and Oldenburg, 2002).

source (grounded wire) which operates at a low frequency and injects charge into the ground. Here, also, the inductive part is not perfectly zero because there is always some induction occurring in the ground when there is a time-varying magnetic field. An additional observation from Figures 9.6 and 9.7 is the discontinuity and continuity of the normal components of electric field and current density in these figures.

### 9.5.4 Accuracy and resource usage

The same accuracy study as was conducted for the direct method is performed for the EM potential scheme and the results are given in Figure 7.21 (a). This figure shows cumulative error versus the changing cell size at observation points. The same grids as were used for the direct method are used here and no interpolation is involved for finding these solutions (the observation points lie on tetrahedral edges and, therefore, no interpolation is required). It can be seen that while the orders of accuracy of

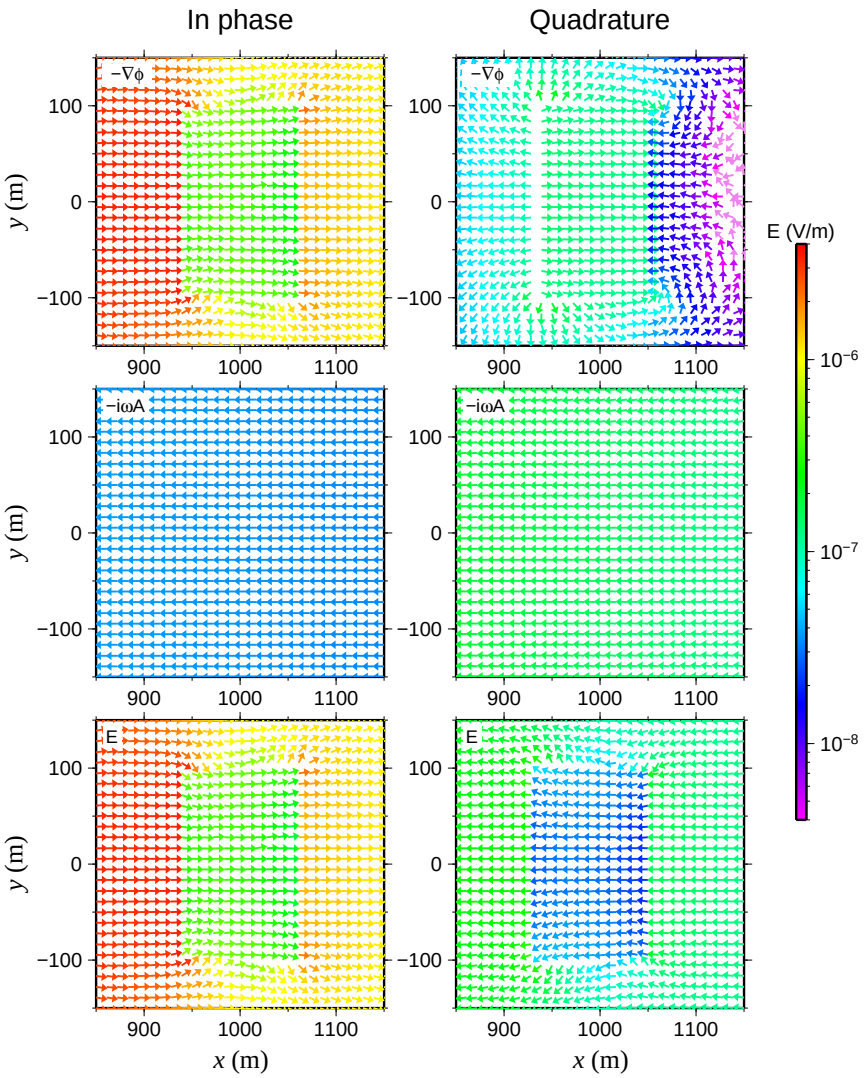


Figure 9.6: Total electric field and its inductive and galvanic parts (from the bottom to the top) for the frequency of 3 Hz at a horizontal section passing through the anomalous prism at the depth of 200 m (the second example for the potential method). The source is a grounded wire which is extended from $(0, 0, 0)$ m to $(0, 0, 100)$ m.

the two methods are similar (between 0.5 and 1), the EM potential method is more accurate than the direct EM-field method (the errors are smaller).

An experiment is also performed in order to compare the MUMPS sparse direct solver and the BiCGStab and GMRES iterative solvers for the solution of the gauged and ungauged potential schemes presented in this chapter (relations 9.18 and

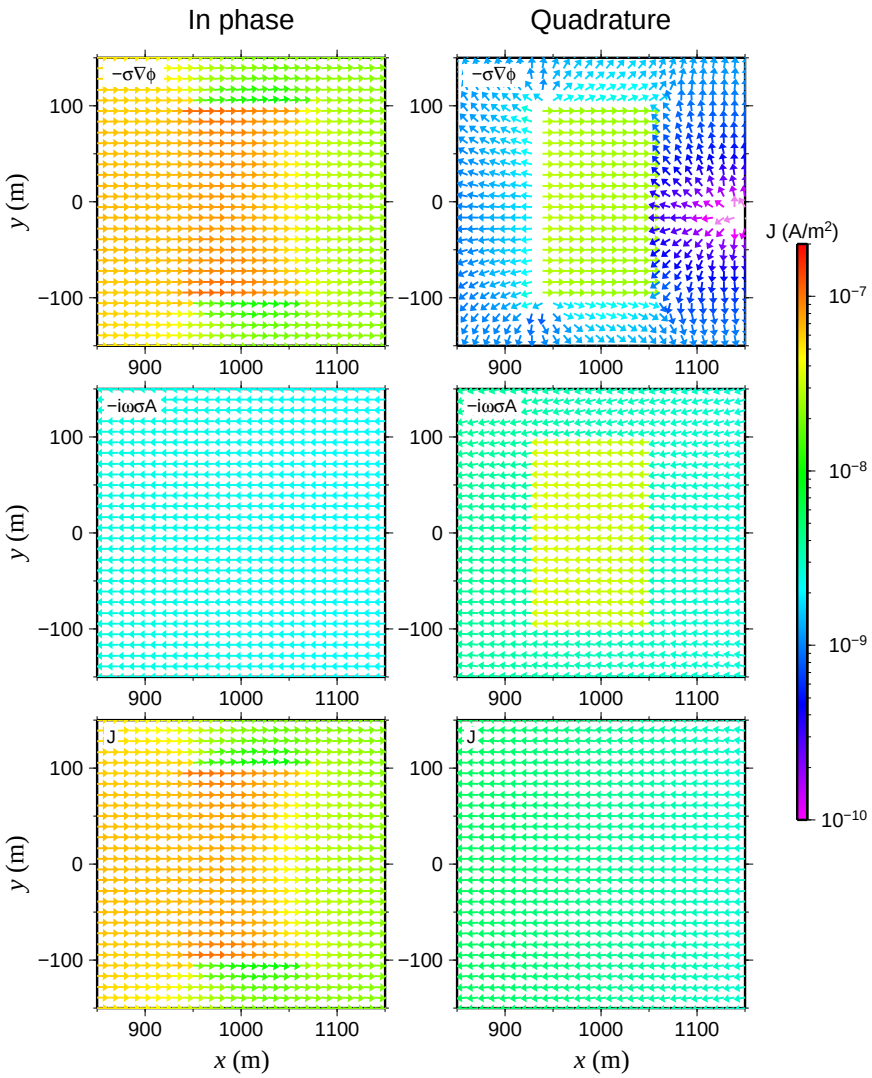


Figure 9.7: Total current density and its inductive and galvanic parts (from the bottom to the top) for the frequency of 3 Hz at a horizontal section passing through the anomalous prism at the depth of 200 m (the second example for the potential method). The source is a grounded wire which is extended from $(0, 0, 0)$ m to $(0, 0, 100)$ m.

9.19, respectively, together with relation 9.21) and the direct scheme from Chapter 7 (relation 7.10). For this experiment, the model from the second example above is used (the model with grounded wire source) and the same operating frequency and observation locations are considered. For the iterative solvers, different values of *lfil*

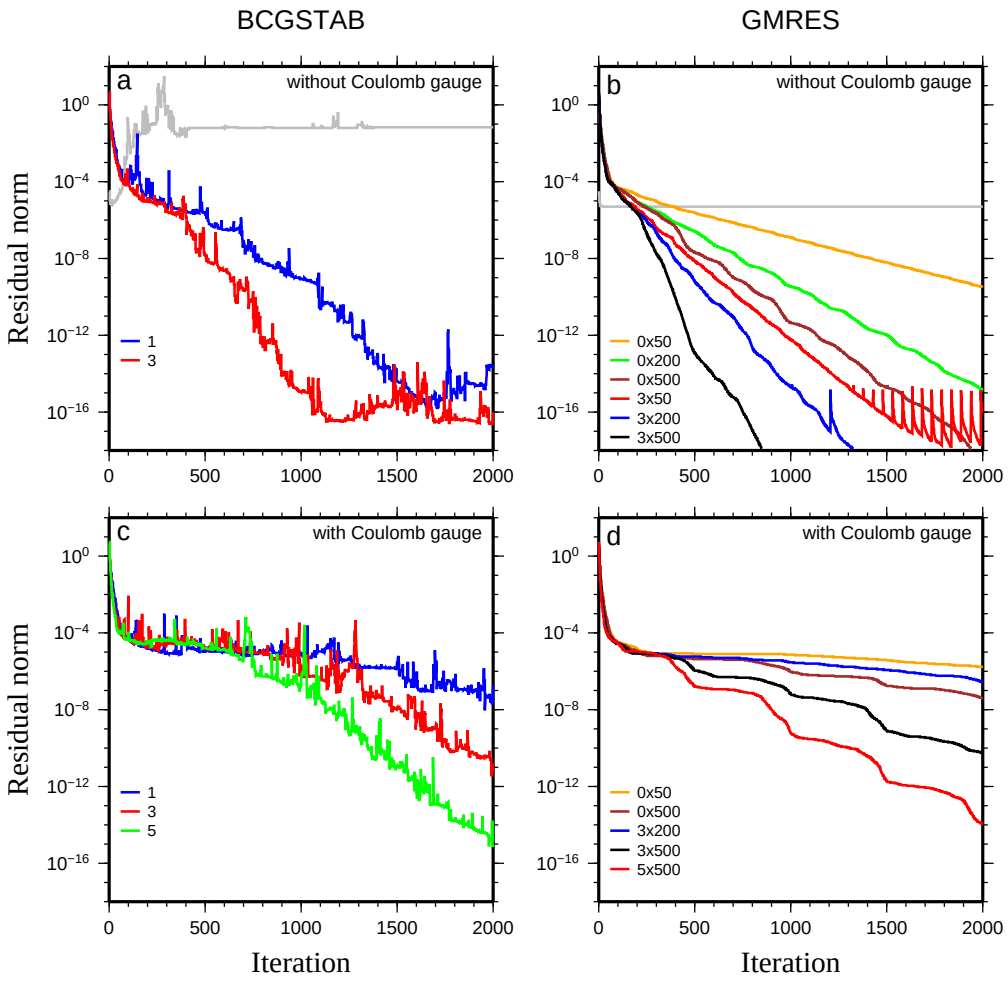


Figure 9.8: Residual-norm versus iterations of GMRES and BiCGStab solvers for the potential schemes (gauged and ungauged) and the direct scheme. Panels (a) and (b) give the results of the solution of the ungauged potential scheme using BiCGStab and GMRES, respectively, and panels (c) and (d) give the results of the solution of the gauged potential scheme using BiCGStab and GMRES, respectively. Additionally, the results for the direct scheme are also shown in panels (a) and (b) by gray lines (for BiCGStab *lfil* was 3 and for GMRES *lfil* and Krylov subspace were 3 and 200, respectively). Results for different gauged and ungauged tests are shown by different colors and their corresponding values of *lfil* and Krylov subspace are given as inlaid legends (*lfil* for BiCGStab and *lfil*×subspace for GMRES).

for the ILUT preconditioner are used. In addition to this parameter, for the GMRES solver different values for the restart parameter (which controls the size of the Krylov subspace) are tested. The convergence of the iterative solvers for each of the exper-

iments is shown in Figure 9.8 using curves that show decrease in the residual-norm with increasing iterations. This figure also shows the results of unsuccessful attempts for solving the direct scheme using the two iterative solvers. Computation time and memory usage for the iterative solvers (for 2000 iterations) and for the direct solver are given in Table 9.1.

The examination of Figure 9.8 and Table 9.1 shows that both of the iterative solvers can solve the problem by reaching sufficiently small residual-norms. As expected, GMRES is more stable than BiCGStab (its residual norm decreases steadily while the residual-norm for BiCGStab is fluctuating). However, GMRES is generally more expensive in terms of time and memory due to the cost of orthogonalization of the Krylov subspace. It can also be seen that the gauged problem is more difficult to solve than the ungauged problem. The figure shows that the direct scheme cannot be easily solved using iterative solvers (the curves do not show any convergence). The solution of the direct scheme using MUMPS is much more expensive than the iterative solution of the potential schemes in terms of memory. However, the direct solution is faster and it can be seen that it is less expensive than the direct solution of the potential schemes (potential schemes with MUMPS) in term of computation time and memory.

## 9.6 Conclusions

This chapter dealt with the solution of the potential formulation of Maxwell's equations using a staggered finite-volume approach on unstructured tetrahedral-Voronoï grids. Compared to the direct EM-field method, the main advantages of the potential method are the better conditioning of the problems, which allows using iterative solvers, and the possibility that this method provides for decomposing the solutions

into galvanic and inductive parts. The latter, which is made feasible by applying a gauge correction, allows studying the physics of galvanic and inductive effects and their relative contributions to the total fields that are observed.

The same grids as were used in the previous chapters were used for the discretization. Scalar and vector potentials were defined, respectively, at tetrahedral nodes and along tetrahedral edges. The problems were solved using both BiCGStab and GMRES iterative solvers and MUMPS sparse direct solver. For verification, the two examples that were previously used for the direct EM-field scheme were employed. The results for these two models (one with magnetic dipole source-receiver pairs and the other one with a grounded wire) were in good agreement with those from the literature and with the results of the direct scheme. For these examples, the solutions were also decomposed into galvanic and inductive parts. The results were in good agreement with the type of the sources that were used. Additionally, accuracy studies were conducted which showed a relatively higher accuracy of the potential scheme compared to the direct scheme.

The schemes were also compared in terms of the efficiency of direct and iterative solvers. The direct EM-field scheme could only be solved using the direct solver (MUMPS) and it was more efficient than the direct solution of the gauged and ungauged potential schemes in terms of memory and computation time (with MUMPS, the ungauged and gauged schemes required, approximately, 1.5 and 3 times as much memory and computation time as the direct EM-field scheme). The potential schemes, however, could be solved using both direct and iterative solvers. The iterative solvers were much more efficient than the direct solver in terms of memory usage but they were not as fast. It suggests that, compared to the direct EM-field method, considerably larger problems can be solved using the potential schemes with iterative solvers. The gauged problems were harder to solve than the ungauged problems: the ungauged

problems could be solved without preconditioning while the gauged problems required at least some preconditioning which resulted in increases in the computation time and memory usage. Therefore, the choice of a numerical scheme is dependent upon the type of solution and the type of solver that are desirable: while the direct EM-field method is more efficient with the direct solvers, the iterative solvers are better suited for the ungauged potential scheme, and it is only the gauged potential scheme which can be used for separating the inductive and galvanic parts of the solutions.

Table 9.1: Computation time and memory usage for the solution of a problem with GMRES and BiCGStab iterative solvers (shown in Figure 9.8) and with MUMPS direct solver. EM potential schemes (gauged and ungauged) and the direct EM-field scheme are solved using the mentioned solvers for this problem. Different values of *lfil* and Krylov subspace are given for the experiments with the iterative solvers.

| Numerical scheme | Solver | lfil | Krylov subspace | Computation time (s) | Memory (Gbytes) |
|---|---|---|---|---|---|
| A-$\phi$ method ungauged | BiCGStab | 1 | - | 157 | 0.5 |
| | ” | 3 | - | 250 | 0.5 |
| | GMRES | 0 | 50 | 383 | 0.6 |
| | ” | 0 | 200 | 1027 | 1.1 |
| | ” | 0 | 500 | 2220 | 2.1 |
| | ” | 3 | 50 | 494 | 0.7 |
| | ” | 3 | 200 | 740 | 1.1 |
| | ” | 3 | 500 | 948 | 2.1 |
| | MUMPS | - | - | 78 | 6.1 |
| A-$\phi$ method gauged | BiCGStab | 1 | - | 259 | 0.7 |
| | ” | 3 | - | 345 | 0.8 |
| | ” | 5 | - | 3737 | 0.9 |
| | GMRES | 0 | 50 | 472 | 0.9 |
| | ” | 0 | 500 | 2421 | 2.4 |
| | ” | 3 | 200 | 1210 | 1.4 |
| | ” | 3 | 500 | 2509 | 2.4 |
| | ” | 5 | 500 | 5917 | 2.5 |
| | MUMPS | - | - | 141 | 11.8 |
| E-field method | MUMPS | - | - | 40 | 4 |

# Chapter 10

# Summary

This thesis investigated the application of unstructured grids for the forward modelling of geophysical potential field data and electromagnetic data. Due to the similarity between the governing equations of the gravitational field and the magnetic field (which constitute potential field theory), for the forward modelling of potential field data only the modelling of gravity data was considered. The main goal was to develop finite-element and finite-volume forward schemes which can be later used as forward solvers inside gradient-based inversion programs. These schemes were based on unstructured tetrahedral grids and their dual Voronoï grids.

Unstructured grids provide the flexibility that is required for the efficient modelling of geological interfaces and topographical features. They also allow local refinement which can be used for refining the grids in places where high curvature of the fields is present such as at electromagnetic sources or at the interface between regions with high contrast of physical properties, or where high precisions are required, such as at the observation points.

The numerical methods that were derived and investigated were finite-element and finite-volume methods. Both of these methods were employed for the forward

modelling of gravity data but for the modelling of electromagnetic data only the finite-volume method was used. Unstructured tetrahedral and Voronoï grids were separately used for the modelling of gravity data while the grid that was used for the modelling of electromagnetic data was a staggered tetrahedral-Voronoï grid.

The first half of this thesis dealt with the forward modelling of gravity data using finite-element and finite-volume methods. Tetrahedral grids were used for the finite-element method and linear and quadratic schemes were developed. In the linear method, the solutions were found at the nodes of the grid (i.e., the vertices of the tetrahedra) and in the quadratic method they were found at the nodes and at the midpoints of the edges. For the finite-volume method, both the tetrahedral and Voronoï grids were used for developing cell-centred and vertex-centred schemes, respectively. In the cell-centred method, the solutions were found at the circumcentres of the tetrahedra while in the vertex-centred scheme the problem was solved for the unknowns at the vertices of the tetrahedra. The direct solution from the forward problem was the gravitational potential and, therefore, post-processing stages were required for finding the vertical derivative of this potential which is the gravitational attraction. For deriving the gravity at the observation points, a differencing scheme was used for the finite-volume approaches and interpolation functions were used for the finite-element schemes.

Several simple and realistic models were used for verifying the four numerical schemes. The simple models were also used for accuracy studies and for evaluating the methods in terms of computation resources (i.e., the computation time and memory usage). The quadratic finite-element scheme was found to be the most accurate but at the same time the most expensive method. The cell-centred finite-volume scheme was more expensive than the two remaining methods while not offering a considerably higher accuracy. The best trade-offs between accuracy and computational

resource requirement were achieved by the linear finite-element and vertex-centred finite-volume schemes. Additionally, the applicability of the schemes to real-life geological models was demonstrated by modelling borehole gravity data due to the Ovoid ore body at Voisey's Bay, Labrador, Canada.

The second half of this thesis dealt with the modelling of electromagnetic data. Two schemes were developed based on the direct EM-field formulation and EM potential formulation of Maxwell's equations. These schemes were generalizations of the well-known Yee method. Instead of the staggered rectilinear grid that is used in the Yee method, here, a staggered tetrahedral-Voronoï grid was employed. In the direct method, the Helmholtz equation for the electric field in the frequency domain was solved and the solutions were found at the tetrahedral edges. In the potential method, the Helmholtz equation for the scalar and vector potentials and the relation of conservation of charge were solved. The solution at any point inside the grid was then calculated using the edge vector interpolation functions of the tetrahedral edges. The schemes were adapted for a variety of electromagnetic sources in order to simulate both controlled-source and magnetotelluric data.

For the verification of the schemes, several benchmark models were used for which solutions from other numerical methods were available. These models represented different electromagnetic survey scenarios. The first one corresponded to air-borne surveys where the source and receiver are towed along a profile and above the ground. There was a large conductivity contrast between the anomalous region and the background, the source was a vertical magnetic dipole and relatively high frequencies were employed. For this example, the solution was the secondary magnetic field and it was compared with finite-element and integral-equation results and with physical scale modelling measurements.

The second example represented a typical land survey in which the source was a

long grounded wire, the anomalous body was far away from the source, there was a small conductivity contrast, and a low frequency was used. The total and secondary electric fields were computed for this example and the solutions were compared with integral-equation and finite-element solutions. For this model, accuracy studies were conducted in order to better understand the relative importance of the different refinements in the grid. The results showed that the most important locations are the observation locations around which the grid should be highly refined. The main factor affecting the accuracy of the solutions was found to be the uniformity of the grid at the observation locations and at the region around these points. This can be controlled, to a great extent, by generating high-quality grids. The accuracy studies also showed the relatively higher accuracy of the potential scheme.

The Ovoid model which was used for the modelling of gravity data was also used for the simulation of helicopter-borne magnetic data with the direct scheme. The source-receiver setting was similar to the first example and the secondary magnetic field was compared with the real data. Although the match was not exact, there was a good agreement between the finite-volume and real field data.

In addition to the controlled-source application, the direct EM-field scheme was also adapted for modelling magnetotelluric data. A different boundary condition was used in order to simulate the natural plane wave source that is considered in this method. For this scheme, two benchmark COMMEMI models were used and the solutions for apparent resistivity and phase were compared with those from the literature. All the comparisons showed good agreements between the solutions and the reference data which confirmed the accuracy of the finite-volume scheme.

In addition to the examples which were used for verification, the potential scheme was also used for studying the inductive and galvanic components of the electric field and current density. As these two parts correspond to the scalar and vector potentials,

a Coulomb gauge was considered in order to guarantee the uniqueness of the solutions for these potentials. The potential scheme is better-conditioned than the direct EM-field scheme and it was possible to solve the potential problems with iterative solvers. A study was performed to compare two standard iterative solvers and a sparse direct solver for the solution of the gauged and ungauged potential schemes and the direct EM-field scheme. The results showed the better performance of the direct EM-field scheme with the direct solver and the higher efficiency of the potential schemes with the iterative solvers. The iterative solvers were not as fast as the direct solver but they were considerably more efficient in terms of memory usage.

Several topics can be considered for future work following the research presented in this thesis. The first natural option is developing inversion programs based on the numerical forward solvers that are presented here. Conjugate gradient optimization techniques can be employed in these inversions in order to take advantage of the sparsity of the matrices that are involved. Also, the EM forward solvers can be generalized to include anisotropic media so that quantities like conductivity, magnetic permeability, and electric permittivity can be represented as tensors rather than scalars. In this thesis, the quasi-static regime was considered which is a good approximation for low-frequency geophysical methods. A further step can be the solution of governing equations for the non-quasi-static case where displacement current in the earth is not ignored. High-frequency electromagnetic data, like GPR data, can be modelled in this way. Finally, adaptive mesh refinement algorithms can be used for both gravity and EM solvers. In this thesis, the devised mesh refinements were mainly based on experiments and intuition. However, there are algorithms available that can control the amounts of refinement and coarsening that are necessary in the grid in order to reduce the numerical error, and hence optimizing the unstructured grids generation process.

# Bibliography

Amestoy, P. R., A. Guermouche, J.-Y. L'Excellent, and S. Pralet, 2006, Hybrid scheduling for the parallel solution of linear systems: Parallel Computing, **32**, 136–156.

Ansari, S. M., and C. G. Farquharson, 2014, 3D finite-element forward modeling of electromagnetic data using vector and scalar potentials and unstructured grids: Geophysics, **79**, 1–17.

Aruliah, D., U. Ascher, E. Haber, and D. W. Oldenburg, 2001, A method for the forward modelling of 3D electromagnetic quasi-static problems: Mathematical Models and Methods in Applied Sciences, **11**, 1–21.

Badea, E. A., M. E. Everett, G. A. Newman, and O. Biro, 2001, Finite-element analysis of controlled-source electromagnetic induction using Coulomb-gauged potentials: Geophysics, **66**, 786–799.

Balch, S. J., 2000, Geophysics in Mineral Exploration: Fundamentals and Case Histories. Ni-Cu Sulphide Deposits with examples from Voisey's Bay, *in* Practical Geophysics III: Northwest Mining Association.

Barbosa, V. C. F., J. B. C. Silva, and W. E. Medeiros, 1997, Gravity inversion of basement relief using approximate equality constraints on depths: Geophysics, **62**, 1745–1757.

Barnett, C. T., 1976, Theoretical modeling of the magnetic and gravitational fields of

an arbitrarily shaped three-dimensional body: Geophysics, **41**, 1353–1364.

Biro, O., and K. Preis, 1989, On the use of the magnetic vector potential in the finite element analysis of three-dimensional eddy currents: IEEE Transactions on Magnetics, **25**, 3145–3159.

Blakely, R. J., 1996, Potential Theory in Gravity and Magnetic Applications: Cambridge University Press.

Börner, R. U., 2010, Numerical Modelling in Geo-Electromagnetics: Advances and Challenges: Surveys in Geophysics, **31**, 225–245.

Börner, R. U., G. O. Ernst, and K. Spitzer, 2008, Fast 3-D simulation of transient electromagnetic fields by model reduction in the frequency domain using Krylov subspace projection: Geophysical Journal International, **173**, 766–780.

Cagniard, L., 1953, Basic theory of the magneto-telluric method of geophysical prospecting: Geophysics, **18**, 605–635.

Cai, Y., and C.-Y. Wang, 2005, Fast finite-element calculation of gravity anomaly in complex geological regions: Geophysical Journal International, **162**, 696–708.

Chasseriau, P., and M. Chouteau, 2003, 3d gravity inversion using a model of parameter covariance: Journal of Applied Geophysics, **52**, 59–74.

Commer, M., and G. A. Newman, 2004, A parallel finite-difference approach for 3-D transient electromagnetic modeling with galvanic sources: Geophysics, **69**, 1192–1202.

Druskin, V., L. Knizhnerman, and P. Lee, 1999, A new spectral lanczos decomposition method for induction modeling in arbitrary 3-d geometry: Geophysics, **64**, 701–706.

Du, Q., and D. Wang, 2006, Recent progress in robust and quality Delaunay mesh generation: Journal of Computational and Applied Mathematics, **195**, 8–23.

Everett, M. E., and M. A. Meju, 2005, Near-surface controlled-source electromagnetic induction: Background and recent advances, *in* Hydrogeophysics: Springer, 157–

183.

Eymard, R., T. Gallouët, and R. Herbin, 2000, Finite Volume Methods, *in* Handbook of Numerical Analysis: Elsevier, 713–1018.

Farquharson, C. G., 2008, Constructing piecewise-constant models in multidimensional minimum-structure inversions: Geophysics, **73**, K1–K9.

Farquharson, C. G., K. Duckworth, and D. W. Oldenburg, 2006, Comparison of integral equation and physical scale modeling of the electromagnetic responses of models with large conductivity contrasts: Geophysics, **71**, G169–G177.

Farquharson, C. G., and M. P. Miensopust, 2011, Three-dimensional finite-element modelling of magnetotelluric data with a divergence correction: Journal of Applied Geophysics, **75**, 699–710.

Farquharson, C. G., and C. R. W. Mosher, 2009, Three-dimensional modelling of gravity data using finite differences: Journal of Applied Geophysics, **68**, 417–422.

Farquharson, C. G., and D. W. Oldenburg, 2002, An integral-equation solution to the geophysical electromagnetic forward-modelling problem, *in* Three-Dimensional Electromagnetics: Proceedings of the Second International Symposium: Elsevier.

Fašková, Z., R. Čunderlík, and K. Mikula, 2010, Finite element method for solving geodetic boundary value problems: Journal of Geodesy, **84**, 135–144.

Fomenko, E. Y., and T. Mogi, 2002, A New Computation Method for a Staggered Grid of 3-D EM Field Conservative Modeling: Earth, Planets and Space, **54**, 499–509.

Francke, J., 2012, A review of selected ground penetrating radar applications to mineral resource evaluations: Journal of Applied Geophysics, **81**, 29–37.

Franke-Börner, A., 2013, Three-dimensional Finite Element Simulation of Magnetotelluric Fields on Unstructured Grids: PhD thesis, TU Bergakademie Freiberg.

Frischknecht, F. C., V. F. Labson, B. R. Spies, and W. L. Anderson, 1987, Profiling methods using small sources, *in* Electromagnetic Methods in Applied Geophysics,

Volume 2: Society of Exploration Geophysicists, 105–270.

Garrie, D. G., 1995, Dighem survey for diamond fields resources Inc. Archean resources Ltd. Voisey's Bay, Labrador: Survey Report 1202, Dighem, A division of CGG Canada Ltd.

Grant, F. S., and G. F. West, 1965, Interpretation Theory in Applied Geophysics: McGraw-Hill Book Co.

Grayver, A., and R. Streich, 2012, Comparison of iterative and direct solvers for 3D CSEM modeling: Presented at the SEG Annual Meeting, Las Vegas.

Griffiths, D. J., 1999, Introduction to Electrodynamics, third edition: Prentice-Hall inc.

Haber, E., 2002, 3D forward modeling of time domain electromagnetic data: Presented at the 72nd Annual International Meeting, SEG.

Haber, E., U. M. Ascher, D. A. Aruliah, and D. W. Oldenburg, 2000, Fast Simulation of 3D Electromagnetic Problems Using Potentials: Journal of Computational Physics, **163**, 150–171.

Hermeline, F., 1993, Two Coupled Particle-Finite Volume Methods Using Delaunay-Voronoï Meshes for the Approximation of Vlasov-Poisson and Vlasov-Maxwell Equations: Journal of Computational Physics, **106**, 1–18.

Hermeline, F., 2009, A finite volume method for approximating 3D diffusion operators on general meshes: Journal of Computational Physics, **288**, 5763–5786.

Hermeline, F., S. Layouni, and P. Omnes, 2008, A finite volume method for the approximation of Maxwell's equations in two space dimensions on arbitrary meshes: Journal of Computational Physics, **227**, 9365–9388.

Hirsch, C., 2007, Numerical Computation of Internal and External Flows: The Fundamentals of Computational Fluid Dynamics (2nd ed.): Elsevier, Butterworth-Heinemann.

Hjelt, S. E., 1974, The gravity anomaly of a dipping prism: Geoexploration, **12**, 29–39.

Hohmann, G. W., 1983, Three-dimensional EM modeling: Geophysical Surveys, **6**, 27–53.

Horesh, L., and E. Haber, 2011, A Second Order Discretization of Maxwell's Equations in the Quasi-Static Regime on OcTree Grids: SIAM Journal on Scientific Computing, **33**, 2805–2822.

Hou, J., R. K. Mallan, and C. Torres-Verdín, 2006, Finite-difference simulation of borehole EM measurements in 3D anisotropic media using coupled scalar-vector potentials: Geophysics, **71**, G225–G233.

Inan, U. S., and R. A. Marshall, 2011, Numerical Electromagnetics: The FDTD Method: Cambridge University Press.

Jin, J., 2002, The Finite Element Method in Electromagnetics, 2nd. ed.: John Wiley & Sons Inc., New York.

Kellogg, O. D., 1967, Foundations of Potential Theory: Springer-Verlag.

Key, K., and J. Ovall, 2011, A parallel goal-oriented adaptive finite element method for 2.5-D electromagnetic modelling: Geophysical Journal International, **186**, 137–154.

Key, K., and C. Weiss, 2006, Adaptive finite-element modeling using unstructured grids: The 2D magnetotelluric example: Geophysics, **71**, G291–G299.

LaBrecque, D. J., 1999, Finite difference modeling of 3-D EM fields with scalar and vector potentials, *in* Three Dimensional Electromagnetics. Geophysical Developments Series 7: Society of Exploration Geophysicists, 146–160.

Lajoie, J. J., and G. F. West, 1976, The electromagnetic response of a conductive inhomogeneity in a layered earth: Geophysics, **41**, 1133–1156.

Lelièvre, P., A. Carter-McAuslan, C. G. Farquharson, and C. Hurich, 2012, Unified

geophysical and geological 3D Earth models: The Leading Edge, **31**, 322–328.

Li, X., and M. Chouteau, 1998, Three-dimensional gravity modeling in all space: Surveys in Geophysics, **19**, 339–368.

Li, Y., and K. Key, 2007, 2D marine controlled-source electromagnetic modeling: Part 1 - An adaptive finite element algorithm: Geophysics, **72**, WA51–WA62.

Li, Y., and D. W. Oldenburg, 1996, 3-d inversion of magnetic data: Geophysics, **61**, 394–408.

Li, Y., and D. W. Oldenburg, 1998, 3-d inversion of gravity data: Geophysics, **63**, 109–119.

Li, Y., and D. W. Oldenburg, 2003, Fast inversion of large-scale magnetic data using wavelet transforms and a logarithmic barrier method: Geopysical Jouranal Internatinal, **152**, 251–265.

Liu, C., Z. R. amd J. Tan, and Y. Yan, 2008, Three-dimensional magnetotellurics modeling using edge-based finite-element unstructured meshes: Applied Geophysics, **5**, 170–180.

Lowry, T., M. B. Allen, and P. N. Shive, 1989, Singularity removal; A refinement of resistivity modeling techniques: Geophysics, **56**, 766–774.

Maaø, F., 2007, Fast finite-difference time-domain modeling for marine-subsurface electromagnetic problems: Geophysics, **72**, A19–A23.

Mackie, R. L., and T. R. Madden, 1993, Three-dimensional magnetotelluric inversion using conjugate gradients: Geopysical Jouranal Internatinal, **115**, 215–229.

Mackie, R. L., T. R. Madden, and P. Wannamaker, 1993, 3-D Magnetotelluric Modeling Using Difference Equations - Theory and Comparisons to Integral Equation Solutions: Geophysics, **58**, 215–226.

Madden, T. R., and R. L. Mackie, 1989, Three-Dimensional Magnetotelluric Modeling and Inversion: Proceedings of the IEEE, **77**, 318–333.

Madsen, N. K., and R. W. Ziolkowski, 1990, A three-dimensional modified finite volume technique for Maxwell's equations: Electromagnetics, **10**, 147–161.

May, D. A., and M. G. Knepley, 2011, Optimal, scalable forward models for computing gravity anomalies: Geopysical Jouranal Internatinal, **187**, 161–177.

Mitsuhata, Y., 2000, 2-D electromagnetic modeling by finite-element method with a dipole source and topography: Geophysics, **65**, 465–475.

Mitsuhata, Y., and T. Uchida, 2004, 3D magnetotelluric modeling using the T-Ω finite-element method: Geophysics, **69**, 108–119.

Mogi, T., 1996, Three-dimensional electromagnetic modeling of magnetotelluric data using finite element method: Journal of Applied Geophysics, **35**, 185–189.

Morisue, T., 1993, A comparison of the Coulomb gauge and Lorentz gauge magnetic vector potential formulations for 3-D eddy current calculations: IEEE Transactions on Magnetics, **29**, 1372–1375.

Mulder, W. A., 2008, Geophysical modelling of 3D electromagnetic diffusion with multigrid: Computing and Visualization in Science, **11**, 129–138.

Nabighian, M. N., M. E. Ander, V. J. S. Grauch, R. O. Hansen, T. R. LaFehr, Y. Li, W. C. Pearson, J. W. Peirce, J. D. Phillips, and M. E. Ruder, 2005a, Historical development of the gravity method in exploration: Geophysics, **70**, 63ND–89ND.

Nabighian, M. N., V. J. S. Grauch, R. O. Hansen, T. R. LaFehr, Y. Li, J. W. Peirce, J. D. Phillips, and M. E. Ruder, 2005b, The historical development of the magnetic method in exploration: Geophysics, **70**, 33ND–61ND.

Nagy, D., 1966, The gravitational attraction of a right rectangular prism: Geophysics, **31**, 362–371.

Newman, G. A., and D. L. Alumbaugh, 1995, Frequency-Domain Modeling of Airborne Electromagnetic Responses Using Staggered Finite Differences: Geophysical Prospecting, **43**, 1021–1042.

Newman, G. A., and D. L. Alumbaugh, 2000, Three-dimensional magnetotelluric inversion using non-linear conjugate gradients: Geophysical Journal International, **140**, 410–424.

Newman, G. A., and D. L. Alumbaugh, 2002, Three-dimensional induction logging problems, part 2: A finite-difference solution: Geophysics, **67**, 484–491.

Nicolaides, R. A., and D. Q. Wang, 1998, Convergence analysis of covolume scheme for Maxwell's equations in three dimensions: Mathematics of Computation, **67**, 947–963.

Novo, M. S., L. C. da Silva, and F. L. Teixeira, 2007, Finite Volume Modeling of Borehole Electromagnetic Logging in 3-D Anisotropic Formations Using Coupled Scalar-Vector Potentials: IEEE Antennas and Wireless Propagation Letters, **6**, 549–552.

Okabe, M., 1979, Analytical expressions for gravity anomalies due to homogeneous polyhedral bodies and translations into magnetic anomalies: Geophysics, **44**, 730–741.

Oldenburg, D. W., E. Haber, and R. Shekhtman, 2013, Three dimensional inversion of multisource time domain electromagnetic data: Geophysics, **78**, E47–E57.

Operto, S., J. Virieux, P. Amestoy, J.-Y. L'Excellent, L. Giraud, and H. Ben Hadj Ali, 2007, 3D finite-difference frequency-domain modeling of visco-acoustic wave propagation using a massively parallel direct solver: A feasibility study: Geophysics, **72**, SM195–SM211.

Palacky, G. J., 1987, Resistivity Characteristics of Geologic Targets, *in* Electromagnetic Methods in Applied Geophysics, Volume 1: Society of Exploration Geophysicists, 53–129.

Palacky, G. J., and G. F. West, 1987, Airborne electromagnetic methods, *in* Electromagnetic Methods in Applied Geophysics, Volume 2: Society of Exploration

Geophysicists, 811–879.

Pilkington, M., 2009, 3d magnetic data-space inversion with sparseness constraints: Geophysics, **74**, L7–L15.

Puzyrev, V., J. Koldan, J. de la Puente, G. Houzeaux, M. Vázquez, and J. M. Cela, 2013, A parallel finite-element method for three-dimensional controlled-source electromagnetic forward modelling: Geophysical Journal International, **193**, 678–693.

Reddy, J. N., 2006, An Introduction to the Finite Element Method, 3rd ed.: McGraw-Hill.

Remaki, M., 2000, A new finite volume scheme for solving Maxwell's system: COMPEL., **19**, 913–931.

Rodi, W., and R. L. Mackie, 2001, Nonlinear conjugate gradients algorithm for 2-d magnetotelluric inversion: Geophysics, **66**, 174–187.

Saad, Y., 1990, SPARSKIT: a basic tool kit for sparse matrix computations: Report RIACS 90-20, Research Institute for Advanced Computer Science. NASA Ames Research Center.

Sadiku, M. N. O., 2000, Numerical Techniques in Electromagnetics, 2nd ed.: CRC Press.

Sazonov, I., O. Hassan, K. Morgan, and N. P. Weatherill, 2006, Yee's scheme for the integration of Maxwell's equation on unstructured meshes, *in* Proceedings of the European Conference on Computational Fluid Dynamics.

Sazonov, I., O. Hassan, K. Morgan, and N. P. Weatherill, 2007, Generating the Voronoï-Delaunay Dual Diagram for Co-Volume Integration Schemes, *in* Proceedings of the 4th International Symposium on Voronoi Diagrams in Science and Engineering.

Schroeder, W., and I. Wolff, 1994, The origin of spurious modes in numerical solutions of electromagnetic field eigenvalue problems: IEEE Transactions on Microwave

Theory and Techniques, **42**, 644–653.

Schwarzbach, C., R. U. Börner, and K. Spitzer, 2011, Three-dimensional adaptive higher order finite element simulation for geo-electromagnetics–a marine CSEM example: Geophysical Journal International, **187**, 63–74.

Schwarzbach, C., and E. Haber, 2013, Finite element based inversion for time-harmonic electromagnetic problems: Geophysical Journal International, **193**, 615–634.

Shankar, V., A. H. Mohammadian, and W. F. Hall, 1990, A time-domain finite-volume treatment for the Maxwell equations: Electromagnetics, **10**, 127–145.

Si, H., 2004, TetGen, a quality tetrahedral mesh generator and three-dimensional delaunay triangulator, v1.3: Technical Report 9, Weierstrass Institute for Applied Analysis and Stochastics.

Siripunvaraporn, W., G. Egbert, and Y. Lenbury, 2002, Numerical accuracy of magnetotelluric modeling: a comparison of finite difference approximations: Earth, Planets and Space, **54**, 721–725.

Smith, J. T., 1996, Conservative modeling of 3-D electromagnetic fields, Part 1: Properties and error analysis: Geophysics, **61**, 1308–1318.

Smith, J. T., and J. R. Booker, 1991, Rapid Inversion of Two- and Three-Dimensional Magnetotelluric Data: Journal of Geophysical Research, **96**, 3905–3922.

Stratton, J. A., 1941, Electromagnetic Theory: McGraw-Hill.

Streich, R., C. Schwarzbach, M. Becken, and K. Spitzer, 2010, Controlled-source electromagnetic modeling studies: utility of auxiliary potentials for low frequency stabilization: Presented at the EAGE 72nd Annual International Conference and Exhibition.

Taflove, A., 2000, Computational Electrodynamics: The Finite-Difference Time-Domain Method, 2nd Edition: Artech House, Inc., New York.

Talwani, M., and M. Ewing, 1960, Rapid computation of gravitational attraction of three-dimensional bodies of arbitrary shape: Geophysics, **25**, 203–225.

Tikhonov, A. N., 1950, On the determination of electrical characteristics of deep layers of the Earth's crust (in russian): Doklady, **73**, 295–297.

Ting, S. C., and G. W. Hohmann, 1981, Integral equation modeling of three-dimensional magnetotelluric response: Geophysics, **46**, 182–197.

Um, E., M. Commer, and G. A. Newman, 2013, Efficient pre-conditioned iterative solution strategies for the electromagnetic diffusion in the earth: finite-element frequency-domain approach: Geophysical Journal International, **193**, 1460–1473.

Um, E. S., D. L. Alumbaugh, J. M. Harris, and J. Chen, 2012a, Numerical modeling analysis of short-offset electric-field measurements with a vertical electric dipole source in complex offshore environments: Geophysics, **77**, E329–E341.

Um, E. S., J. M. Harris, and D. L. Alumbaugh, 2010, 3D time-domain simulation of electromagnetic diffusion phenomena: A finite-element electric-field approach: Geophysics, **75**, F115–F126.

Um, E. S., J. M. Harris, and D. L. Alumbaugh, 2012b, An iterative finite element time-domain method for simulating three-dimensional electromagnetic diffusion in earth: Geophysical Journal International, **190**, 871–886.

Vozoff, K., 1991, The magnetotelluric method, *in* Electromagnetic Methods in Applied Geophysics, Volume 2: Society of Exploration Geophysicists, 641–711.

Waldvogel, J., 1976, The Newtonian Potential of a Homogeneous Cube: Journal of Applied Mathematics and Physics (ZAMP), **27**, 867–871.

Walker, P. W., and G. F. West, 1991, A robust integral equation solution for electromagnetic scattering by a thin plate in conductive media: Geophysics, **56**, 1140–1152.

Wang, T., and G. W. Hohmann, 1993, A finite-difference time-domain solution for

three-dimensional electromagnetic modelling: Geophysics, **58**, 797–809.

Wannamaker, P. E., 1991, Advances in three-dimensional magnetotelluric modeling using integral equations: Geophysics, **56**, 1716–1728.

Wannamaker, P. E., G. W. Hohmann, and S. H. Ward, 1984, Magnetotelluric responses of three-dimensional bodies in layered earths: Geophysics, **49**, 1517–1533.

Ward, S. M., and G. W. Hohmann, 1988, Electromagnetic Theory for Geophysical Applications, *in* Electromagnetic Methods in Applied Geophysics, Volume 1, Theory: Society of Exploration Geophysicists, 131–308.

Weaver, J. T., 1994, Mathematical Methods for Geo-Electromagnetic Induction: Research Studies Press Ltd. and John Wiley & Sons Inc.

Weidelt, P., 1999, 3-D Conductivity Models: Implications of Electrical Anisotropy, *in* Three Dimensional Electromagnetics. Geophysical Developments Series 7: Society of Exploration Geophysicists, 119–137.

Weiss, C. J., 2010, Triangulated finite difference methods for global-scale electromagnetic induction simulations of whole mantle electrical heterogeneity: Geochemistry, Geophysics, Geosystems, **11**, 1–15.

Weiss, C. J., 2013, Project APhiD: A Lorenz-gauged A-$\phi$ decomposition for parallelized computation of ultra-broadband electromagnetic induction in a fully heterogeneous Earth: Computers & Geosciences, **58**, 40–52.

Weiss, C. J., 2014, An overset grid method for global geomagnetic induction: Geophysical Journal International, **199**, 1–17.

Weiss, C. J., and G. A. Newman, 2002, Electromagnetic Induction in a Fully 3-D Anisotropic Earth: Geophysics, **67**, 1104–1114.

Weiss, C. J., and G. A. Newman, 2003, Electromagnetic Induction in a Fully 3-D Anisotropic Earth, Part 2: The LIN Preconditioner: Geophysics, **68**, 922–930.

West, G. F., and J. C. Macnae, 1987, Physics of the electromagnetic exploration

method, *in* Electromagnetic Methods in Applied Geophysics, Volume 2: Society of Exploration Geophysicists, 5–45.

Wong, S. H., and Z. J. Cendes, 1988, Combined finite-modal solution of three-dimensional eddy current problems: IEEE Transactions on Magnetics, **24**, 2685–2687.

Xie, Z. Q., O. Hassan, and K. Morgan, 2011, Tailoring unstructured meshes for use with a 3D time domain co-volume algorithm for computational electromagnetics: International Journal for Numerical Methods in Engineering, **87**, 48–65.

Yee, K. S., 1966, Numerical solution of initial boundary problems involving Maxwell's equations in isotropic media: IEEE Transactions on Antennas and Propagation, **14**, 302–309.

Yee, K. S., and J. S. Chen, 1994, Conformal hybrid finite difference time domain and finite volume time domain: IEEE Transactions on Antennas and Propogation, **42**, 1450–1455.

Yee, K. S., and J. S. Chen, 1997, The finite-difference time-domain (FDTD) and the finite-volume time-domain (FVTD) methods in solving Maxwell's equations: IEEE Transactions on Antennas and Propogation, **45**, 354–363.

Zhang, J., C.-Y. Wang, Y. Shi, Y. Cai, W.-C. Chi, D. Dreger, W. B. Cheng, and Y. H. Yuan, 2004, Three-dimensional crustal structure of central Taiwan from gravity inversion with a parallel genetic algorithm: Geophysics, **69**, 917–924.

Zhdanov, M. S., I. M. Varentsov, J. T. Weaver, N. G. Golubev, and V. A. Krylov, 1997, Methods for modelling electromagnetic fields: results from COMMEMI - the international project on the comparison of modelling methods for electromagnetic induction: Journal of Applied Geophysics, **37**, 133–271.

Zienkiewicz, O. C., and R. L. Taylor, 2000, The Finite Element Method, Volume 1: The Basis, 5th. ed.: Butterworth-Heinemann.